Doctoral Dissertation
Doctoral Program in Physics (35^{th}cycle)

Experimental and 2D/3D modeling investigation of DC magnetic shielding by machinable MgB_2 bulks

By

Michela Fracasso

******

Supervisor(s):
Prof. Laura Gozzelino

Doctoral Examination Committee:
Dr. Alessandra Manzin, Referee, Istituto Nazionale di Ricerca Metrologica
Prof. Massimiliano Polichetti, Referee, Università di Salerno
Dr. Marco Bonura, University of Geneva
Prof. Dario Daghero, Politecnico di Torino
Prof. Mauro Tortello, Politecnico di Torino

Politecnico di Torino
2023

Declaration

I hereby declare that, the contents and organization of this dissertation constitute my own original work and does not compromise in any way the rights of third parties, including those relating to the security of personal data.

Michela Fracasso
2023

* This dissertation is presented in partial fulfillment of the requirements for **Ph.D. degree** in the Graduate School of Politecnico di Torino (ScuDo).

Acknowledgements

First, I would like to express my profound gratitude to my supervisor, Professor Laura Gozzelino, for her assistance during my research work and her advice about both my academic career and future. My appreciation goes out to the whole SM-MESH research team, including Professors Gianluca Ghigo, Francesco Laviano, Roberto Gerbaldo and Daniele Torsello as well as my colleague Simone Sparacio. Finally, I would thank myself too, this time I deserve it.

Abstract

The main purpose of this thesis is to investigate and to exploit the superconducting properties of magnesium diboride (MgB_2) bulk samples with the aim to develop magnetic shields meeting the practical requirements of both high shielding factors and space-saving solutions. The project involves both an experimental and computational point of view. Experiment outputs give a first hint on the shielding ability of specific compositions/shapes as well as the parameters needed to model the material (e.g. the magnetic field dependence of the critical current density, $J_c(B)$). The numerical analysis aims to guide the design of more efficient magnetic shields and to predict their performance as a function of the magnetic field and temperature.

In more detail, the shielding properties of an open and a single-capped MgB_2 tube (the former henceforth denominated just tube and latter cup) with an aspect ratio of height to diameter close to one were experimentally characterized by means of cryogenic Hall probes. The samples were obtained by Spark Plasma Sintering (SPS) [1] of commercial MgB_2 powder of different purity mixed with hexagonal boron nitride (BN). Moreover, the characterization of a hybrid tube-shaped shield, obtained by superimposing a soft Fe shell on the MgB_2 tube, was performed as well. The magnetic flux density was measured at fixed positions along the axis of the shields in both axial (AF) and transverse (TF) field orientations. These measurements allowed the evaluation of the shielding efficiency providing the shielding factor, i.e. the ratio of the applied magnetic field to the measured magnetic flux density. From the same measurements, the dependence of the superconductor critical current on temperature and magnetic flux density was calculated as well (needed also for modeling the material). These measurements highlight two weaknesses of these shields: a huge decrease of their shielding ability when the applied field is tilted away from the screen axis and the occurrence of thermo-magnetic instabilities (namely, flux jumps) that cause abrupt magnetic field penetration inside the samples.

To investigate how overcoming these bottlenecks without useless experimental trials, a computational approach was adopted. To model the electromagnetic behaviour of the superconductor, a computational approach able to predict the shielding behaviour of the bulks placed either in the axial or transverse applied field orientation was chosen. While the former orientation can be modelled by a 2D axisymmetric simulation, the latter needs a 3D approach. For this purpose, a 3D simulation study was implemented by means of the commercial finite-element software COMSOL Multiphysics® [2]. Therefore, a numerical procedure based on the 3D vector-potential (**A**) formulation described in [3] was applied, assuming an electric field-current density (E-J) relation approximating the critical state in the superconductor.

To validate this modeling approach, two strategies were adopted. At first, I numerically analysed the shielding capability of superconducting tube- and cup-shaped shields, with dimensions replicating that of the samples experimentally characterized. Their shielding properties were calculated both in AF and TF orientations. In the case of the superconducting tube, the effect of the superimposition of a shorter ferromagnetic (FM) tube was also investigated. Simulation data were then compared with those previously measured experimentally on the same shielding arrangements, evidencing a good agreement. Then, I compared the results achieved on the tubular geometry with the above-mentioned A-formulation approach with those attained with the most used and already validated, 3D magnetic field (**H**) formulation (still implemented by means of COMSOL Multiphysics®). A good agreement was again obtained in AF, TF and intermediate field orientations, also evidencing how the adopted **A**-formulation is more advantageous in terms of time consumption.

Afterwards, I applied this as-validated model for investigating the shielding ability of new screening configurations. In particular, exploiting the peculiarity of FM tubular samples to provide high SFs in transverse field geometry [4, 5], I focused on hybrid arrangements, consisting of two coaxial cylindrical shields assumed made of MgB_2 (SC shield) and soft Fe (FM shield) having either equal or different heights. This analysis evidenced that the positive/negative effect of the addition of the FM shell strongly depends on the field orientation and on the relative height of the two components. In particular, the comparison between the shielding performances of these new hybrid configurations and the SC-only shields highlighted how the superimposition of a ferromagnetic shell is very efficient in mitigating the strong decrease of the superconductor shielding ability even for small tilt angle of the applied field.

The last numerical study focuses on the prediction of thermo-magnetic instabilities via a numerical multiphysics analysis, coupling the magnetic study based on the **A**-formulation with a thermal one. This approach allowed me to predict and study the flux jumps phenomena, already observed during the experimental measurements. In particular, taking advantage of the cylindrical symmetry of the investigated layouts and since the flux jumps were experimentally observed only in the AF orientation, a 2D axisymmetric model was implemented in the software package. The model was validated by comparing the computational outputs with the experimental results measured at different operational temperatures, namely 20 K, 25 K, and 30 K. The analysis shows an excellent agreement between the measured and calculated data, proving its reliability in reproducing the experimental shielding factor curves and their abrupt decrease caused by the flux jump events. The as-validated model was then used to investigate possible solutions to mitigate or even avoid the flux jump occurrence, such as enhancing the material thermal conductivity and the heat exchange with the cooling stage.

Contents

Chapter 1

Introduction

1.1 History of superconductivity

In 1908 Heike Kamerlingh-Onnes, who served as professor at the University of Leiden, reached the liquefaction of helium at the boiling point of 4.2 K [6]. This result allowed him to explore the physical properties of materials in a wide temperature range near the absolute zero point. Three years later, Kamerlingh-Onnes found out that the DC resistance of mercury (Hg) dropped to zero below 4.2 K. This result pointed out the first characteristic property of a superconductor, namely the zero electrical resistance below a threshold temperature T_c, called *critical temperature*. The superconducting behaviour was then discovered also for other elements, such as lead (Pb) in 1913 and Niobium (Nb) in 1940.

After Kamerlingh Onnes results, the behaviour of the superconductors was extensively studied. In 1933, Walther Meissner and Robert Ochsenfeld identified the second distinguish characteristic of a superconductor: the perfect diamagnetism, meaning that these materials have a magnetic susceptibility χ = -1. This property results in the capability of a superconductor, placed in an external applied field $\mathbf{H}_{app}$, to expel the magnetic flux lines keeping the magnetic field inside the material at zero. This characteristic is now called *Meissner effect* (see Section 1.1.2).

The discovery of the Meissner effect gave way to a theoretical study of the superconductivity. The first equations were proposed by the London brothers followed by the Ginzburg-Landau theory (1950), which described superconductivity in terms of an order parameter and provided a derivation for the London equations. Both the theories are macroscopic and only in 1957 Bardeen et al. [7] proposed a microscopic theory (BCS) explaining the fundamental mechanism by which electrons can pair up (pairing mechanism) through a phonon mediated interaction to form carriers that propagate without dissipation. However, for 75 years the superconductivity was accounted as a phenomenon limited to low temperature and only in 1986 Bednorz and Müller [8] discovered superconductors based on copper oxide (belonging to the cuprates class), initiating the era of the high-temperature superconductors. These materials present electronic correlations and spin fluctuations and the BCS theory cannot explain their high T_c. In 2001, superconductivity was reported in Magnesium Diboride (MgB_2) [9], whose peculiarity is that of being an intermetallic compound with a transition temperature of 39K. MgB_2 behaves like the "classical" metallic superconductors, however with two energy gaps. More recently, a new family of superconductors called iron-based superconductors (IBSs) was discovered [10], setting another turning point for the study of the superconductivity. Figure 1.1 shows a timeline of the superconductor discoveries.

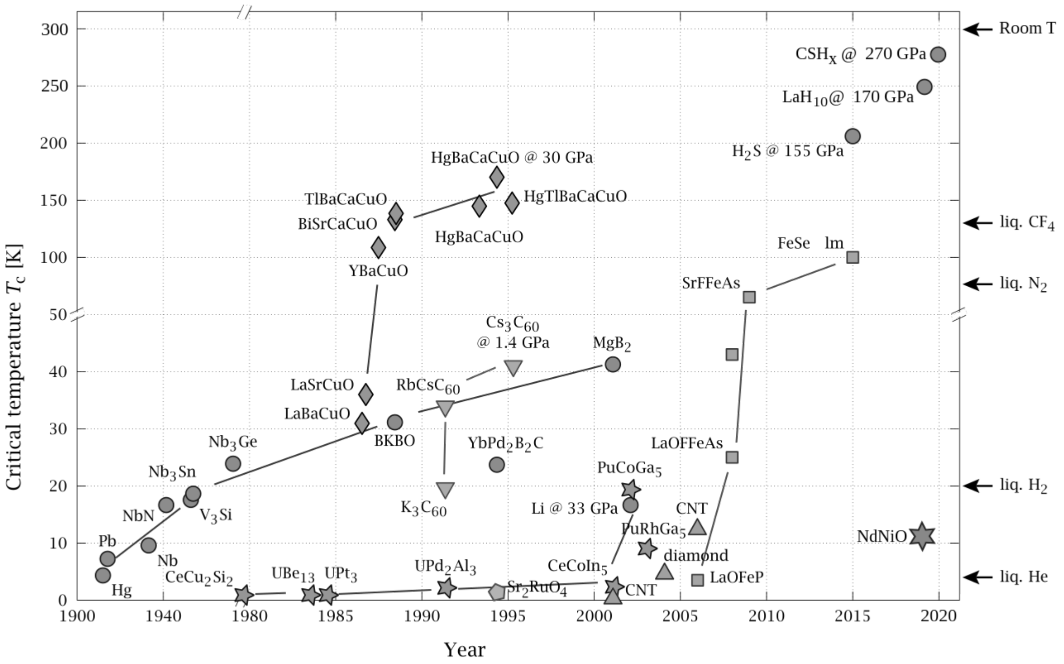

Fig. 1.1 Historical overview of the superconductor discoveries.

1.1.1 The critical surface

The first proof of superconductivity was the drop to zero of the electrical resistance below the critical temperature, T_c. This critical value represents the point at which the transition from the normal to the superconducting state occurs. Indeed, the existence of superconductivity is ensured if the material is below T_c. However, besides T_c, there are other critical parameters. One of them is the critical current density, J_c, namely the maximum current density that can flow in a superconductor before it reverts to the normal state. During his study on superconducting (SC) materials, Kamerlingh-Onnes also reported a critical value of the magnetic field, H_c, over which the materials go back to the normal state. Moreover, both J_c and H_c depend on temperature, T, increasing as T decreases.

Hence, the critical behaviour of a superconductor could be described in terms of a critical surface in a three-dimensional space formed by magnetic field H, electric transport current density J_{tr} and temperature T, as shown in Figure 1.2. The material is in the superconducting state if the values of temperature, field, and current are below this surface.

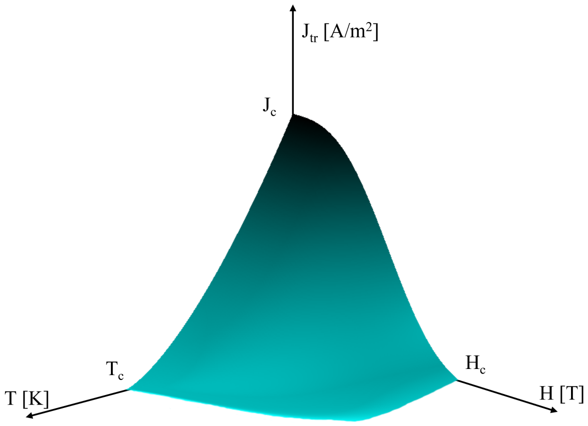

Fig. 1.2 Critical surface separating the normal (above the surface) and the superconducting states (below the surface).

1.1.2 The Meissner effect

As mentioned above, the second intrinsic characteristic of a superconductor is the perfect diamagnetism, resulting in the capacity of the material to expel the flux lines of the applied magnetic field, $\mathbf{H}_{app}$. From Maxwell equations, the relationship between the **B** and **H** fields within a material of permeability μ is

$$\mathbf{B} = \mu\mathbf{H} = \mu_0(\mathbf{H}+\mathbf{M}) \tag{1.1}$$

where **M** is the magnetization. Being the superconductor a perfect diamagnetic material, its magnetic susceptibility is χ=-1, then

$$\chi = \frac{\mathbf{M}}{\mathbf{H}} \quad \Rightarrow \quad \mathbf{M} = -\mathbf{H} \quad \mathit{and} \quad \mathbf{B} = 0 \tag{1.2}$$

This is equivalent to the assertion that the magnetic field **B** inside the material is zero because the magnetization **M** is directed opposite to the **H** field (Figure 1.3(a)-(b)).

Furthermore, the Meissner effect points out that a superconductor is not only a perfect conductor. To highlight this difference, suppose to magnetize a superconductor and a perfect conductor. Two ways of magnetization are possible, namely the Zero Field Cooling (ZFC) and the Field Cooling (FC) processes. The former consists in cooling the sample and then applying an external magnetic field, whereas the latter requires the cooling of the sample while an external magnetic field is applied. Figure 1.3 shows the different behaviour of a superconductor and a perfect conductor in case of a ZFC and FC process.

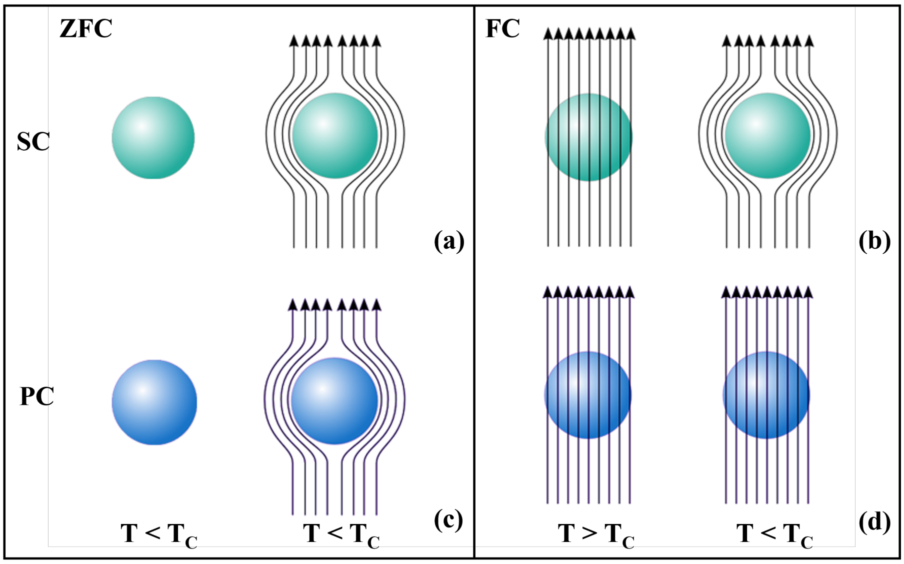

Fig. 1.3 Comparison between the response of a superconductor (a-b) and a perfect conductor (c-d) to a ZFC and FC magnetization process.

1.1.3 Superconducting materials classification

SC materials are generally classified in two ways: by temperature or by their magnetic response to an external applied magnetic field.

The former criterion leads to definitions of low-temperature superconducting (LTS) and high-temperature superconducting (HTS) materials. The LTS materials, typically called conventional superconductors, have a critical temperature below 30 K and their properties are fully explained by BCS and related theories. They usually refer to the Nb-based alloys and A15 type superconductors. Conversely, the HTS materials have a critical temperature above 30 K and their behaviour cannot be explained by conventional superconductivity theories. It is worth mentioning that it is difficult to insert MgB_2 in this classification, since its critical temperature is T_c=39 K, but its superconducting properties can be explained by conventional theories.

The second classification is based on the different response of the superconductor to an external applied magnetic field, leading to definitions of Type I and Type II superconductors. What defines the types of a superconductor is the number of states that the material can have. If an external field is applied, the Type I superconductor is in the Meissner state (perfect diamagnetism) below the critical field H_c. When the applied field exceeds this value, the SC state reverts back to the normal state.

In a Type II superconductor, an intermediate state, called mixed state, exists in the region of the H-T diagram limited by the lower, H_{c1}, and the upper, H_{c2}, critical magnetic field. Therefore, below H_{c1}, the superconductor is in the Meissner state, but above H_{c1} and below H_{c2} the magnetic field partially penetrates the sample in form of magnetic flux lines (fluxons) within which the material is in the normal state, whereas outside of them the material remains in the superconducting state. The flux lines are quantized and each quantum flux is surrounded by a screening current (called vortex) giving rise to a repulsive force that forces the flux lines cores to arrange themselves into a periodic array called the Abrikosov vortex lattice. As long as the applied field increases, the normal state gains more and more space and in correspondence to the upper critical field, H_{c2}, the material passes into the normal state (Figure 1.4). In terms of applications, this is the key to increase the work field range of a superconductor. Indeed, the use of Type I superconductors is limited by the extremely low T_c and H_c values. On the other hand, Type II superconductors, having a H_{c2} hundred times larger than H_c, can carry much larger amounts of current in higher magnetic fields.

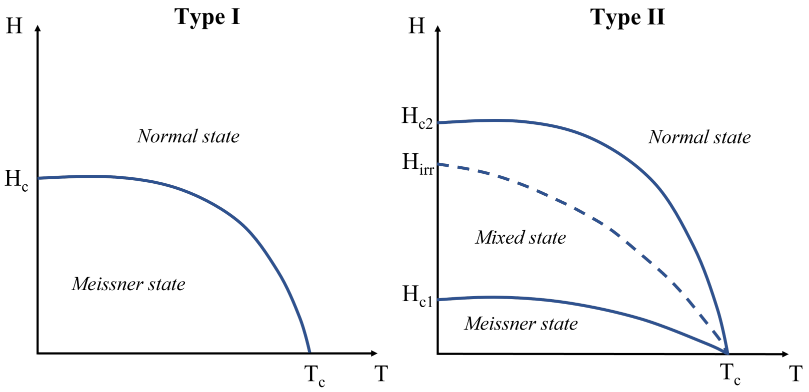

Fig. 1.4 Phase diagram of Type I and Type II superconductor in the J_{tr}=0 plane.

Actually, the region of a Type II superconductor phase diagram useful for applications is limited by another characteristic quantity, the irreversible field, H_{irr}, lower than the upper critical field H_{c2} [11]. In the field range H_{irr}<H<H_{c2}, due to the thermal fluctuation and instability of the vortex lattice, the current cannot flow without losses, i.e., the resistance is not zero, even if the material is in the superconducting state. For this reason, the knowledge of H_{irr} is a basic prerequisite for applications of high-temperature superconductors.

1.2 Superconductors applications

1.2.1 Wire, tapes and thin films superconductors

Because of their remarkable electric and magnetic properties, superconducting materials are nowadays an innovative solution for a wide range of applications, mostly as wires, tapes, and thin films [12, 13]. The large-scale applications of the superconductors cover different fields, such as energy, health, and transportation. In fact, the superconductor capability of carrying higher current density determines the possibility to produce magnetic fields much higher than the saturation field of ferromagnetic materials, such as iron [14]. In this framework, in the 1980s, superconductors started to be employed for Nuclear Magnetic Resonance (NMR) and Magnetic Resonance Imaging (MRI) magnets, which became the most successful commercial applications of superconductivity [15–17]. On the other hand, superconductors offer an opportunity for a change of pace in power system technology, improving the efficiency and lowering the carbon emissions. Superconductors are promising candidates for the fabrication of superconducting magnets in nuclear fusion reactors, which requires large values of the magnetic field [18, 19]. The use of superconductor for transformers and cables is also increasingly common, thanks to the possibility to reduce the energy losses and the smaller dimensions of the facilities. Under this perspective, the demand of more efficient solutions for energy supply and storage points the attention on superconducting devices such as Superconducting Rotating Machines (SRM) and Superconducting Magnetic Energy Storage (SMES) systems, respectively [20]. Superconducting materials are also an essential component of particle accelerators for high-energy physics, used, for instance, in experiments to study the most fundamental constituents of matter and how they interact, such as ATLAS, CMS and ALICE [21–23].

Additionally, superconducting thin films are widely exploited for small scale applications. The most common use is in Josephson Junctions-based devices, such as SQUIDs (Superconducting Quantum Interference Devices) or devices for terahertz spectroscopy [24]. SC thin films are also employed for the fabrication of bolometers, used to study extremely weak radiations in many environmental and astrophysical experiments [25]. Moreover, microwave devices (especially high-performance filters) using HTS films are very promising candidates for mobile communication systems, radio astronomy, and meteorology [26].

1.2.2 Bulk superconductors

In the last few years, also superconducting bulk materials have found a more widespread use thanks to the improvement of both their growth techniques and the cooling technologies required to exploit their potential. Nowadays, their applications have a wide scope, which – as suggested by Durrell et al. [27] - can fall into three areas: i) flux pinning applications, ii) flux trapping applications and iii) flux shielding applications. In each application field, the SC bulks are performing candidates to replace traditional solutions, e.g. acting as conventional permanent magnets [28–32] or competing with the ferromagnetic materials for low frequencies ($f < 1$ kHz) magnetic shielding [33].

Regarding the first applications, exploiting the flux pinning forces generated in the Type II superconductors greatly enhanced the stability of the levitation processes of a permanent magnet (PM) above a SC bulk. One of the magnetic levitation challenges is its application to magnetic levitated (MAGLEV) transportation, which provides a minimal friction of the vehicles under which superconducting bulks are placed with the PM guideway[34–36]. The PM-HTS arrangement was also proposed for the fabrication of magnetic bearings and flywheel energy storage systems [37, 38].

Between the flux trapping applications, it is worth mentioning the magnetic separation, useful for the purification of water or other fluids of interest [39, 40], or rotating machines [41, 42]. Following the same idea of flux trapping, portable NMR and MRI, that provide reasonably uniform high magnetic fields, were developed as well [43, 44].

The third application (flux shielding) will be treated in detail in the next section.

1.3 Magnetic shielding

Magnetic shielding is nowadays one of the most challenging perspectives for bulk superconductors, with a high growth potential. The necessity of using shielding solutions is twofold. The first aim is to protect ultra-sensitive devices, such as SQUIDs, even from ultra-low magnetic field background. On the other hand, the today's extensive use of superconducting magnets and other machines generating magnetic feelds of some tesla requires solutions for the protection of the surrounding space. Typically, these sources work at a value of magnetic field above the saturation field of the traditional solutions, generally employing ferromagnetic (FM) materials.

Although FM shields have been widely used [45–47], to overcome the saturation field of the ferromagnet is not the only challenge. The shielding capability of a FM shield depends on the dimensions of the bulk and on the magnetic permeability (μ_r) of the material [48]. To obtain high shielding performances with reasonable shield thicknesses (lower than 1 cm), FM materials with a very high relative magnetic permeability, $\mu_r \geq 10^4$, have to be used. In some commercial ferromagnetic shields, μ_r values up to 450 000 can be achieved in the DC case [49, 50]. However, thermal treatments are necessary to obtain so high values of μ_r, making the production of FM shields costly. Moreover, the ferromagnet relative permeability decreases when the frequency of the applied field, f, increases. For these reasons, the use of innovative options is fundamental for suitable and efficient shielding solutions.

Under this perspective, in the last years, superconducting shields have attracted a lot of interest. Indeed, they provided good results in several fields ranging from biomedical engineering to high-sensitivity instrumentation [51–54]. In the last few years, also the so-called hybrid solutions have gained many attentions [55, 56], mixing the shielding capability of both ferromagnetic and superconducting materials to enhance the total shielding performances. Moreover, with the same end in view, bulk superconductors can be combined with other SC layouts, such as coated conductors [57] or SC tapes [51], and recently tested solutions including both active [58] and passive layouts [27, 59, 60] have also been investigated. In 2010, it was first demonstrated magnetic shielding above 1 T using $Bi_2Sr_2CaCu_2O_8$ (Bi-2212) tubes at 10 K [61] or MgB_2 bulk at 4.2 K [62]. More recently, magnetic shielding up to 1 T at 20 K and up to 1.8 T at 20 K was achieved with cup-shaped Y-Ba-Cu-O bulk [63] and cup-shaped MgB_2 bulk [64] respectively, having an aspect ratio of height to diameter close to unity.

Although a lot of efforts have been made to improve the shielding performances of the SC bulks, some demanding challenges still need to be addressed. In more detail, the main aspects to be investigated are i) the shape and size of SC bulks and ii) the physical limitations and properties of the SC shields [27]. Regarding the first point, since the shield efficiency is related to the size of the induced macroscopic current loops, geometric parameters providing as large as possible current loops are preferred. Hence, to develop manufacturing process able to produce suitable, fashioned and high homogeneous shields is needed. At the same time, the knowledge of the physical behaviour of the samples can support innovative and efficient shielding solutions. For instance, superconductors can be subjected to flux jumps or other thermo-magnetic instabilities that can lead to a worsening of the shielding ability or even destroy the superconductors shield. In the same way, forces and torques exerted on the shield need also to be considered carefully, especially when the superconductor is subjected to a non-uniform field. Hence, a comprehensive understanding of the in field behaviour of a superconductor is a powerful tool. Under this perspective, developing characterisation and modeling techniques provides a good strategy to fabricate superconducting shells with improved shielding ability.

1.4 Numerical approaches for the study of the superconductors

The extensive use of superconducting bulks for different applications requires optimization processes in order to maximize the performances of the superconducting materials and to achieve a deeper understanding of the flux-lines dynamics. In this framework, a wide range of models and numerical approaches have been proposed since superconductivity has been discovered. To override the mathematical difficulties of fundamental theories, the electromagnetic behaviour of the superconductor in the mixed state is often described using phenomenological models based on constitutive equations relating the local electric field **E** and the local current density **J**. The most common approaches are the critical state model (CSM), which assumes the balance between the Lorentz and pinning forces acting on fluxons, and the power-law model that considers flux creep phenomena [65]. Both analytical [66] and numerical [67] methods have been proposed to predict the electromagnetic behaviour of a superconducting device. Among the latter, the finite element method (FEM), has turned out to be particularly suitable for complex geometries or when different elements are present (e.g. hybrid solutions with superconductor and ferromagnetic materials). Applying this method, current and magnetic field distribution can be calculated by solving the Maxwell equations

Different solution approaches, exploiting different equation packages, have been developed, such as the **A**–V formulation, based on the magnetic vector-electrostatic potentials [68], the T–Ω formulation, based on the current vector-magnetostatic potentials [69] and the **H**-formulation, based on the magnetic field [70]. Nonetheless, different and mixed formulations such as **A**-ϕ, **H**-ϕ, **H**-**A**, **T**-**A** and **T**-ϕ have been implemented successfully in electromagnetic dedicated FEM software packages, often in relation to a specific application [71–76].

1.5 Aim of the thesis

On the basis of the aforementioned considerations, the main purpose of this thesis is to investigate and to exploit the superconducting properties of magnesium diboride (MgB_2) bulk samples aimed at the development of magnetic shields. The project develops from both an experimental and a computational point of view. The shielding properties of an open and a single-capped MgB_2 tube (henceforth denominated tube and cup, respectively) were indeed experimentally characterized by means of cryogenic Hall probes, for both axial (AF) and transverse (TF) orientations of the applied field respect with to the shield axis. Relying on the experimental results, two critical issues emerged: i) the dependence of the shielding capability on the orientation of the applied magnetic field and ii) the presence of thermo-magnetic instabilities that completely deteriorate the shielding performances of the samples. With the aim to avoid unnecessary and time-consuming experimental procedures, possible solutions to the issues mentioned above were explored using a computational approach based on an $\mathbf{A}$ formulation. Firstly, the role of a FM layer superimposition on the superconducting shields was analyzed, aiming at the improvement of the screening abilities of the SC shields, especially in the TF orientation where a FM shield is predicted to be more powerful than the superconductor one. To this end, the shielding properties of both the superconducting and the new hybrid (superconducting+ferromagnetic, hereinafter SC+FM) layouts were investigated for different tilt angles (from 0° to 90°) of the applied magnetic field with respect to the shield axis. Then, I used a multyphisics approach to study the evolution of the thermo-magnetic instabilities inside the SC bulks and to explore possible solutions to mitigate or avoid this phenomenon occurrence.

The thesis is organized as follows. Chapter 2 focuses on the main characteristics of Type II superconductors and on the numerical models and formulations most widely used to reproduce the electromagnetic and thermal behaviour of a superconductor. In Chapter 3 *Materials and experimental procedures*, I present the properties of the employed materials and the experimental procedures followed for the shields characterization. In particular, in the first section of this chapter, the peculiar characteristics of MgB_2 are given, while the other sections illustrate the fabrication route of the investigated samples, the experimental setup and the measurements procedures. The experimental results obtained on both the tube- and cup-shaped shields are discussed in Chapter 4. Chapter 5 addresses the 3D numerical model based on the **A**-electromagnetic formulation, which was used to predict the screening ability of both the SC and hybrid shields for different tilt angles of the applied field. After presenting the procedure followed for the model validation, I focus on the numerical results obtained with the novel and more efficient shielding layouts. The multiphysics approach for the study of the thermo-magnetic instabilities and its validation procedure are discussed in Chapter 6, where possible improvements to mitigate/overcome this problem are also investigated. I summarize the main results in Chapter 7.

Chapter 2

Type II superconductors

In Section 1.1.3 the difference between Type I and Type II superconductors was introduced. Type II superconductors differ from Type I for the presence of a mixed state between the two critical fields H_{c1} and H_{c2}.
To deeper understand this difference under the perspective of this work, consider a long SC cylinder to which a magnetic field $\mathbf{H}_{app}$ is applied, parallel to its axis. This parallelism allows us to assume the boundary condition so that the H fields outside the sample (H_{app}) and inside the superconductor (B) are equal ($H_{app} = B/\mu_0$) at the surface of the sample, considering that the general expression 2.1 is valid both outside and inside a superconducting sample:

$$\mathbf{B} = \mu_0(\mathbf{H}+\mathbf{M}) \tag{2.1}$$

Taking into account a Type I superconductor, below H$_c$ (Meissner state), the field inside the superconductor is zero. That means, from Equation 2.1

$$\left.\begin{aligned} \mu_0 M &= -\mu_0 H_{app} \\ B &= 0 \end{aligned}\right\} \qquad 0 \leq H_{app} \leq H_c \tag{2.2}$$

Above the critical field H$_c$ the superconductor becomes normal, the magnetization M becomes negligibly small and $\mu_0 H_{app} \approx B$.

The behaviour is different in the case of a Type II superconductor, which has two critical fields. As in case of Type I superconductor, in the Meissner state, below H$_{c1}$, the internal field and magnetization are given by:

$$\left.\begin{aligned}\mu_0 M &= -\mu_0 H_{app}\\ B &= 0\end{aligned}\right\} \qquad 0 \leq H_{app} \leq H_{c1} \tag{2.3}$$

While, when the field exceeds the critical value H_{c1}, the internal field and magnetization are given by:

$$\left.\begin{aligned}\mu_0 M &= -(\mu_0 H_{app} - B)\\ M &= \chi(H) \cdot H_{app}\end{aligned}\right\} \qquad H_{c1} \leq H_{app} \leq H_{c2} \tag{2.4}$$

being B the magnitude of the inner magnetic flux density. The comparison of the different behaviours of Type I and Type II superconductors is shown in Figure 2.1, still referring to an ideal SC cylinder.

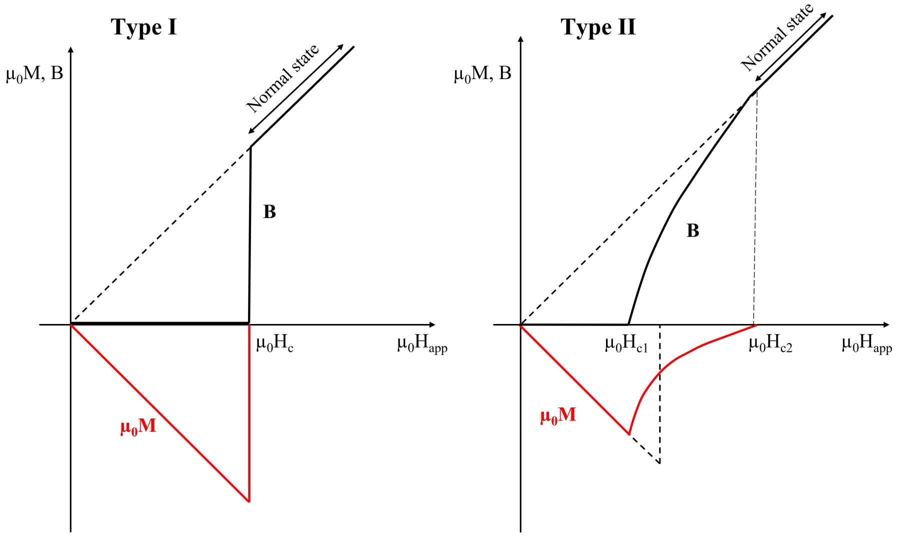

Fig. 2.1 Evolution of the magnetic flux density (black curves) and magnetization (red curves) calculated in the volume of the superconductor, as a function of the applied magnetic field for a Type I (left) and a Type II (right) superconductors.

In the next sections, the main characteristics of Type II superconductors are presented.

2.1 Characteristic lengths scale of superconductors

In 1950, a phenomenological approach for the study of superconductivity was proposed by Ginzburg and Landau (GL) [77]. The GL theory assumes that in the superconducting state the current is carried by super-electrons, whose density, ${n_s}^*$, is defined as

$$ {n_s}^* = \frac{1}{2} n_s \tag{2.5} $$

where n_s is its electron counterpart. The main assumption of the theory is the description of the superconductivity in terms of a complex order parameter ϕ, which is related to the fact that $|\phi|^2$ is proportional to the density ${n_s}^*$ of the super-electrons.

$$ {n_s}^* = |\phi|^2 \tag{2.6} $$

Hence, the parameter ϕ increases continuously as the temperature decreases below T_c and is zero above T_c.

In the GL theory, the behaviour of superconductivity is associated with two fundamental length-scales, namely the coherence length, ξ, and the penetration depth, λ. The coherence length ξ is related to the distribution of the density of super-electron ${n_s}^*$, which increases from zero at the boundary of the superconductor to a constant value far inside the material. The penetration length λ characterizes the exponential decay of an external applied field inside the superconductor.

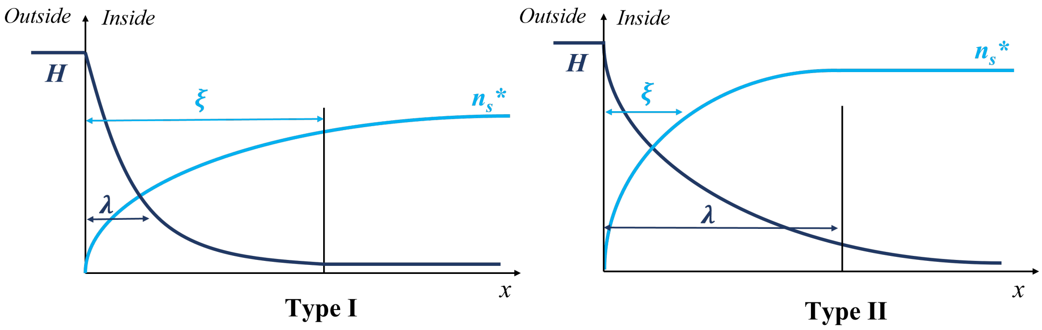

Fig. 2.2 Behaviour of the coherence length, ξ, and the penetration depth, λ, in correspondence to a boundary of a superconductor, delimiting the region outside and inside the superconductor, for Type I (left) and Type II (right) superconductors.

Figure 2.2 shows the typical behaviour of λ and ξ for Type I and II superconductors. Type I are characterized by a $\lambda \ll \xi$, while, for the Type II, $\lambda \gg \xi$. This means that, for Type II superconductors, near the external surface of the superconductor a high concentration of super-electrons coexists with a relatively large magnetic field strengths.

When the applied field exceeds H_{c1}, Type II superconductor enters the mixed state. Magnetic flux lines start entering the materials in the form of tubular regions of quantized confined magnetic flux (the fluxons). In their core, having a radius equal to ξ, the magnetic field reaches its highest value. The core is surrounded by screening current flowing around it (the vortices) on a radius given by the penetration depth, λ. Therefore, the magnetic field around the core decays exponentially with a dependence on λ (Figure 2.3). When the applied magnetic field increases, the density of the fluxons/vortices increases and they begin to overlap, while preserving the quantization condition. The meaning assumed by the coherence length and the penetration depth makes clear the reason why the mixed state is not present in a Type I superconductor. The fluxons only exist in Type II superconductor where λ is greater than ξ: this concept becomes pointless in case of Type I superconductors where $\lambda \ll \xi$.

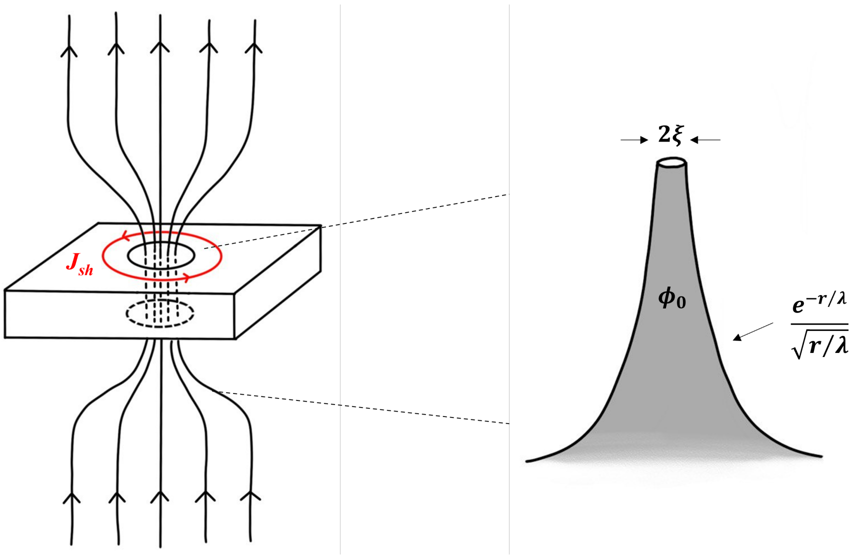

Fig. 2.3 Sketch of a magnetic fluxon surrounded by a vortex. The coherence radius of the core and the decay of B at large distance, dependent on the penetration depth λ, are indicated.

2.2 Pinning forces

When the mixed state takes place and the fluxons enter the superconductor, each fluxon is subject to a mutual-repulsion Lorentz force, which, per unit volume, is $\mathbf{J}_i \times \mathbf{B}_j$ due to the interaction between the current density $\mathbf{J}_i$ of one fluxon and the magnetic field $\mathbf{B}_j$ in the core of an adjacent fluxon. If the fluxons are not pinned or trapped, this mutual repulsion causes the arrangement of the fluxons in a hexagonal equilibrium configuration, called *Abrikosov lattice*. This situation corresponds to a zero magnetic field gradient in the sample and so, in accordance to the Ampere equation, to a zero critical current flow, meaning that J_c is effectively zero.

Let's consider a Type II superconductor carrying a uniform current density $\mathbf{J}$. The local magnetic flux density is $\mathbf{B} \perp \mathbf{J}$. Hence, on each fluxon a Lorentz force is exerted equal to $\mathbf{F}_L = \mathbf{J} \times \mathbf{B}$ per unit volume. This determines a displacement of the fluxon which moves in the direction of $\mathbf{F}_L$. This means that, if each fluxon (carrying its flux) moves across the sample with a constant velocity $\mathbf{v}$, it generates an electric field $\mathbf{E}$ (parallel to $\mathbf{J}$) due to Faraday law, which in turn gives rise to an Ohmic loss, so to a heat dissipation $Q = \mathbf{J} \cdot \mathbf{E}$.

For practical applications, pinning forces are needed in order to support the current density flow in the superconductor without resistance. The pinning force density, $\mathbf{F}_p$ balances the Lorentz force, keeping the fluxons in place: $\mathbf{F}_p = \mathbf{F}_L = \mathbf{J} \times \mathbf{B}$. Actually, if pinning centres are present in the material, a magnetic field gradient is established across the sample. Thus, in accordance to Ampere equation, $\mathbf{J}_c$ increases as the pinning strength does. In particular, the pinning forces have to be strong enough to prevent the flux motion and consequently the heat dissipation, but weak enough to allow the starting fluxon motion to establish a magnetic flux gradient. In practice, however, the fluxons are not able to freely move in a superconductor, since non-superconducting phases, inhomogeneities, and defects within the material, such as dislocations, voids, and grain boundaries act as pinning sites, determining a frictional force preventing the motion of flux lines. If a prevalent type of defects is present in the materials, a specific pinning regime can be established [78]. It is possible to obtain single fluxon or fluxon bundle pinning. In the first case, only a single line is pinned by the defect, whereas for the fluxon bundle situation, a bundle of lines can be pinned by the collective action of many weak defects (weak collective pinning) or the independent action of stronger defects [79]. A lot of efforts have been made by several research teams in order to add pinning centres in the materials, both by fabrication processes or by adding them with extrinsic techniques, such as irradiation [80–84].

In the case that the fluxons are free to move in the superconductor, the superconductor is said to be in a reversible regime; on the other hand, if the fluxons are pinned by the pinning centres, the superconductor is in an irreversible regime. In the next section, the characteristics of an irreversible superconductor are investigated.

2.3 Bean model

As said in the previous section, a superconductor in which the fluxons cannot freely move in the material is in an irreversible state. That means that when a parameter, such as temperature, current density or external applied field, changes its value, hysteretic effect occurs, and the system cannot reverse its former path. Moreover, due to the pinning forces present in the material, the fluxons distribution strongly varies from the equilibrium Abrikosov lattice. One of the first models developed in order to describe the magnetization behaviour of Type II superconductors is the critical state model (CSM). This model postulates that when an external field is applied to a superconductor, only two regions can be distinguished: i) an external region, which is in the critical state, with specific values of current density and not completely shielded and ii) an internal region completely shielded from the external field within which the current density related to fluxon penetration is zero. When the applied field is increased, the first region extends in the superconductor and for sufficiently strong fields fully penetrates the material. In this state, every macroscopic region in the sample carries a critical or maximum current density $J(B)$ determined by the local magnetic field at that region [85].

The critical state model was originally proposed by Charles Bean in 1964. His model, now known as the Bean critical state model, is able to describe the fluxon distribution, or in other words the irreversible magnetisation behaviour of Type II superconductors [86]. The model proposed by Bean is based on some fundamental assumptions:

- the critical current J_c is field independent

- the relative permeability of Type II superconductor, μ_r, in the mixed state is 1, as in free space, i.e., B = μ_0H;
- the Meissner state is considered as negligible
- the current induced by the applied field is zero where the field is not penetrated and $J = J_c$ in the region penetrated by the flux lines

Expressing the SC internal magnetic flux density **B**=μ_0**H** as the average flux density over regions containing several fluxons, the model allows calculating **B** as a function of the position inside the material and the external applied magnetic field **H**$_{app}$. Based on the above assumptions, the magnetic behaviour in the two regions of the superconductor can be summarized by the following equations derived from Ampere law:

$$\nabla \times \mathbf{B} = \mu_0 \mathbf{J}_c \qquad or \qquad \nabla \times \mathbf{B} = 0 \tag{2.7}$$

To better understand the field distribution proposed by Bean, we can consider the infinitely long tube in the uniform axial magnetic field of Figure 2.4. The thickness of the tube is $d = a_2 - a_1 \gg \lambda$.

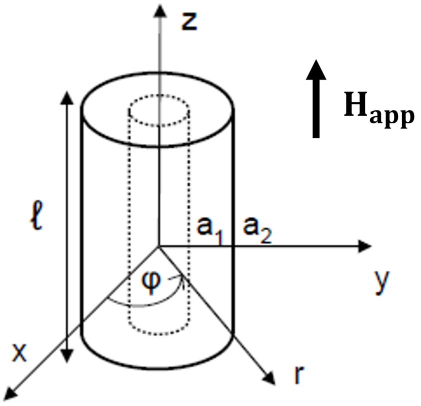

Fig. 2.4 Irreversible Type-II superconductor tube in a uniform axial applied magnetic field, **H**$_{app}$, with height $\ell \to \infty$.

Working with cylindrical coordinates and assuming **H**$_{app}$ parallel to z-axis, equations 2.7 can be written as

$$\frac{\partial B_z}{\partial r} = \mu_0 J_c \qquad or \qquad \frac{\partial B_z}{\partial r} = 0 \tag{2.8}$$

The latter equation establishes that, because of the spatial variation of **B**, a macroscopic current flows in the superconductor. As known from the previous section, this current determines a Lorentz force driving the fluxons to move. However, due to the pinning mechanism, their motion is stopped if the pinning force $\mathbf{F}_P$ equals the Lorentz force $\mathbf{F}_L$ ($\mathbf{F}_P$=$\mathbf{F}_L$).

Consider again the superconducting tube in Figure 2.4, previously cooled in ZFC condition, and subjected to an applied magnetic field $\mathbf{H}_{app} \parallel z$. Under these conditions, the fluxons start to penetrate in the material from the outer surface but are strongly pinned. For this reason, the distribution of B_z is non-uniform along the tube thickness, reaching its maximum at r = a_2. From Equation 2.8, this non uniformity of B_z distribution determines a flowing current density J_c. As B_z increases, $|\mathbf{F}_L|$ is temporarily higher than $|\mathbf{F}_P|$ and the fluxons start to move towards the centre of the tube. Thus, the current density is $\pm J_c$ in the penetrated zones and zero elsewhere. This continues until the full penetration of the sample is reached for H_{app}=H_p (Figure 2.5). If H_{app} is further increased above H_p, B(r) increases uniformly along the tube thickness, and the current distribution is no longer changed. Since the currents flow in such a way that in the inner zones of the sample the local magnetic flux density is reduced – as shown in Figure 2.5 - they are also called shielding currents.

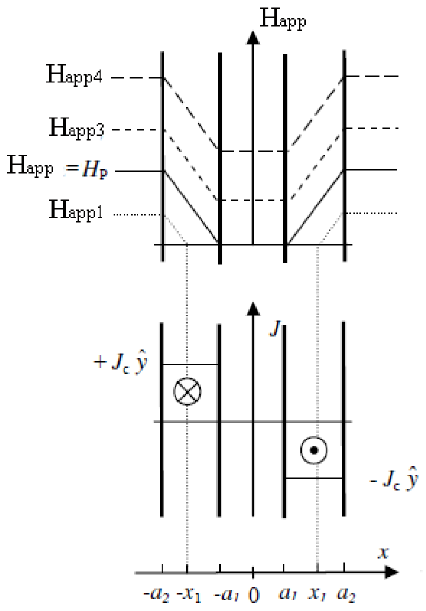

Fig. 2.5 Magnetic field and current density distributions according to the Bean model in the infinite tube of Figure 2.4 subjected to a uniform and increasing axial applied magnetic field, $\mathbf{H}_{app}$.

2.4 Limitation of the Bean model and the E-J power law

In the Bean model, the magnitude of the current density that flows in the superconductor can take only the constant and maximum value J=J$_c$ or zero. Since the variation of the local magnetic flux density **B** induces an electromotive force which, in turn, induces the current to flow locally, the relation between the electric field, E, and the current density, J, is that shown in Figure 2.6: if $J < J_c$ the electric field is zero, otherwise if $J > J_c$ then $E \to \infty$.

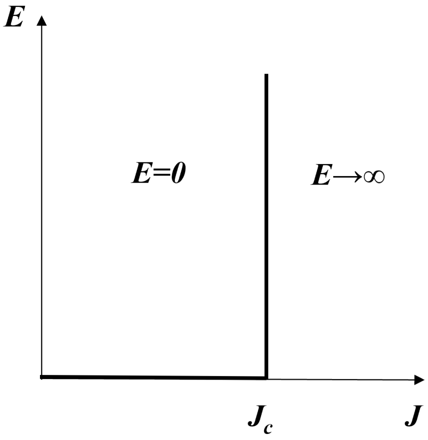

Fig. 2.6 E-J curve of an irreversible Type-II superconductor in according to the Bean model.

Another assumption of the Bean model is that only the Lorentz force, $\mathbf{F}_L$, can depin the fluxons. While the distribution of fluxons in the Abrikosov lattice is an equilibrium configuration, that of the pinned fluxons is a non-equilibrium state. For HTSs some processes, such as thermal activation, quantum tunnelling or other external activation (e.g. mechanical vibrations), could relax this non-equilibrium configuration of fluxons causing the flux lines to spontaneously move out of their pinning sites. However, once depinned, fluxons are affected by the Lorentz force and driven in its direction. The interconnection of these two depinning mechanisms establishes a different relation between the electric field and current density. As a consequence, the E-J curve shown in Figure 2.6 is no longer a correct representation of the E-J relationship.

To better explain the E-J behaviour, first consider the case of T=0 K. In this situation, the Lorentz force F_L dominates and only the F_L can unpin the fluxons. When this happens, the superconductor enters the so-called *flux-flow* regime. The fluxons moving in the superconductor experience a viscous drag. Hence, the E-J relationship can be expressed, as a first approximation as

$$\mathbf{E} = \rho_{ff}\mathbf{J} \tag{2.9}$$

where ρ_{ff} is the flux-flow resistivity. Otherwise, if $T \neq 0$, the thermal activation can depin the fluxons as well. For HTSs, pinning energies are quite small and the working temperatures are usually high, making the thermal activation an important issue for their practical applications [87–90]. For working temperatures near the critical one, T_c, a small value of the current density is needed to depin the fluxons.

In 1962, Anderson proposed the *flux creep theory*, which also considers the thermal activation as the cause of fluxons hopping [91]. Anderson introduced a hopping time t as a function of the potential-energy barrier height U, the Boltzmann constant k, the temperature T and the effective hopping attempt time t_0:

$$t = t_0 \exp\left(-\frac{U}{kT}\right) \tag{2.10}$$

Since the hopping of fluxons is assisted by the Lorentz force, the barrier U should be a decreasing function of J and, as a first approximation, one can write U as a linear function of J:

$$U(J) = U_0\left(1 - \frac{J}{J_c}\right) \tag{2.11}$$

where U_0 is the barrier height in the absence of a driving force. Combining equations 2.10 and 2.11, one obtains the expression predicting the temporal logarithmic decay of currents:

$$J = J_c\left[1 - \frac{kT}{U_0} ln \frac{t}{t_0}\right] \tag{2.12}$$

A later version of the flux creep theory was also proposed by Zeldov *et al.* [92] taking into account a nonlinear U(J) dependence:

$$U(J) = U_0 ln \frac{J_c}{J} \tag{2.13}$$

In order to establish a relation between the flux creep and the E-J curve, one has to take into account that the moving fluxons, experiencing a Lorentz force, induce an electric field $\mathbf{E} = \mathbf{B} \times \mathbf{v}$, where $\mathbf{v}$ is the average velocity of the flux lines in the direction of the Lorentz force. The average velocity v can be associated with the thermally activated flux lines, as:

$$v = v_0 \exp\left[-\frac{U(J)}{kT}\right] \tag{2.14}$$

where v_0 is the velocity with no barrier. If the fluxons is moving perpendicular to the field B, then E=Bv. Hence, using Equation 2.14, one obtains:

$$E = E_0 \left(\frac{J}{J_c} \right)^n \tag{2.15}$$

with $n = U_0/kT$ and $E_0 = Bv_0$.

n is called the creep factor and defines the steepness of the transition between the superconducting state and the normal state. If $n = 1$, Equation 2.15 describes a normal conducting material (linear Ohm law), whereas for $n \rightarrow \infty$ it reduces to the Bean model. Figure 2.7 shows a comparison among E-J curves obtained from Equation 2.15 for different n values.

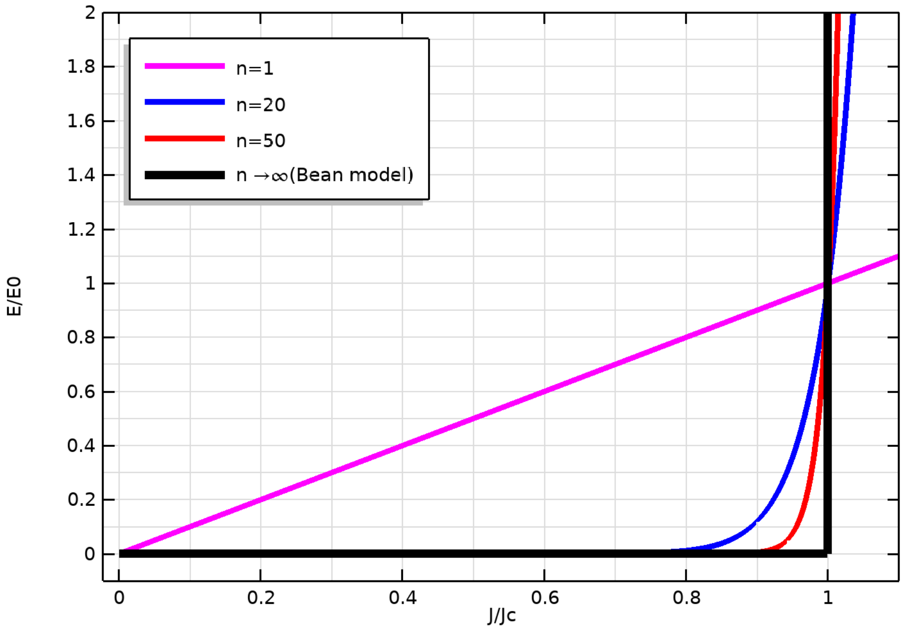

Fig. 2.7 Comparison of the E–J power laws (Equation 2.15) for n = 1 (linear Ohm law), 20 and 50, as well as for $n \rightarrow \infty$ (corresponding to the Bean model).

2.5 A-V formulation

The description of the electromagnetic behaviour of HTSs is challenging, especially in applications with variable magnetic fields, where one needs to be able to follow the motion of the magnetic flux front. In order to better understand the electromagnetic and thermal behaviour of superconducting devices, in the last few years several numerical models have gained a lot of popularity. These models provide a typical approach to researching the electromagnetic response of HTSs, i.e. using finite elements method to calculate a differential form of time-dependent Maxwell equations with a nonlinear resistivity (or conductivity) to characterize the superconductor electrical behaviour [93]. Among the several formulations developed to this aim, the **H**- and **A**-V formulations are the most common used. By using the **A**-V formulation, the Maxwell equations are written in terms of the vector magnetic potential **A** and the electric potential V. Expressing the electric conductivity $\sigma(E)$ as a function of E and remembering that $\mathbf{E} = -\partial\mathbf{A}/\partial t - \nabla V$, the constitutive equation is

$$\mu\sigma(E)\frac{\partial \mathbf{A}}{\partial t} - \nabla\times\nabla\times\mathbf{A} = -\mu\sigma(E)\nabla V \tag{2.16}$$

In order to solve this equation and properly characterize the behaviour of the superconductor, a relation between the electric field and the current density have to be used. The conventional power law relation between E and J is commonly used. Even if this relation can be implemented easily in commercial finite element programs, for hard superconductors n usually takes a huge value that can lead to numerical difficulties. Moreover, the true critical state, where n becomes infinite, is not accessible. So smoother and more stable E-J relations are needed. In the next section, the E-J relations proposed by Campbell and Gomory will be discussed.

2.5.1 Campbell model and hyperbolic-tangent approach

In 2007 Campbell [94] proposed a model based on the force-displacement of the flux lines [95, 96]. According to the Campbell model, when the flux lines experience a force, they move elastically for a short distance and then, when the flux lines start to be unpinned, the force turns out to be a frictional force. Hence, the magnitude of the force per unit volume f can be expressed as:

$$f = BJ_c\left[1-\exp\left(-\frac{|s|}{d}\right)\right] \tag{2.17}$$

where s is the fluxon displacement and d is a characteristic distance connected to the fluxons distance. The displacement can be related to the vector potential taking into account the following relation:

$$-\frac{\partial \mathbf{A}}{\partial t} = \mathbf{E} = \mathbf{B} \times \mathbf{v} = \mathbf{B} \times \frac{\partial \mathbf{s}}{\partial t} \tag{2.18}$$

Since ***s*** is perpendicular to ***B***, then the following scalar equation can been written:

$$s = -\frac{A}{B} \tag{2.19}$$

For the fluxons in a stationary condition, the Lorentz force must balance the pinning force. Being **B** perpendicular to **J** and since both the Lorentz and pinning forces lie on the same plane, the force magnitudes are related by:

$$BJ = -BJ_c\left[1 - \exp\left(-\frac{|s|}{d}\right)\right] \tag{2.20}$$

where the left-hand side is the Lorentz force (per unit volume) and the right-hand side is the force exerted by the pinning centres as a function of the fluxon displacement [94]. Combining equations 2.19 and 2.20, the equation for positive displacements can be obtained as:

$$J = -J_c\left[1 - \exp\left(-\left|\frac{A}{Bd}\right|\right)\right] \tag{2.21}$$

Next, in order to take into account both positive and negative displacements, Campbell introduced the following equation:

$$J = -sgn(A)J_c\left[1 - \exp\left(-\left|\frac{A}{Bd}\right|\right)\right] \tag{2.22}$$

and, finally, considering the Maxwell equation $\nabla \times \nabla \times \mathbf{A} = \mu_0 \mathbf{J}$, the following equation – only involving the vector potential – is achieved:

$$\nabla \times \nabla \times \mathbf{A} = -sgn(A)\mu_0 J_c\left[1 - \exp\left(-\left|\frac{A}{Bd}\right|\right)\right]\hat{\mathbf{u}} \tag{2.23}$$

The sign of A determines the sign of J with the exponential, giving a continuous transition through zero. Then, this equation can be considered a reformulation of the equation $J = +J_c, 0$ or -J_c predicted in the critical state. The key point of this approach is that the current density behaviour is expressed only in terms of the vector potential **A**.

Relying on the numerical method presented by Campbell [94], Gömöry et al. [97, 98] proposed an alternative 2D form of the critical state formulation, still using the vector potential $\mathbf{A}$ to model the behaviour of the SC materials. This approach lies on two hypotheses: i) the external magnetic field increases monotonically and ii) there is a *neutral zone* where the electric field vanishes. From Maxwell equations, the electric field can be expressed as

$$\mathbf{E} = -\frac{\partial \mathbf{A}}{\partial t} - \nabla V \tag{2.24}$$

In the case of a superconductor infinitely extended along the z axis, for symmetry reasons, the electric field components in the xy plane vanish and its magnitude is z independent. As a consequence, the current flows exclusively in the direction perpendicular to the xy plane [3], ∇V has only z component and V takes the same values in all the cross sections of the superconductor, thus it only depends on time. Applying Equation 2.24 to the neutral zone, one obtains:

$$\nabla V = -\frac{\partial \mathbf{A}_c}{\partial t} \tag{2.25}$$

where $\mathbf{A}_c$ is the vector potential at the neutral zone. The existence of the neutral zone allows defining a normalized vector potential

$$\mathbf{A}' = \mathbf{A} - \mathbf{A}_c \tag{2.26}$$

so taking into account that $\mathbf{A}'_c$ is zero, the equation to be solved becomes:

$$\mathbf{E} = -\frac{\partial \mathbf{A}'}{\partial t} \tag{2.27}$$

For a single shape with axial symmetry, there is always a neutral zone, validating the use of the Equation 2.27. Moreover, for a 2D axisymmetric problem with H_{app}=H_z Equation 2.27 can be simplified as:

$$E_\phi = -\frac{\partial A_\phi}{\partial t} \tag{2.28}$$

In order to solve Equation 2.28, a non-linear *E*-*J* relation has to be introduced to describe the superconducting behaviour. The following power-law dependence is one of the most used relations:

$$E_\phi = E_0 \left(\frac{J_\phi}{J_c} \right)^n \tag{2.29}$$

Combining Equation 2.28 and 2.29 one obtain:

$$J_\phi = J_c \sqrt[n]{-\frac{\partial A'_\phi}{\partial t E_0}} \tag{2.30}$$

where E_0 is usually set to 10^{-4} V m^{-1}. From a computational point of view, this equation presents two limits: i) it is defined only for odd n in case of negative argument and ii) it is not smooth at zero. Since for hard superconductors, n usually takes large value, i.e. $n \gg 1$, Equation 2.30 converges to the signum function as proposed by Campbell:

$$J_\phi = J_c sign\left(-\frac{\partial A_\phi}{\partial t E_0} \right) \tag{2.31}$$

which fully verifies the critical state model definition:

$$J = \begin{cases} +J_c & for \quad \partial A_\phi / \partial t < 0 \\ 0 & for \quad \partial A_\phi / \partial t = 0 \\ -J_c & for \quad \partial A_\phi / \partial t > 0 \end{cases} \tag{2.32}$$

However, this formulation still makes its use in computational problem not trivial, having the derivative divergent at zero. For this reason, Gomory *et al.* [97, 98] proposed the use of the hyperbolic tangent function instead of the signum function, modifying the shape of J as:

$$J_\phi = J_c \tanh\left(-\frac{1}{E_0} \frac{\partial A_\phi}{\partial t} \right) \tag{2.33}$$

Figure 2.8 shows a comparison between the E-J curves discussed above.

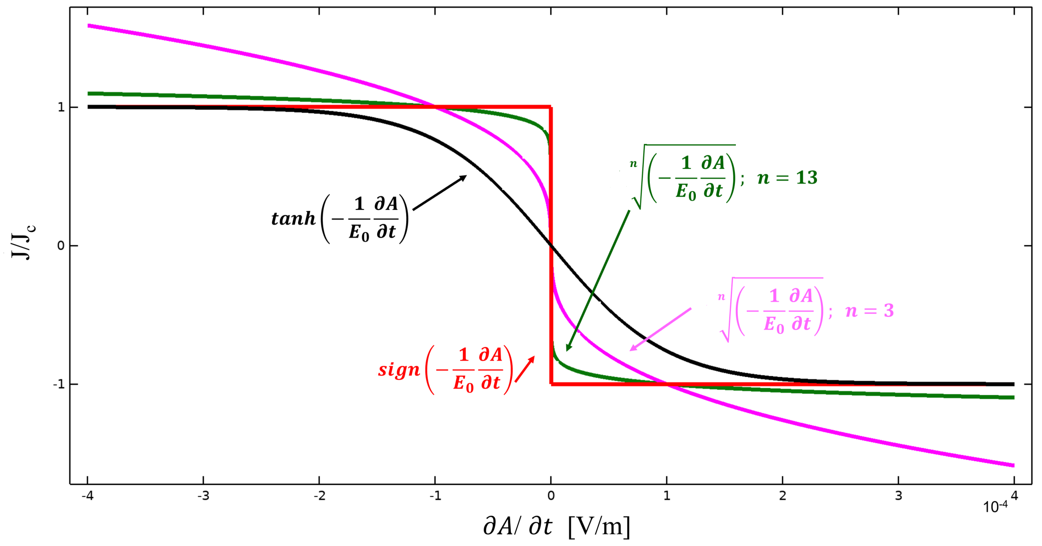

Fig. 2.8 A graphic comparison of the different functions that could be used to relate the current density and the vector potential time derivative.

Very recently, Solovyov et al. [3] extended this formulation to solve a 3D problem, assuming that Equation 2.33 is valid for each component of the vectors **A** and **J** separately (see Section 5.1). In addition, this approach was also successfully used to model SC samples in SC+FM hybrid structures [99].

2.6 H-formulation

From a mathematical point of view, the **H**-formulation uses the finite-element method to solve Faraday equation, which in terms of the magnetic field **H** takes the form:

$$\frac{\partial \mu_0 \mu_r \mathbf{H}}{\partial t} + \nabla \times (\rho(J) \nabla \times \mathbf{H}) = 0 \tag{2.34}$$

where μ_r is the relative magnetic permeability and $\rho(J)$ the resistivity [100]. The superconductor is usually modeled as a material with a non-linear electrical resistivity, showing the power–law dependence on the current density (see Section 2.4):

$$\rho(J) = \frac{E_0}{J_c}\left[\frac{|\mathbf{J}|}{J_c}\right]^{n-1} \tag{2.35}$$

where E_0 is the same conventional electric field as in Equation 2.15, whose value is generally assumed $E_0 = 10^{-4}$ Vm^{-1}, $\mathbf{J}$ is the current density, J_c is the critical current density and the n value is a factor indicating the steepness of the transition from the superconducting to the normal state (see Figure 2.7). In the last few years, the **H**-formulation has been the most commonly used approach. Actually, its implementation is quite simple, since no gauging or post-processing is required [72]. However, using the **H**-formulation implies some challenges, such as a higher number of degrees of freedom that increases the computational time [101]. Furthermore, a degradation of the matrix conditioning is caused by the requirement of an artificial resistivity in non-conducting domains [72].

2.7 J-B relations

Several numerical approaches have been developed with the aim to properly describe the superconductors and investigate new arrangements and applications [102]. Independently of the mathematical formulation, software implementation or adopted numerical method, a key aspect is to find a suitable relation between the electric field E and the current density J. The most E-J relation used is the power law, where $E \propto J^n$ (see Section 2.4). However, different constitutive laws are used in a wide papers and works [65], as models based on the CSM [86, 66, 103, 104], the percolation model [105] or the eta-beta model [106]. In 1963, Kim and Anderson [85, 91] proposed an empirical equation that takes into account the strong dependence of the critical current on the local magnetic field:

$$J_c(B) = \frac{J_{c0}}{\left(1 + \frac{B}{B_0}\right)^{\alpha}} \tag{2.36}$$

where B_0 and α are material-dependent constants that can vary with temperature and J_{c0} is the magnitude of the critical current density when the local field is zero.
A different behaviour of J_c was observed in some HTSs and MgB_2 [107–109], which are typically represented by the following exponential law:

$$J_c(B) = J_{c0} exp\left[-\left(\frac{B}{B_0}\right)^{\beta}\right] \tag{2.37}$$

where B$_0$ and β are material-dependent constants. In particular, the β parameter can define different pinning regime according to the collective pinning theory as reported in [110]. Table 2.1 summarizes the most common current-field relationship.

$J_c(B) = J_c$	Bean [111, 86]
$J_c(B) = \frac{J_{c0}}{\lvert B\rvert/B_0}$	Fixed Pinning [112]
$J_c(B) = \frac{J_{c0}}{\lvert B/B_0\rvert^{1/2}}$	Square Root [112]
$J_c(B) = \frac{J_{c0}}{1+\lvert B\rvert/B_0}$	Kim [85]
$J_c(B) = J_{c0}\exp[-\lvert B\rvert/B_0]$	Exponential [113]
$J_c(B) = J_{c0} - J'_{c0}\lvert B\rvert/B_0$	Linear [114]
$J_c(B) = \frac{J_{c0}}{[1+\lvert B\rvert/B_0]^{\alpha}}$	Kim generalized [85, 91]
$J_c(B) = J_{c0}\exp[(-\frac{B}{B_0})^{\beta}])$	Exponential generalized [110]

Table 2.1 Current-field relationships.

However, since the critical current density J_c is a crucial parameter for the characterization of the superconductors, its dependence on temperature and, in the anisotropic superconductors, on the angle between the applied field direction and the axis of the crystal lattice must be accounted for, i.e. J$_c(B,T,\theta)$.

2.8 Thermo-magnetic instabilities

Sections 2.4 investigated the hopping mechanism of fluxons that can arise when the superconductor is in the critical state [115, 116]. When the superconductor is in this non-equilibrium state, some uncontrolled instabilities can arise, such as quench phenomena or other thermo-magnetic instabilities [117]. Among the latter, the flux jump phenomenon can totally compromise the superconducting properties of the samples. When a flux-jumping process starts, it causes a flux redistribution towards the equilibrium state, followed by a strong heating of the superconductor. From a macroscopic point of view, this means that a sudden penetration of the magnetic field inside the superconductor occurs, which can even induce the SC material to switch from superconducting to normal state. It is well known that the flux jump occurrence is provoked, for instance, by small temperature fluctuations or variations in the external magnetic field [115, 116]. Moreover, their occurrence probability is affected by the ramp rate of the external applied magnetic field and by the working temperature [118, 119]. In general, two types of flux jumps can be defined, namely local and global flux jumps. The former occurs in a small fraction of the sample volume, the latter involves vortices in motion in the entire volume of the sample [120]. Moreover, depending on the initial perturbation and the driving parameters there are two qualitatively different types of global flux jumps, namely, partial and complete flux jumps. The former self-terminates when the temperature is still lower than the critical temperature. The latter turns the superconductor to the normal state.

Several theories to explain flux-avalanche phenomena, based on the critical state model and local adiabatic assumption, were developed during the last century. Swartz and Bean [116] extended the critical state model proposed by Bean to include heating effect, presenting their adiabatic critical-state model. One of the most important results of this theory is the definition of the external magnetic field B_{fj} corresponding to the first flux jump. However, by not taking into account the magnetic field dependence of the current density, they described the phenomenon only partially and a more complex field-dependence relationship for the critical current density is needed. Müller and Andrikidis [121] calculated the magnetization loops with flux jumps for Y-Ba-Cu-O superconducting slabs, demonstrating that the assumption of a magnetic field dependence of the critical current density in the calculations is necessary to properly reproduce the experimental data. In 1996, Mints proposed an approach based on the Bean critical state model introducing the instability criterion $\delta W > \delta Q$, where δQ is the heat release due to the fluxon motion and δW is the additional cooling heat flux to a cryogenic coolant at the sample surface [120]. From this assumption, for an infinite Type II superconducting slab, B_{fj} results to be proportional to the ramp rate $\dot{H}_{app}$ of the external applied magnetic field as $B_{fj} \propto \dot{H}_{app}^{-1/2}$. According to the model proposed by Mints [120, 122], the mechanism underlying the flux jump can be described as follows. To a first approximation, we can consider a critical current density dependent only on temperature $J_c = J_c(T)$. In the framework of the Bean model, for a long superconducting cylinder subjected to an external magnetic field, the spatial distribution of flux follows Equation 2.8, namely

$$\frac{\partial B_z}{\partial r} = \mu_0 J_c \qquad or \qquad \frac{\partial B_z}{\partial r} = 0 \tag{2.38}$$

When the hopping mechanism arises, the moving fluxons can determine a local heating of superconductor due to the viscous drag, in a similar way to the conventional Joule heating. Suppose that, because of this amount of initial heat δQ_0 released, the initial superconductor temperature T_0 is increased by a small perturbation δT_0. From GL theory, we know that the critical current density $J_c(T)$ is a decreasing function of temperature. Hence, the density of the screening current decreases as the temperature increases, namely it is lower at $T = T_0 + \delta T_0$ than at $T = T_0$. This reduction allows the magnetic field to penetrate more deeply in the superconductor (Figure 2.9).

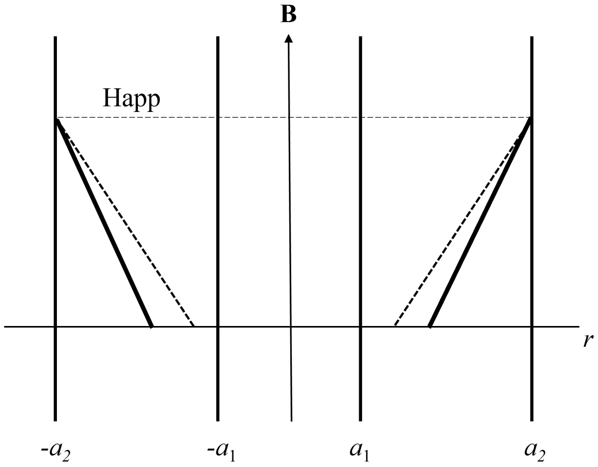

Fig. 2.9 Magnetic-field B(r) distribution in a tube (see Figure 2.4) at different temperatures: $T = T_0$ (solid line), $T = T_0 + \delta T_0$ (dashed line).

Indeed, due to the motion of magnetic flux into the superconductor, an electric field perturbation δE_0 is induced, which in turns causes an additional heat release δQ_1. The former leads to an additional increase of temperature, δT_1 which provokes a reduction of the critical current. This iterative process can result in an avalanche-type increase of the temperature and magnetic flux in the superconductor, i.e. in a global flux jump. In order to properly characterize the correlation between the temperature and electromagnetic field increasing during the flux jump, the magnetic and thermal diffusion coefficients, D_m and D_t respectively, can be introduced. Their ratio, $\tau = D_t/D_m$, is defined as:

$$\tau = \mu_0 \frac{k\sigma}{C} \tag{2.39}$$

where k is the heat conductivity, σ is the electric conductivity, and C is the heat capacity of the superconductor. Two limiting cases can be realized in a superconductor. The former, for $\tau \ll 1$ ($D_t \ll D_m$), corresponds to a fast propagation of flux with an adiabatic heating of the superconductor (*adiabatic condition*). For $\tau \gg 1$ ($D_t \gg D_m$), the spatial distribution of the flux is fixed during the rapid heating (*dynamics condition*). Relying on these definitions, Mints and Rakhmanov [122] identified the two conditions as peculiar to Type II and superconducting composites (materials containing a combination of normal and superconducting materials), i.e. Type II are characterized by $\tau \ll 1$ condition whereas superconducting composite by $\tau \gg 1$. The dynamic condition $\tau \gg 1$ ($D_t \gg D_m$) typical for the superconducting composite can be achieved with the characteristic value at low temperature of $D_m = 10^{-5} - 10^{-6}$ m^2/s and $D_t = 10^{-1} - 10$ m^2/s resulting in the rapid heating stage taking place while the magnetic flux lines are stationary[120]. For Type II superconductors, the adiabatic condition $\tau \ll 1$ ($D_t \ll D_m$) can be reached with the typical values at low temperature of $D_m = 10^{-2} - 10$ m^2/s and $D_t = 10^{-4} - 10^{-3}$ m^2/s. This means that the magnetic flux diffusion is considerably faster than that of the heat flux and consequently the heating of hard superconductors with a rapid variation of magnetic flux can be assumed adiabatic [122].

From a practical point of view, the flux jump phenomenon represents a big hurdle. Indeed, the abrupt penetration of the flux lines in the superconductor and the possible consequent transition to the normal state lead to quench processes that can deteriorate the material and device performances. The developing of normal zones inside the HTSs is helped where local perturbations arise, such as a localized thermal load (radiation heat, beam energy deposition, AC losses, inductive coupling with another quenching magnet system, etc.) or microscopic conductor defects that either pre-existed from manufacturing or suddenly or gradually developed under mechanical stress [123, 124]. For this reason, a lot of efforts have been made in order to reduce the flux-jump occurrence, both improving the material properties such as the thermal conductivity and optimizing the manufact shape [125–127] and its thermal contact with the coolant.

With these aims, it is necessary to thoroughly investigate the flux avalanche occurrence conditions as well as their evolution in order to strengthen the critical state stability against flux-jumps. To do this, it is essential to understand and simulate the in-field behaviour of a SC device in order to predict its characteristics and optimize its thermal anchoring and architecture for the particular application. Since relying on appropriate simulation tools can be a successful approach to fully comprehend the inherent electromagnetic-thermal behaviour of SC materials [128], computational approaches have been used in the past few years with the aim of recreating and predicting the flux jump phenomenon [129–132]. The models are based on the general idea that the electromagnetic equations (Maxwell equations) and the thermal equations have to be coupled. The thermal behaviour and the changes in the local value of temperature in the superconducting domain are usually described by the heat diffusion equation:

$$\nabla(\kappa(T)\cdot\nabla T) - C(T)\cdot\rho_m\cdot\frac{\partial T}{\partial t} + Q = 0 \tag{2.40}$$

where $Q = \mathbf{E}\cdot\mathbf{J}$ gives the volumetric heating rate and $\kappa(T)$, $C(T)$ and ρ_m are the thermal conductivity, specific heat and mass density, respectively. Moreover, in order to properly described the superconductor behaviour and the evolution of the thermo-magnetic instabilities, both the current density dependence on the magnetic field **B** and temperature T must be considered. This means that the parameter J_{c0} in the **J**-**B** relations reported in Table 2.1, or more in details in Equations 2.36 and 2.37, has to be supposed dependent on the temperature, $J_{c0}(T)$ [130, 110].

Chapter 3

Materials and experimental procedures

3.1 Magnesium diboride (MgB_2)

In 2001 Nagamatsu *et al.* [133] discovered the superconducting behaviour of the magnesium diboride (MgB_2). In the last few years, MgB_2 has gained much attention for shielding applications [27, 60], due to the low-cost and non-toxic precursors not including rare earth elements, the low weight density, and the long coherence length. In particular, the last characteristic implies that clean grain-boundaries do not prevent the flow of high current densities, thus opening the employment of large polycrystalline manufacts - fabricated by in situ or ex situ sintering processes [134–137, 64] or by infiltration processes [60, 138, 139] - for large scale applications. MgB_2 possesses a AlB_2-type hexagonal crystal structure that belongs to P6/mmm space group and the dimensions of the unit cell are a = b = 3.086 Å and c = 3.524 Å. As shown in Figure 3.1, the boron atoms are arranged in layers, with layers of Mg interleaved between them. The structure of MgB_2 is composed of alternate boron and magnesium hexagonal layers along the c axis [133]. The crystal structure of MgB_2 determines a theoretical density of 2.57 g/cm^3 [133].

Since its discovery, different fabrication routes have been proposed in order to optimize the superconducting properties of MgB_2 samples. Between them, chemical substitution and impurities addition have shown good results, enhanced the values of the upper critical field H_{c2} and the current density J_c introducing new point defects

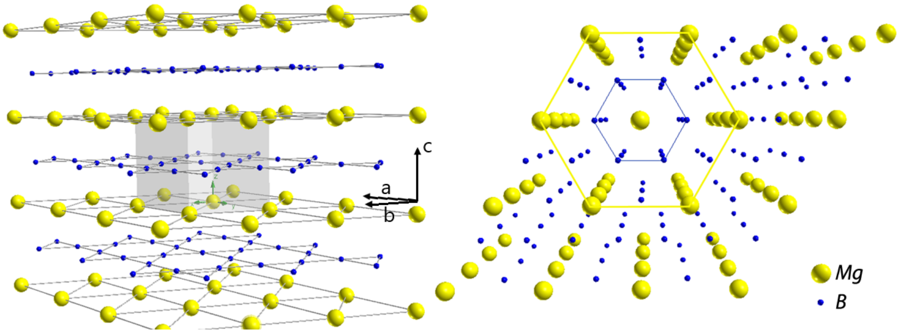

Fig. 3.1 Crystal structure of MgB_2.

capable of pinning more vortices [140, 141]. The peculiar feature of MgB_2 is the presence of two bands and energy gaps, which causes the upper critical field in clean MgB_2 to be low and anisotropic. Typical H_{c2} values at low temperatures are around 3 T for $H^{||c}$ and 16 T for $H^{||ab}$. From the relationship $H_{c2}^{||c} = \Phi_0/(2\pi\xi_{ab}^2)$ and $H_{c2}^{||ab} = \Phi_0/(2\pi\xi_{ab}\xi_c)$, where Φ_0 is the quantum magnetic flux in each vortex, it follows that the coherence length has an anisotropic behaviour as well, in particular along the *ab* plane $\xi_{ab} \approx 10$ nm and along the *c* axis $\xi_c \approx 4$ nm. The values of ξ results to be higher than both the interatomic spacing and the typical grain boundary thickness, with a positive impact on the applications as detailed below. Conversely, at low temperature the penetration depth, λ, presents an isotropic behaviour, with a typical value of $\lambda \approx 100$ nm. Moreover, according to the standard anisotropic Ginzburg-Landau theory the bulk anisotropy $\gamma = \lambda_c/\lambda_{ab} = \xi_{ab}/\xi_c = H_{c2}^{||ab}/H_{c2}^{||c}$ is not universally constant, but it systematically decreases with increasing temperature and shows a pronounced field dependence near T_c [142, 143].

The study of the trend of $J_c(H,T)$ in polycrystalline samples and in dispersed powders has shown that the microscopic current density in densified bulks is almost identical to the intragranular, one relative to a powder: the current is therefore not limited by the presence of grain boundaries, which in general severely limit the performance of the HTSs. Since the MgB_2 coherence length is larger than the typical grain boundaries thickness, MgB_2 shows to be free from weak link effects and the connections between the grain is a key point to prevent a J_c reduction in polycrystals. This property allows overcoming the limitations evidenced by the HTSs, which require a grain alignment, achievable with epitaxial growth techniques.

In order to enhance the connectivity, a number of strategies have been pursued: improving the density by the application of an external pressure during the synthesis; limiting the presence of impurity phases at grain boundaries by using high-purity elements; limiting the formation of the amorphous MgO layer on the grain surface by performing the synthesis in controlled atmosphere; increasing the grain size in order to reduce the exposed surface of the grains; and texturing the MgB_2 phase by mechanical means or grain orientation under magnetic field [144–146]. Consequently, the synthesis method highly affects the superconducting performances of MgB_2 samples.

The production methods for MgB_2 bulk can be of two types:

- ex-situ processes: use the MgB_2 powder to fabricate bulks through sintering;
- in-situ processes: the reaction between B and Mg occurs simultaneously with the bulk formation.

Among the ex-situ processes, the most employed for MgB_2 fabrication bulk are Powder in-tube technique (PIT), Uniaxial Hot Pressing (HP) and Spark Plasma-Sintering (SPS). The MgB_2 powder is obtained through a milling process of MgB_2 sample with great granulometry through Mg diffusion into boron. The resulting powder shows different features depending on the precursor granulometry and characteristics.

In PIT, a metallic capsule is filled in with powder and the capsule is subjected to drawing/rolling followed by a thermal treatment. Using PIT techniques, Aldica *et al.* [147] obtained MgB_2 samples characterized by a nominal density of 2.55 g/cm^3. The Rietveld method allowed them to estimate the average crystallite size of MgB_2, i.e. 125 nm. The samples showed the presence of minority phases: MgB_4 (10.1%) and MgO (7.1%).

HP is performed in a rigid die using loading along the vertical axis on punches pressurized from an external hydraulic system. Although the pressure is applied along the vertical axis, there is a radial pressure against the die wall. The differential stress between the axial and radial directions generates shear that is effective in particle bonding. This shear stress is proportional to the applied stress. Initial densification includes particle rearrangement and plastic flow. As densification progresses, creep by grain boundary diffusion and volume diffusion becomes controlled [148].

The SPS method involves the consolidation of the samples, previously in the form of powders, through the simultaneous use of current, pressure, and temperature. The powders are placed inside a mould, typically made up of graphite. The passage of current through the mould and the sample leads to a further local increase of temperature; at the same time, the sample is subject to a pressure causing the formation of the bulk. The literature reports, among the various advantages in the use of the SPS, a greater density of the obtained materials, a smaller grain dimension and cleaner grain boundaries [149].

Häßler *et al.* [150] compared the features of MgB_2 samples obtained through SPS and HP. All the samples are characterized by the presence of MgB_4 and MgO phases, even if with different percentages. Both methods show a correlation with a previous milling process of MgB_2 powder, that could help to obtain better bulk. This work suggests that the sample obtained with SPS technique has the best grain–grain connections and mass density.

Despite the improvements in the fabrication processes, thermomagnetic instabilities still occur at low operating temperatures. In MgB_2, the adiabatic condition $D_t \ll D_m$ (see Section 2.8) is verified at low temperatures due to the low heat capacity and thermal conductivity of this compound [151–154, 64]. Chabanenko [155] estimated the value of the thermal and magnetic diffusivity at 4.2 K, namely $D_t(4.2K) \approx 6 \cdot 10^{-4}$ m^2/s and $D_m(4.2K) \approx 3.2 \cdot 10^{-3}$ m^2/s, demonstrating that the adiabatic conditions are fulfilled also for a polycristalline MgB_2 bulk.

Thermo-magnetic instability-driven flux avalanches in MgB_2 have been revealed by several techniques in films, tapes, and bulks [156–162]. Their occurrence probability is affected by the ramp rate of the external applied magnetic field and by the working temperature [118, 119]. Moreover, Aldica *et al.* [163] showed that fabrication parameters, such as the heating temperature in Spark Plasma Sintering (SPS) process, can influence the flux jump occurrence in bulk MgB_2, as well. The flux-jump occurrence drastically deteriorates the intrinsic capacity of a superconductor to shield magnetic fields [131, 64], becoming the major factor limiting the shielding performance at low temperatures [117].

3.2 MgB_2 samples

For this PhD project, a tube- and a cup-shaped MgB_2 bulks were manufactured at the National Institute of Materials Physics in Magurele, Romania (Prof. Badica's group). The aim was to obtain superconducting vessels with an aspect ratio of height to external diameter close to unity and characterized by high performing magnetic shielding properties. Moreover, the low weight density of MgB_2, make these shields suitable for applications where practical requirements of a small size, low weight and a high shielding factor are needed, such as aerospace applications [27].

For both the geometries, commercial MgB_2 powders were mixed with hexagonal boron nitride powder (BNh). The powders were loaded into a graphite die system of ≈20 mm inner diameter and processed by spark plasma sintering (SPS) (FCT System GmbH—HP D 5, Germany) at 1150 °C for a dwell time of 8 min and the maximum pressure applied on the sample during sintering was 95 MPa [1, 164, 165]. As demonstrated in [165, 166], the addition of the BNh improves the SPS bulk machinability while leading to a reduction of the thermal conductivity that, as one can see later, get the thermomagnetic instabilities problem worse. For tube-shaped bulk, the cylinder was drilled by using bits with different radii. The inner radius of the final product was obtained by means of a lathe machine. The final product have the following dimensions: height h=17.5 mm, inner radius R_i=7.0 mm, external radius R_e=10.15 mm (Figure 3.2). The sample, obtained starting from MgB_2 powder with a pristine phase concentration of 87.9 [$wt.\%$], presents a final density ≈ 2.45 g/cm^3 and an aspect ratio $AR=h/R_e=1.75$.

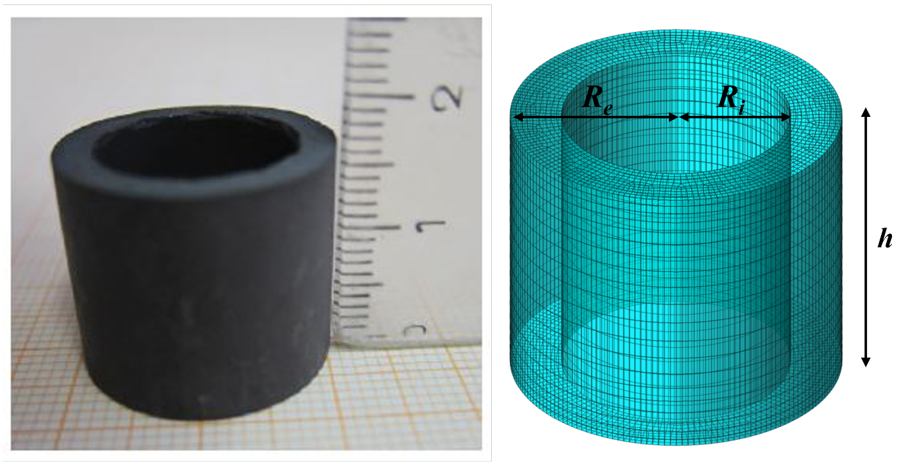

Fig. 3.2 Picture of the tube-shaped MgB_2 shield (left) and its schematic view (right). Its dimensions are: height h=17.5 mm, inner radius R_i=7.0 mm, external radius R_e=10.15 mm.

The cup-shaped sample was obtained by a cylinder (25 mm in height) which was partially bored by using drill bits, and then it was refined in the final cup-shape by means of a lathe machine. The final dimensions of the sample are: inner radius R_i=7.0 mm, external radius R_e=10.15 mm, external height h_e=22.5 mm, internal depth d_i=18.3 mm (Figure 3.3). The sample presents a final density $\approx$ 2.50 g/cm^3, obtained with an MgB_2 powder with a pristine phase concentration of 97 [*wt.%*], and an aspect ratio AR=h_e/R_e=2.25 and AR'=d_i/R_e=1.83.

Fig. 3.3 Picture of the cup-shaped MgB_2 shield (left and center) and its schematic view (right). Its dimensions are: inner radius R_i=7.0 mm, external radius R_e=10.15 mm, external height h_e=22.5 mm, internal depth d_i=18.3 mm.

3.3 Experimental setup and characterization details

The samples were characterized following the same procedure. In both cases, the MgB_2 bulk samples were placed in tight thermal contact with the second cold stage of a cryogen-free cryocooler. In order to guarantee an optimal thermal contact between the sample and the sample holder, the sample was covered by an indium layer, whose thermal properties are good enough to ensure an excellent thermal contact. The second cold stage was inserted in a thermal shield in order to reduce the heating by radiation. During the characterization, the sample was in vacuum and the cryostat chamber was positioned in the bore of a superconducting cryogen-free solenoid (CRYOMAGNETICS INC, 6T Cryo-Free Magnet System, W.O. # 3888-C) (Figure 3.4).

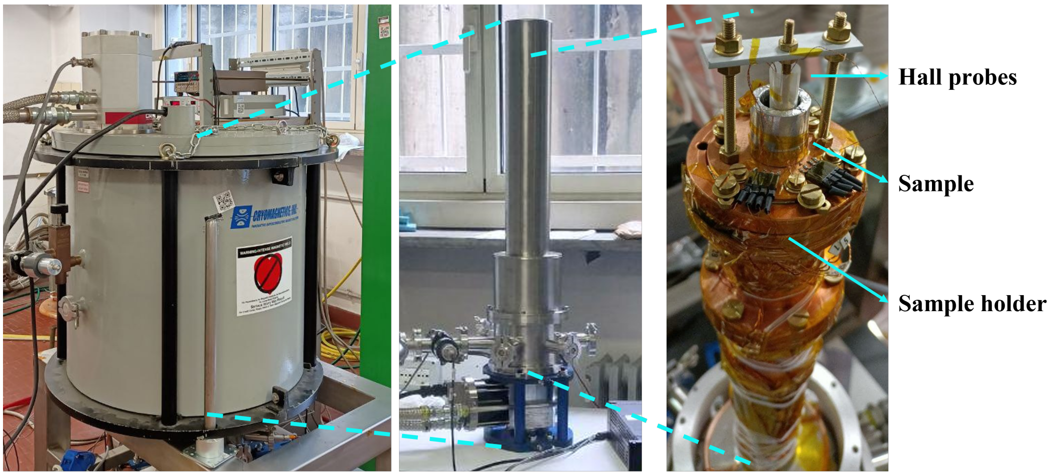

Superconducting magnet **Vacuum chamber**

Fig. 3.4 Experimental setup. From left to right: the superconducting magnet, the vacuum chamber and the sample holder on which the sample and the Hall probes are placed.

The shielding properties of the samples were investigated in both axial field (AF) and transverse field (TF) orientation (Figure 3.5 (a) and (b) respectively). In the former case, the sample was placed with its axis parallel to the coil axis, whereas for the TF characterization the sample was placed with its axis perpendicular to the coil axis (Figure 3.5).

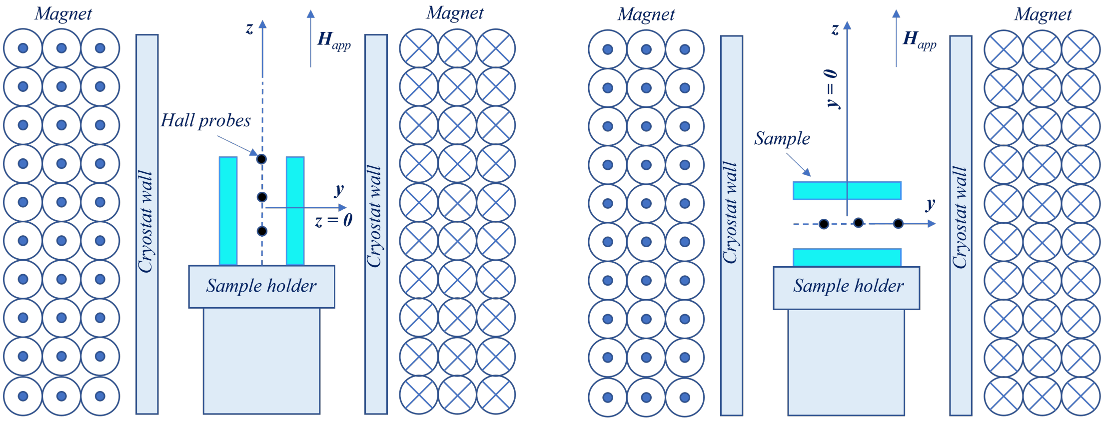

(a) AF **(b) TF**

Fig. 3.5 Schematic drawing of the experimental setup (not to scale) for the Axial (a) and Transverse (b) magnetic field configurations.

The magnetic flux density was measured by cryogenic Ga–As Hall probes, with a sensitivity of 5.2 Ω/T, located along the sample axis in the positions reported in Figure 3.6. For the cup-shaped sample the Hall probes (*hp*) were positioned at different distances from the closed extremity of the cup (*hp*=0), namely hp_1 = 1.0 mm, hp_2 = 5.0 mm, hp_3 = 9.2 mm (corresponding to the shield centre), hp_4 = 13.7 mm, and hp_5 = 18.3 mm (corresponding to the shield open extremity). The positions were left unchanged for both the AF and TF orientations. Otherwise, for the tube-shaped sample the Hall probes (*hp*) were positioned at different distances from the centre of the tube, namely hp_1 = 0 mm (SC shield centre), hp_2 = 4.4 mm and hp_3 = 8.8 mm (SC shield edge coordinate), left unchanged both in AF and TF orientation; hp_4 = 13.1 mm and hp_4 = 12 mm in AF and TF orientation respectively. For both AF and TF orientations, the probes were always oriented to measure the component of the magnetic flux density parallel to the applied magnetic field. The Hall probes voltage was measured by a 2182 A Keithley nanovoltmeter coupled to an 8-channel Keithley 7001 scanner and the acquisition system were controlled and/or driven by a Labview interface. The measurements were collected in zero field condition (ZFC), i.e. after cooling the sample in zero field, the applied field was cycled keeping fixed the sample temperature while the magnetic flux density was recorded.

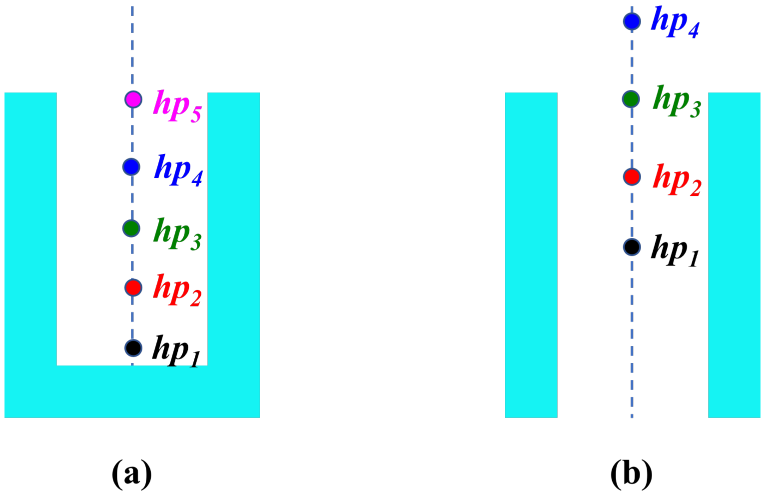

Fig. 3.6 Sketch of the position of the Hall probes along the axis of the cup – (a) and tube-shaped shields (b).

3.4 Critical current density evaluation

In order to properly characterize the SC samples, the evaluation of the critical current density, J_c, is needed. The aim of this estimation is twofold: the value of the critical current density is a fundamental information to determine the potential application of a superconducting sample; moreover, as it will be shown below, this parameter is necessary to model the superconducting behaviour of the sample by a numerical approach. In this work, taking advantage of the tubular geometry of the samples, the value of J_c was calculated from the magnetic flux density cycles relying on the approach proposed by Bartolomé *et al.* for finite superconducting rings [167]. Applying the Bean model to this specific geometry, they proposed to determine the critical current density as:

$$J_c = \frac{\Delta B_c}{\mu_0 f(R_e, R_i, h, z)} \tag{3.1}$$

where $\Delta B_c = B_c^+ - B_c^-$ is the magnetic flux density cycle width measured at a given applied field in the axial field configuration (Figure 3.7 is reported as example) and the function f provides the dependency of J_c on the geometry of the sample:

$$\begin{aligned} f(R_e, R_i, h, z) = & \left[\frac{h}{2} - z\right] \ln\left[\frac{R_e + \sqrt{R_e^2 + (z - h/2)^2}}{R_i + \sqrt{R_i^2 + (z - h/2)^2}}\right] \\ & + \left[\frac{h}{2} + z\right] \ln\left[\frac{R_e + \sqrt{R_e^2 + (z + h/2)^2}}{R_i + \sqrt{R_i^2 + (z + h/2)^2}}\right] \end{aligned} \tag{3.2}$$

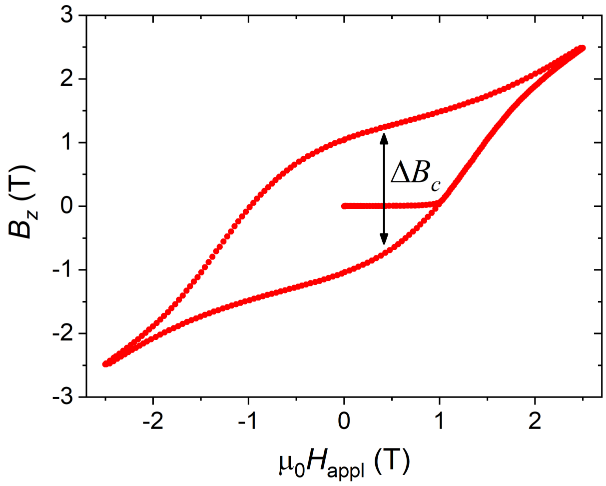

Fig. 3.7 Example of a magnetic flux density loop measured while the external applied field was cycling at axial field orientation. The cycle width ΔB_c is also shown.

For the tube-shaped bulk R_e and R_i are the external and inner radii of the tube, respectively, h is the tube height and z the distance from the tube centre (i.e. hp_1 in Figure 3.6(b)). The J_c calculations were made using the magnetic flux density cycles measured in the centre of the tube, i.e. at hp_1 position (Figure 3.6(b)). Conversely, for the cup-shaped sample R_e and R_i are the external and inner radii of the cup respectively, z is the distance from the cup centre (i.e. hp_3 in Figure 3.6(a)) and h is the cup internal depth. In order to neglect the effects of the cup closure, J_c was obtained applying Equation 3.1 to the magnetic flux density cycles measured in the outer position of the cup, i.e. hp_5 in Figure 3.6(a). The J_c vs. applied field curves obtained with this procedure are plotted in Figure 3.8 (solid lines). This figure also shows the J_c curves obtained from magnetic flux density measurements performed at the National Institute of Materials Physics (Magurele, Romania) on two small pieces (open symbols) cut from the same MgB_2 cylinders as the tube/cup-shaped shields, respectively. The agreement between the two sets of data is remarkable. Notably, the cup shows higher critical current density values than the tube for the same temperature and applied field values, which can be ascribed to the different MgB_2 phase concentrations presented in the starting powders (97 [wt.%] for the cup against 87.9 [wt.%] for the tube).

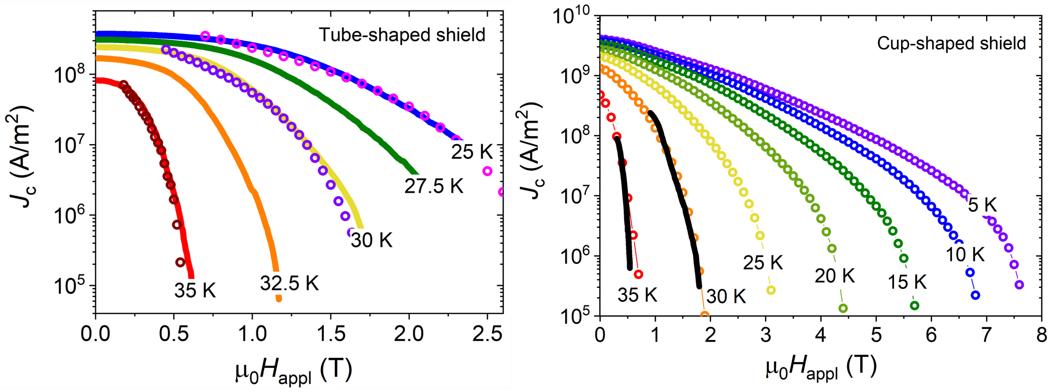

Fig. 3.8 $J_c(B)$ calculated by Equation 3.1 (solid lines) and extracted from magnetic flux density cycles performed on small pieces (open symbols) cut from the same MgB_2 cylinders as the tube/cup-shaped shields, respectively.

3.5 Ferromagnetic material and hybrid configuration

In order to improve the shielding properties of the superconducting sample, a coaxial FM layer was superimposed on the tube-shaped shield shown in Figure 3.2. Figure 3.9 shows a sketch of this hybrid configuration. The centres of the two shields coincide but the FM shield is shorter than the SC one, being the difference between the edges Δh=3.5 mm. This new configuration was experimentally characterized with the same procedure used for the only SC tube-shaped bulk and the magnetic flux density was measured in the same positions along the axis of the SC tube alone (Figure 3.6(b)). On the other hand, the choice to investigate the addition of the FM sheet with height lower than the SC one relied on previous studies, in which better results were obtained when the SC shield protruded over the FM one [168, 169, 71].

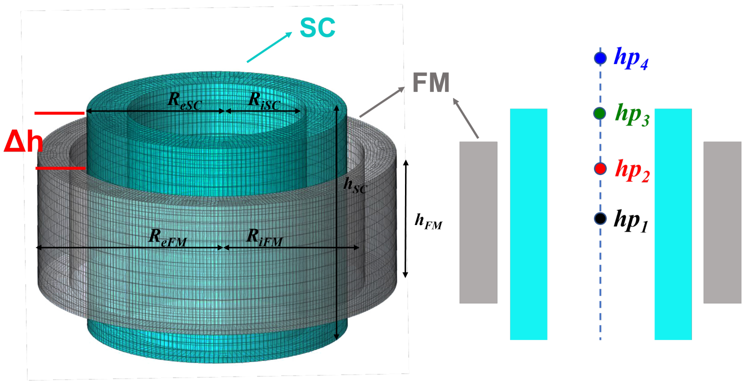

Fig. 3.9 Schematic view of the hybrid tube-shaped shield and of the position of the Hall probe placed along its axis. The SC tube dimensions are the same as in Figure 3.6(b) while the FM tube dimensions are: height h=10.5 mm, inner radius R_{iFM}=11.5 mm, external radius R_{eFM}=14 mm. The Hall probe were placed at the same positions as for the characterization of the SC tube alone (see Section 3.3).

The ferromagnetic shell experimentally characterized is made out of iron ARMCO whose B–H characteristic curve is plotted in Figure 3.10. Its relative permeability at low fields overcomes the value $\mu_r = 7500$, while its saturation magnetic flux density is ≈ 2.3 T. The sample was preliminary degaussed by means of a thermal treatment in vacuum atmosphere at 760 °C for 1 hour. A degaussing procedure was also performed before each characterization process, applying an alternating magnetic field.

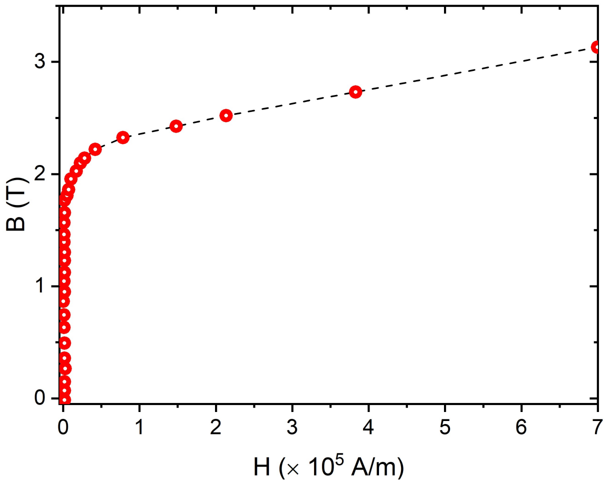

Fig. 3.10 B–H characteristic curve of the iron ARMCO used for the FM shield.

Chapter 4

Experimental results

In this chapter, the experimental results of the magnetic characterization are presented for each configuration (SC tube, SC cup and SC+FM tubes Figure 3.6(a), (b) and Figure 3.9 respectively) tested for the two applied field orientations, i.e. AF and TF [137, 64]. The shielding ability of all the configurations were evaluated for different operational temperatures in the range 20 - 35 K . However, for all the considered geometries, I mainly focused on the results obtained at the operational temperature T_{OP}=30 K, which is a good compromise between the need to achieve high shielding performance and the requirement of high working temperatures. In the next section, the screening abilities of the SC shields are presented, specifically the SC tube performance in Subsection 4.1.1 and that of the SC cup in Subsection 4.1.2. Finally, the results obtained for the hybrid configuration, SC+FM tubes, are discussed in Section 4.2.

4.1 Superconducting shields

4.1.1 Tube-shaped shield

In this first section, the results obtained with the only SC tube (Figure 3.2) are presented. Figure 4.1 shows the magnetic flux densities measured at positions hp_1 and hp_3 positions (Figure 3.6) for different temperatures. From these pictures, two aspects clearly emerge: at the same temperature, the shielding capability of the tube gets worse as the temperature increases and it is much higher in AF orientation.

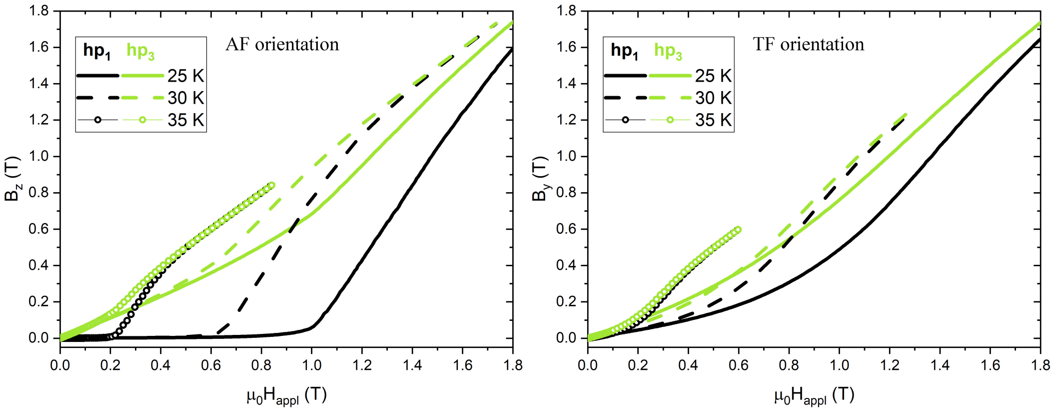

Fig. 4.1 Magnetic flux density measured as a function of the applied field at position hp_1 and hp_3 along the axis of the SC tube for the AF (left) and the TF (right) orientations and for different operational temperatures.

Focusing on the working temperature of 30 K, the magnetic flux density measured at different positions along the z-axis of the shield in both AF and TF orientations are displayed in Figure 4.2.

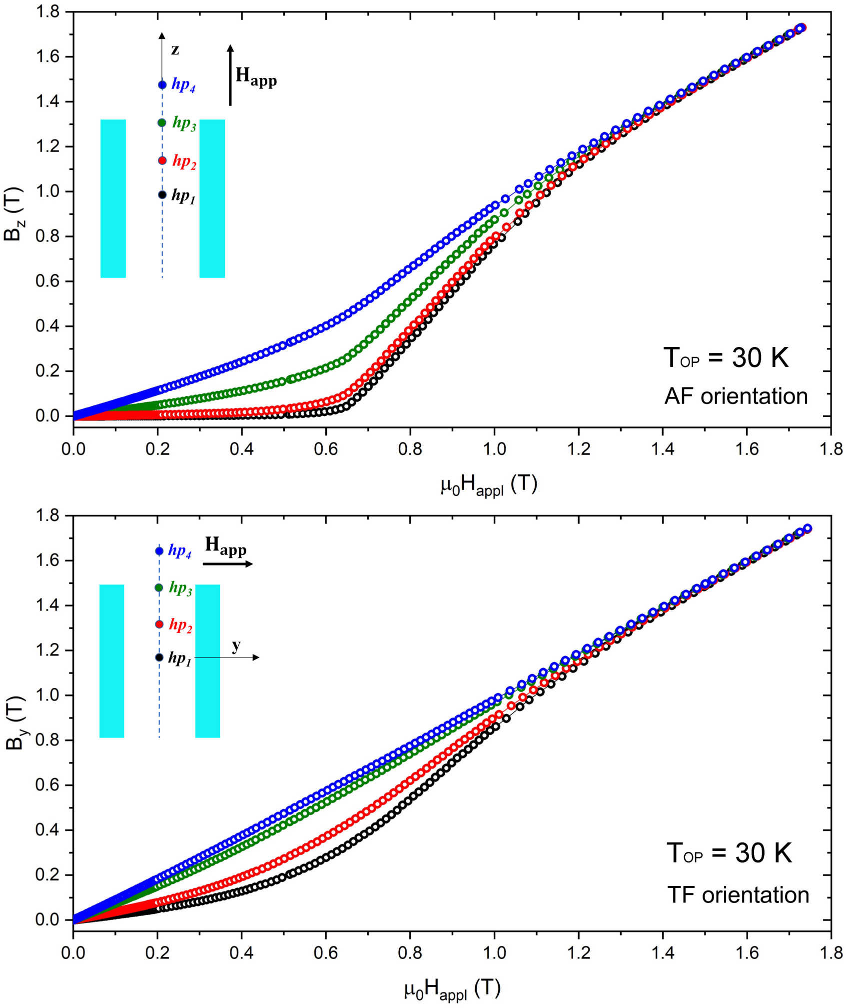

Fig. 4.2 Magnetic flux density measured at T_{OP}= 30 K as function of the applied field by the four Hall probes positioned along the tube axis.

In order to properly quantify and compare the shielding properties of the investigated shields, I introduced the Shielding Factor (SF), defined as the ratio of the applied magnetic field and the magnetic flux density measured by the Hall probes. Figure 4.3 shows the SF curves for each position along the tube axis evaluated in AF and TF orientations. In AF orientation, SFs greater than 10^2 up to $\mu_0 H_{app} \approx 0.4$ T were measured in the centre of the tube (position hp_1). As expected, in TF orientation the performances of the shield are worse than those obtained in AF and, considering the innermost position hp_1, the SF values lie between 4 and 5, for applied field lower than 0.2 T.

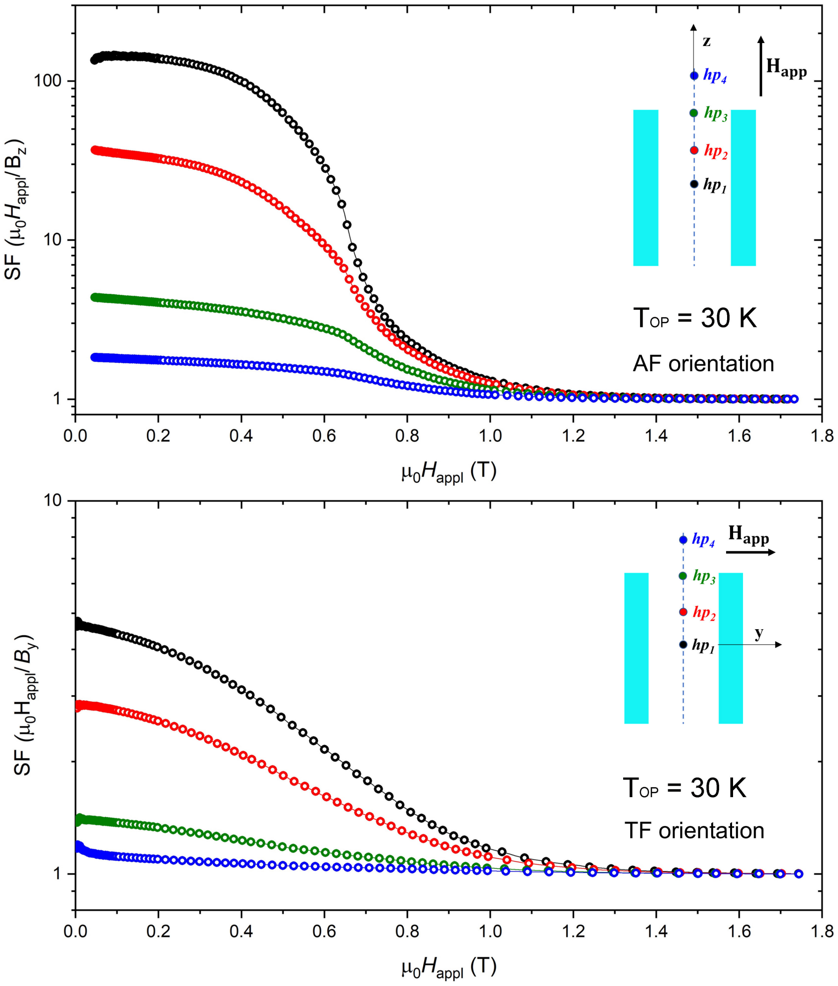

Fig. 4.3 SF curves measured at T_{OP}= 30 K as function of the applied field by the four Hall probes positioned along the tube axis.

4.1.2 Cup-shaped shield

Following the same procedure, the shielding ability of the cup-shaped shield was evaluated at different temperatures in the range 20 - 35 K. Figure 4.4 shows the magnetic flux density measured at position hp_1, in both AF and TF orientations at all the investigated temperature. As for the tube case, also in this case the shielding ability of the cup is lessened when a transverse field is applied. Note that in the AF orientation, the shielding performances experience an abrupt worsening, due to the flux jump occurrence.

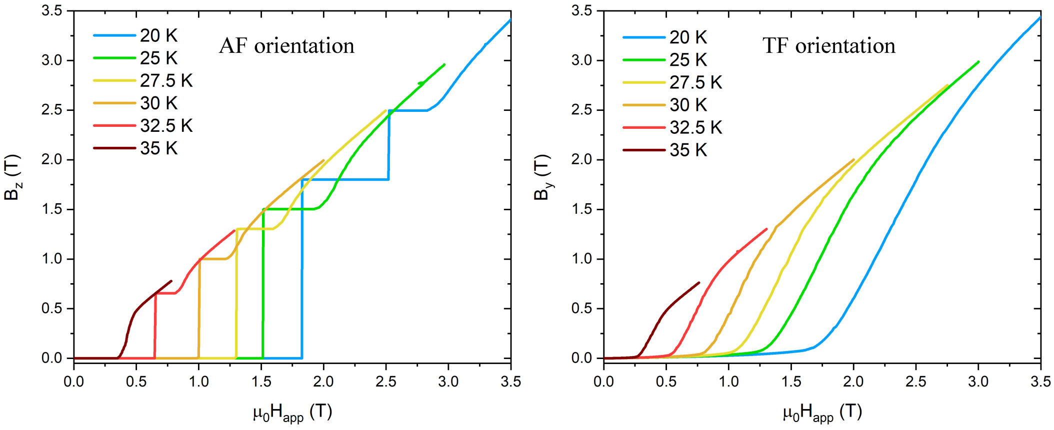

Fig. 4.4 Magnetic flux density measured at position hp_1 along the axis of the SC cup for AF (left) and TF (right) orientations and for different operational temperatures.

Focusing on the working temperature T_{OP}=30 K, the magnetic flux density dependence on the applied magnetic field measured by all the Hall probes is shown in Figure 4.5, while Figure 4.6 illustrates the corresponding SF values.

In the AF orientation, despite the occurrence of a flux jump at $\mu_0 H_{app} = 1$ T, SF values grater than 10^4 up to $\mu_0 H_{app} = 1$ T are obtained at the innermost position hp_1. Otherwise, a SF≈50 is achieved in TF orientation at position hp_1 for $\mu_0 H_{app} < 0.2$ T.

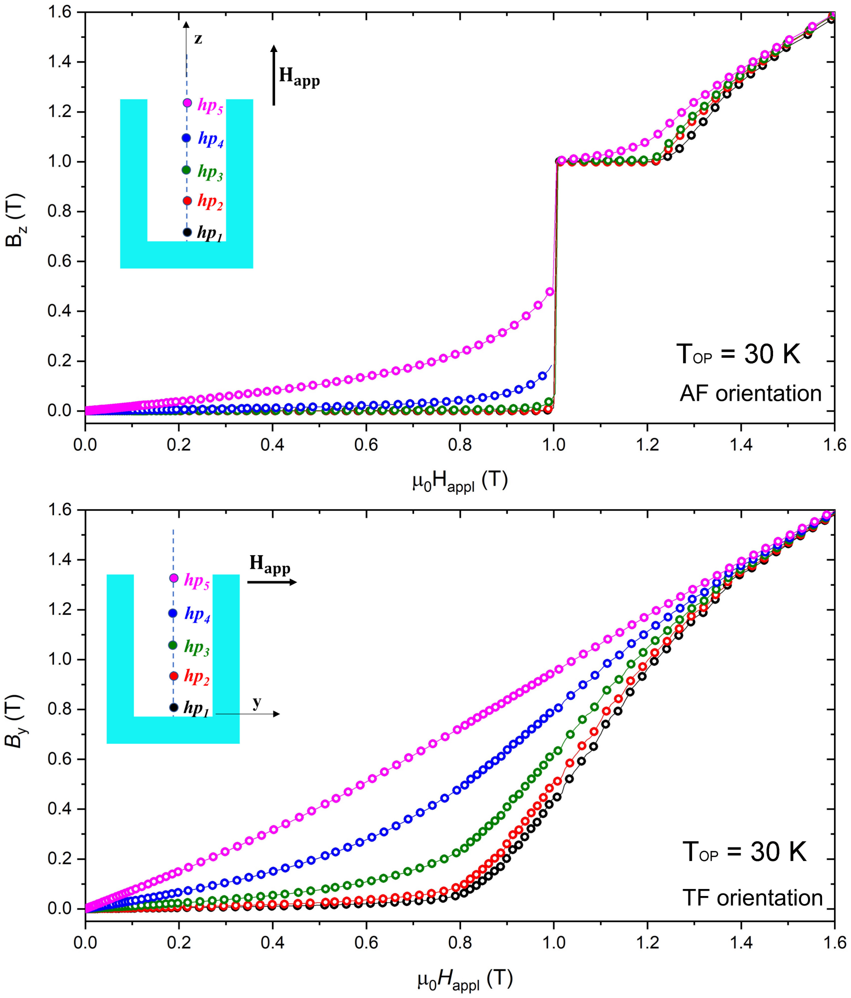

Fig. 4.5 Magnetic flux density measured at T_{OP}= 30 K as function of the applied field by the five Hall probes positioned along the cup axis.

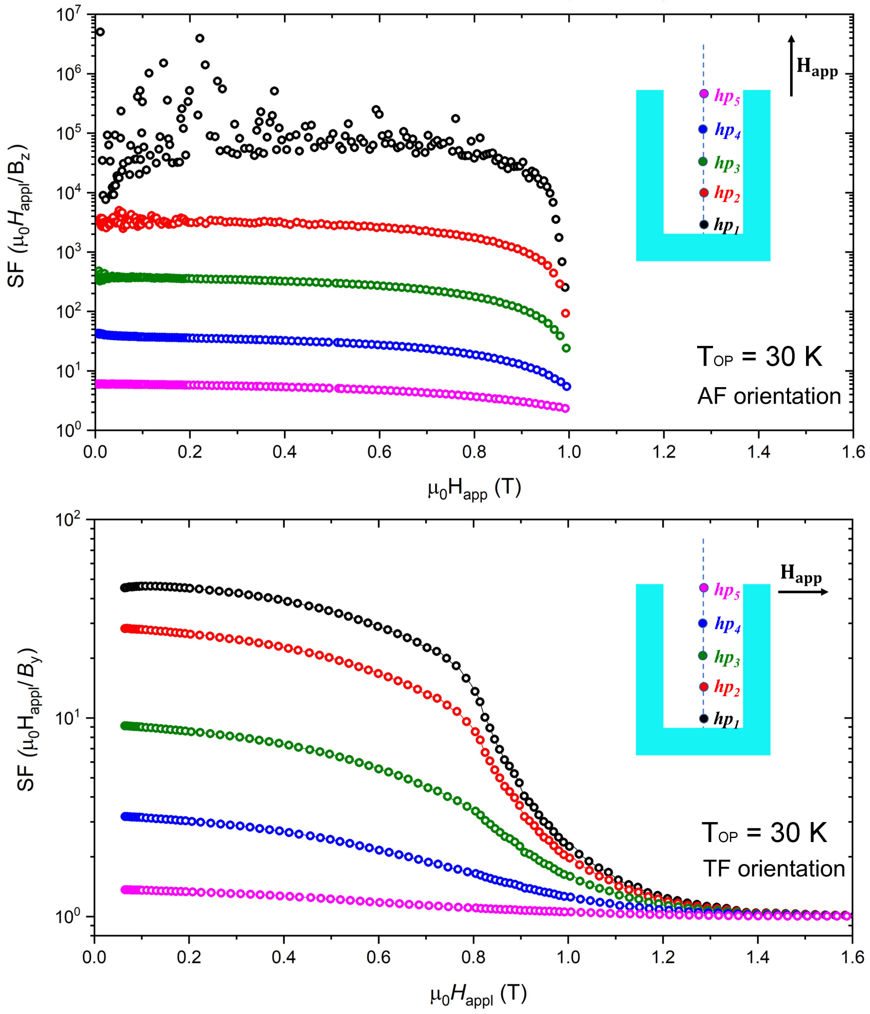

Fig. 4.6 SF curves measured at T$_{OP}$= 30 K by the five Hall probes positioned along the cup axis as function of the applied field.

In order to better visualize the shielding capability evolution with temperature, let me define a threshold field, $\mu_0 H_{app,lim}$, as the applied field above which the shielding factor drops below a reference value. Figure 4.7(a) shows the $\mu_0 H_{app,lim}$ dependence on temperature in AF orientation, having chosen as reference values SF=10^4 for position hp_1, 10^3 for position hp_2, and 10^2 for position hp_3. Remarkably, at 20 K, SF $> 10^4$ up to $\mu_0 H_{app}$ = 1.8 T was achieved near the closed extremity (Figure 4.7(a), position hp_1), while in the same range of applied fields, the SF values remain higher than 10^2 all the inner half of the shield (Figure 4.7(a), position hp_3).

In the same way, I specified three threshold fields for the TF orientation as the applied field above which the shielding factor goes below 40 (for position hp_1), 20 (for position hp_2) and 7 (for position hp_3). In figure 4.7(b), these $\mu_0 H_{app,lim}$ values are plotted as a function of temperature. As can be seen, near to the cup closed edge (Figure 4.7(b), position hp_1), at 20 K SF is over 40 up to $\mu_0 H_{app}$ = 0.8 T, while in the same field range it is over 7 in correspondence to the cup centre (Figure 4.7(b), position hp_3).

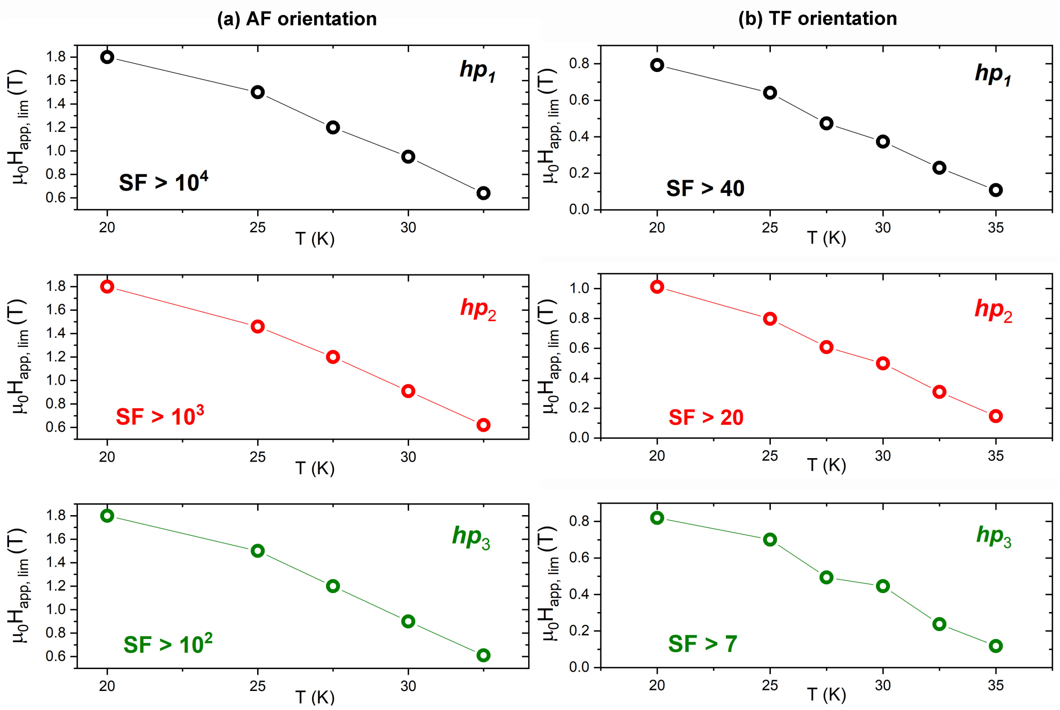

Fig. 4.7 Temperature dependence of the threshold applied fields, $\mu_0 H_{app,lim}$, above which the shielding factor drops below (a) 10^4 (for position hp_1), 10^3 (for position hp_2) and 10^2 (for position hp_3) in the AF orientation and (b) 40 (for position hp_1), 20 (for position hp_2) and 7 (for position hp_3) in the TF orientation.

4.2 Hybrid tube–shaped shield

It is well known that the superimposition of a ferromagnetic layer on the superconducting shield can enhance the shielding capability of the only superconducting shield [170, 171, 169, 4]. Moreover, it was demonstrated that the FM shield results to be more efficient when a transverse magnetic field is applied. Indeed, unlike superconductors [5], long tubular shields of high-permeability materials are expected to mitigate transverse magnetic fields more effectively than axial ones [172], and significant SF improvements were predicted in a transverse field for an ideal

rectangular-shaped SC shield with an outer layer of μ-metal [52]. Taking advantage of this peculiarity, the effect of the addition of a ferromagnetic tubular shell around the superconducting tube-shaped shield was experimentally evaluated.
The shielding capability of this tubular hybrid configuration (SC+FM tube) at different temperature is displayed in Figure 4.8.

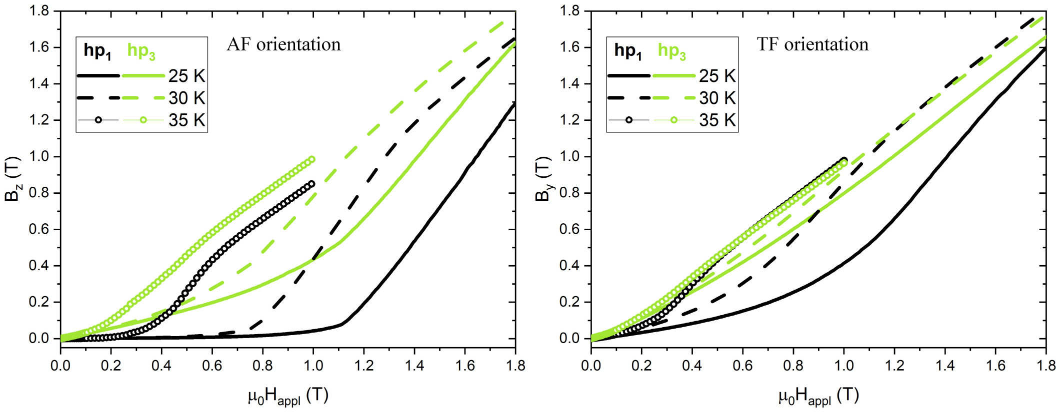

Fig. 4.8 Magnetic flux density measured at positions hp_1 and hp_3 along the axis of the SC+FM tube for the AF (left) and the TF (right) orientations and for different operational temperatures.

Despite the FM tube superimposition, here as well, the magnetic field mitigation ability of this hybrid shield is less powerful when a transverse field is applied, even if it is improved compared to that obtained with the only SC tube. Focusing on the results measured at 30 K, Figure 4.9 shows the magnetic flux density measured at different positions along the hybrid shield axis, while in Figure 4.10 SF values of the SC (open symbols) and SC+FM (solid symbols) configurations are compared. Note that the hp_4 shielding curve of the SC+FM shield in TF orientation is lacking, since there were some wiring problems with the corresponding Hall probe.

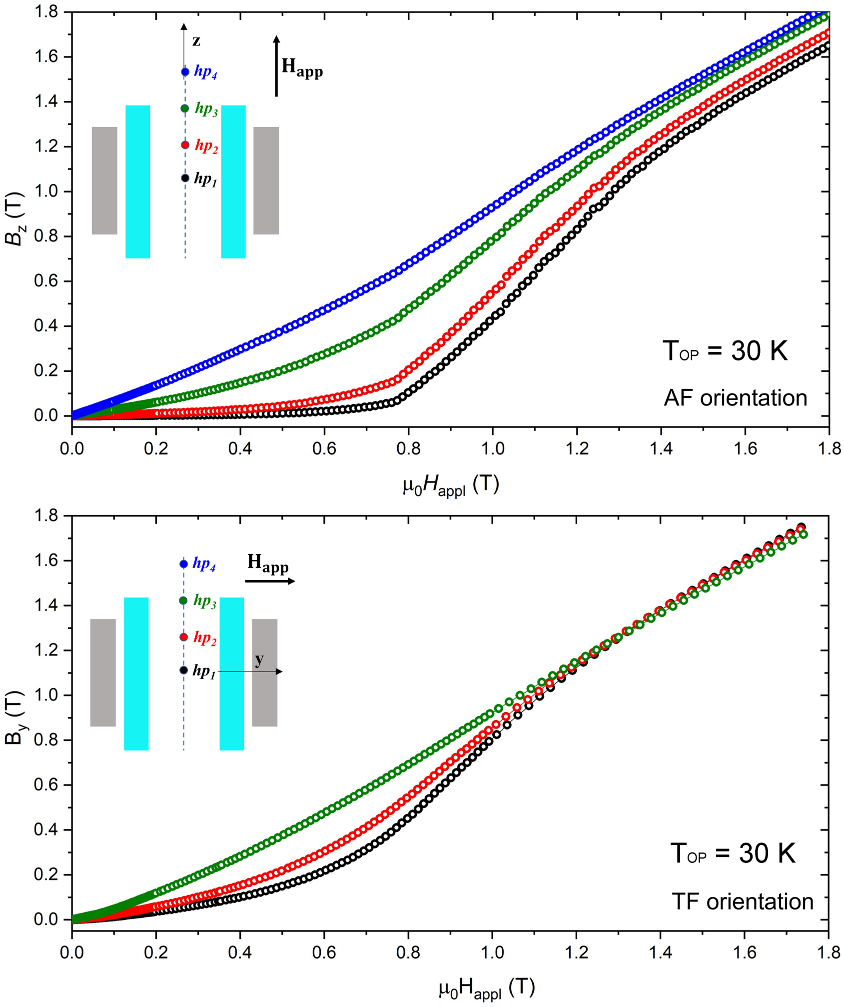

Fig. 4.9 Magnetic flux density measured at T_{OP}= 30 K as function of the applied field by the four Hall probes positioned along the hybrid shield axis.

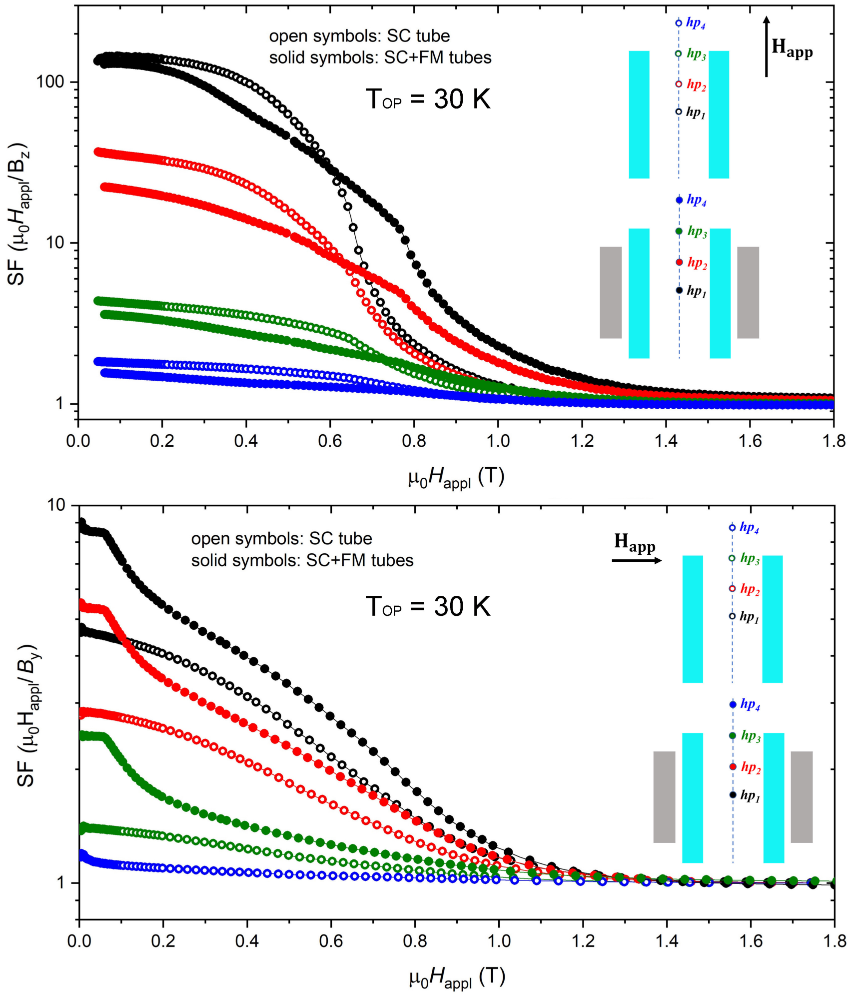

Fig. 4.10 Comparison of the SF curves measured at T$_{OP}$= 30 K as function of the applied field by the four Hall probes positioned along the SC (open symbols) and SC+FM (solid symbols) tube axis.

From this comparison, it emerges a dependence of the effect of the FM shield addition on the applied field orientation. In AF orientation at low fields ($\mu_0 H_{app} < 0.5$ T) the only SC solution is the most efficient, whereas the addition of the FM shield allows the persistence of a great-SF region at higher applied fields.

On the contrary, in the TF orientation the hybrid configuration ensures a better shielding performance in the whole range of applied fields, reaching a SF=9 in the shield centre (i.e. at position hp_1) up to $\mu_0 H_{app} \approx 0.1$, namely nearly doubling the SF obtained with the SC tube.

4.3 Summary

The experimental characterization allowed me to study the shielding performances of two different shield geometries (tube and cup) and to evaluate their shielding ability in a wide range of working temperatures. The results show that, thanks to the closed extremity, the cup-shaped shield is the most efficient layout even though flux-jump phenomena were observed up to quite high temperature. They also highlight how the magnetic mitigation capability of the SC shield strongly depends on the orientation of the applied magnetic field. Under this perspective, it was demonstrated that the addition of the FM shell can actually enhance the screening potential of the SC shields in TF orientation, where superconducting layouts were proved to be the less effective.

For these reasons, the collection of the experimental data lays the foundation for a more comprehensive and detailed analysis on the shielding properties of hybrid configurations also in dependence on the applied field orientation. In order to attain optimized layouts avoiding costly experimental trials and taking advantage of the computational analysis, new hybrid configurations are investigated by means of a numerical approach under differently tilted applied field. To this aim I employed the model based on the **A**-formulation, presented in Chapter 2, and, as will be shown in Chapter 5.2, the experimental data are fundamental for the validation of the model.

Chapter 5

Electromagnetic model

As mentioned in Chapter 2, in the last few years, numerical modelling was proved to be a powerful tool for the study of the electromagnetic behaviour of HTSs. In this work, I employed two mathematical formulations to describe the behaviour of the tube- and cup-shaped MgB_2 shields, namely the **A**- and **H**-based formulations, described in Section 2.5 and 2.6, respectively.
In the next section, the extension of the **A**-formulation to solve 3D shielding problems is presented. In Section 5.2 and Section 5.3 I describe the validation of this model through the comparison with the experimental results and the numerical output of a benchmark problem solved employing the well-established **H**-formulation. Finally, the numerical results obtained investigating new and more efficient hybrid layouts are presented in Section 5.4.

5.1 3D problem: A-based electromagnetic formulation

I implemented the numerical model based on the hyperbolic-tangent function (Section 2.5.1) by means of COMSOL Multiphysics®, which is suitable for computing magnetic fields and induced currents using Maxwell equations, expressed here in terms of the magnetic vector potential **A**. The model was applied both to the tube- and cup-shaped geometry and, initially, two orientations of the applied magnetic field were investigated. i.e. the axial field and the transverse field orientations.

The analysis was then enlarged to consider the intermediate tilt angle between the applied field direction and the axis of the shield. The superconducting behaviour of the two bulk shapes was described by means of the following non-linear **E–J** relationship, which, as evidenced in Section 2.5.1 for the 2D approach, provides a smooth approximation of the critical state model function [111, 97]:

$$\mathbf{J} = J_c \tanh\left(\frac{|\mathbf{E}|}{E_0}\right)\left(\frac{E_x}{|\mathbf{E}|}\mathbf{i} + \frac{E_y}{|\mathbf{E}|}\mathbf{j} + \frac{E_z}{|\mathbf{E}|}\mathbf{k}\right) \tag{5.1}$$

where $(E_x, E_y, E_z) = (-\frac{\partial A_x}{\partial t}, -\frac{\partial A_y}{\partial t}, -\frac{\partial A_z}{\partial t})$ is the local value of the electric field, and J_c is the local critical current density ($J_c \geq \sqrt{J_x^2 + J_y^2 + J_z^2}$). Here E_0 is a computation parameter that defines the sharpness of the transition function [3], which, in the case of power-law relation, is defined by the *n*-factor. Therefore, I would point out that the physical meaning of this parameter is not the same as the criterion conventionally assumed to identify the value of the critical current density from the I–V experimental curves [65]. Actually, the chosen value $E_0 = 10^{-4}$ Vm^{-1} gives a good compromise between the computation time performance and the accuracy introducing the shielding behaviour of the investigated superconducting object, also considering the chosen range of applied magnetic field and its growth rate [173]. However, other configurations could require additional verification and adjustment of E_0 value. Equation (5.1) ensures the collinearity between the current density and the electric field, expected in superconductors with isotropic properties, such as the polycrystalline $\mathrm{MgB_2}$ bulks that I experimentally characterized [64].

In order to properly simulate the SC shielding behaviour, the J_c dependence on the magnetic field needs to be taken into account. As introduced in Section 2.7, the J_c behaviour in $\mathrm{MgB_2}$ sample is well described by an exponential function. For these reasons, the experimental J_c(B) curves – obtained as explained in Section 3.4 - were fitted by the following exponential relation in the range of applied fields higher than the full penetration field:

$$J_c(B) = J_{c,0} exp\left[-\left(\frac{|\mathbf{B}|}{B_0}\right)^{\gamma}\right] \tag{5.2}$$

where $J_{c,0}$, B_0, and γ are constant parameters obtained separately for tube- and cup-shaped shields at each working temperature. The fit was only possible for applied fields that went beyond the entire penetration field. However, the effectiveness of the

fit parameters that emerged in defining $J_c(B)$ across the entire spectrum of applied fields under investigation was then presumed. (Figure 3.8) [137].
In all calculations, the source term for the applied magnetic field, $\mathbf{H}_{appl}$, was considered through the boundary conditions: at a large distance from the shield(s), $\mathbf{B}$ was set equal to $\mu_0\mathbf{H}_{appl}$. The applied field was always assumed uniform and increasing monotonically.

5.2 A-formulation approach validation: comparison with experimental data

The model based on the **A**-formulation was implemented through the Magnetic Field (*mf*) interface of COMSOL Multiphysics® as reported in the Section 5.1. To calculate the magnetic field penetration in both the superconducting tube and cup, I assumed the $J_C(B)$ dependence reported in Equation 5.2, where the parameters $J_{c,0}$, B_0 and γ have the values summarized in Table 5.1.

	$J_{c,0}$ (A/m^2)	B_0 (T)	γ
Tube	3.01×10^8	0.83	2.52
Cup	5.02×10^8	0.98	3.78

Table 5.1 Fitting parameters obtained by fitting the experimental critical current densities (see Section 3.4) by Equation 5.2.

The ferromagnetic shield was modeled introducing the B-H curve reported in Chapter 3, Section 3.5.

Figure 5.1 and 5.2 show the comparison between the experimental data and the computational outputs for the tube-shaped shields, both superconducting and hybrid, and for the two field orientations, AF and TF. The magnetic flux density was calculated in the same positions along the shields axis in which the magnetic flux density was measured during the experimental characterization (see Figure 3.6(b)). In both cases, the model allowed me to replicate the experimental data remarkably well.

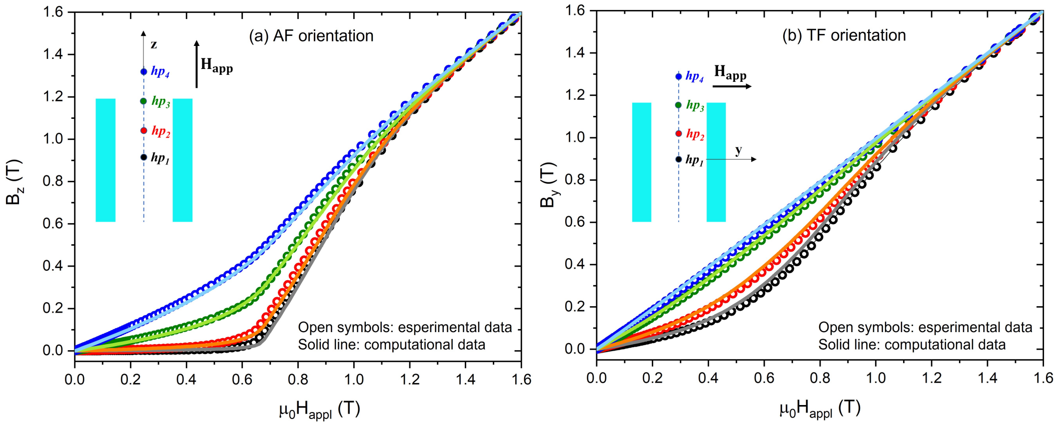

Fig. 5.1 Comparison between the magnetic flux density measured along the SC tube axis by the Hall probes at T_{OP} = 30 K (symbols) and the corresponding values computed by numerical simulations (lines), both in AF (a) and TF (b) orientations.

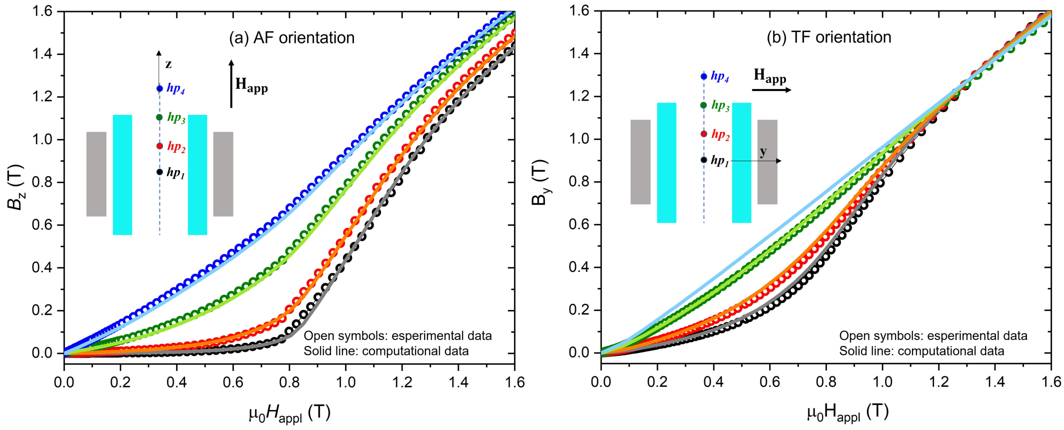

Fig. 5.2 Comparison between the magnetic flux density measured along the SC+FM tube axis by the Hall probes at T_{OP} = 30 K (symbols) and the corresponding values computed by numerical simulations (lines), both in AF (a) and TF (b) orientations. Note that the hp_4 experimental shielding curve of the SC+FM shield in TF orientation is lacking, since there were some wiring problems with the corresponding Hall probe.

The model was applied also to the superconducting cup-shaped shield and, also in this case, the magnetic flux density was calculated in the same positions along the shields axis in which the magnetic flux density was measured during the experimental characterization (see Figure 3.6(a)). The comparison between experimental and calculated magnetic flux density is reported in Figure 5.3, showing a valuable correspondence here as well. However, in the AF orientation the calculation cannot reproduce the occurrence of the flux jump at $\mu_0 H_{appl}$ = 1.0 T. This outcome was expected considering that the model predicts a homogeneous field penetration in the sample, pointing out that an extension of the model is needed in order to properly described the SC behaviour taking into account the thermo-magnetic instabilities. Moreover, some differences arise for the TF orientation when the magnetic flux starts to enter the cup through the closed extremity. They could be cause by some roughness of the inner surface of the cup base, which cannot be considered in the calculation unless the simulation time increase significantly.

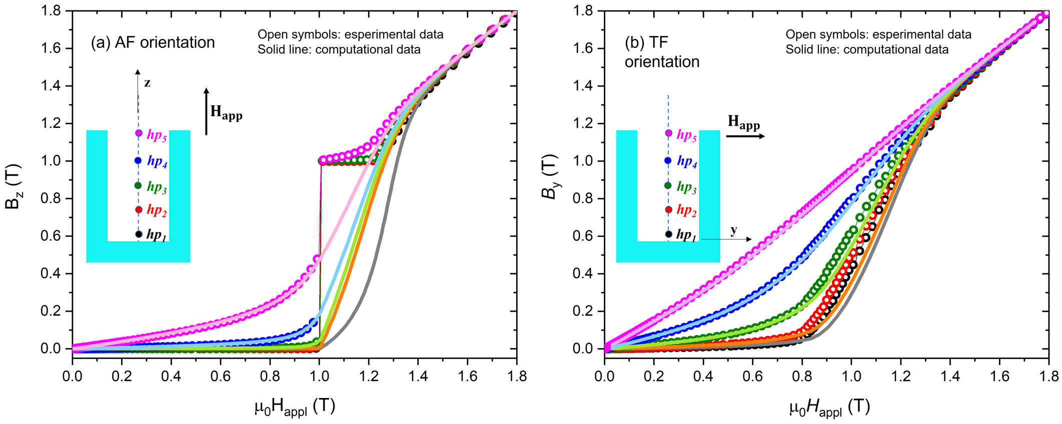

Fig. 5.3 Comparison between the magnetic flux density measured along the cup axis by the Hall probes at T_{OP} = 30 K (symbols) and the corresponding values computed by numerical simulations (lines), both in AF (a) and TF (b) orientations.

All these comparisons demonstrate that the model is able to reproduce the experimental data, and it is suitable to predict and investigate different geometries, both SC and SC+FM, for the two orientations of the applied field.

5.3 A-formulation approach validation: comparison with the H-formulation in the solution of a benchmark problem

The second validation was carried out by comparing the results obtained with the **A**-formulation with those collected through the **H**-formulation, investigating the shielding abilities of a tube-shaped superconducting shield, whose dimension corresponds to the SC sample experimentally characterized (Figure 3.2). The study focused on this shape since it is very advantageous from a computational time point of view and allows addressing the peculiarity of a short axisymmetric structure.

For what concerned the **A**-formulation, I used the same numerical procedure described in Section 5.1. Instead, the **H**-formulation was implemented by means of the PDE module of COMSOL Multiphysics®, in which the magnetic permeability μ_r was set to 1 in the whole space and the resistivity to 10^8 Ωm in the air domain. The SC was modeled by Equation 2.34, in which n was set equal to 100 according to [160].

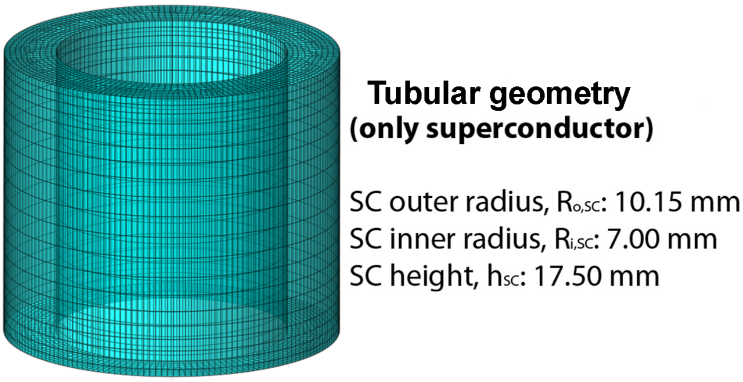

Fig. 5.4 Schematic view of the shielding layout investigated with both the **A**- and **H**-formulations.

The study was firstly carried out by applying the external field in the AF an TF orientations, up to applied field values at which the superconductor is fully penetrated. Then, I focused on the range $0 < \mu_0 H_{app} < 0.5$ T where the shielding effect is more significant, calculating the magnetic flux density distribution inside the shield for applied field tilted 7.5°, 15°, 30°, 45°, and 60° from the shield axis. This allows me to validate the use of the **A**-formulation based model regardless of the applied field direction. In Figure 5.5, the magnitude of the magnetic flux density calculated in the tube axis centre O (corresponding to Hall probe position hp_1) are shown.

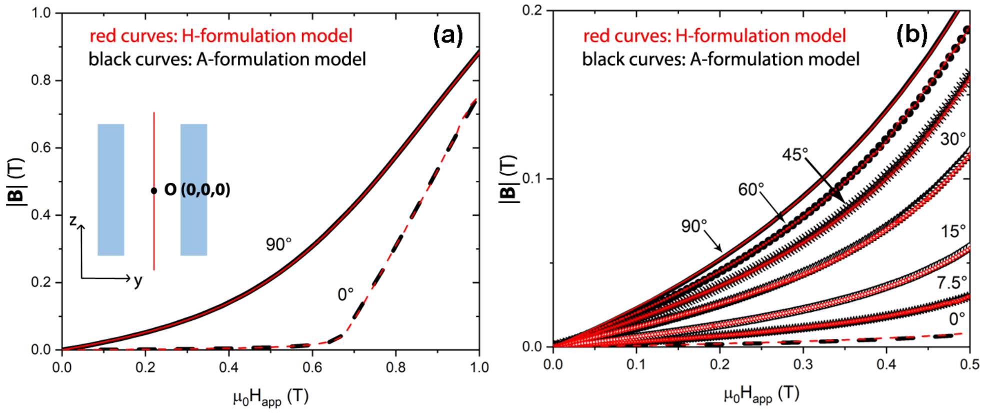

Fig. 5.5 Comparison between the magnetic flux density values calculated in the tube centre O (whose coordinates were set to (0,0,0)) using the **H**-formulation (red curves) and the **A**-formulation (black curves). Calculations were carried out in the axial and transverse field orientations (a) and for different angles of the applied field (b).

As can be seen, the curves obtained by means of the two different formulations display the same trend in the whole investigated magnitude range and for all the tilt angles of the applied field.

In order to verify the validity of the model in the entire screened region, result achieved at points out of axis of the tube were also compared. By way of example, Figure 5.6 shows the magnitude values of the magnetic flux density found at position O’ placed 4 mm away from the tube centre along the radial direction and 1 mm away along the axial direction. Also in this case, the comparison between the results obtained using the two formulations gives an excellent agreement for both the AF and TF orientations and the intermediate tilt angles of the applied magnetic field.

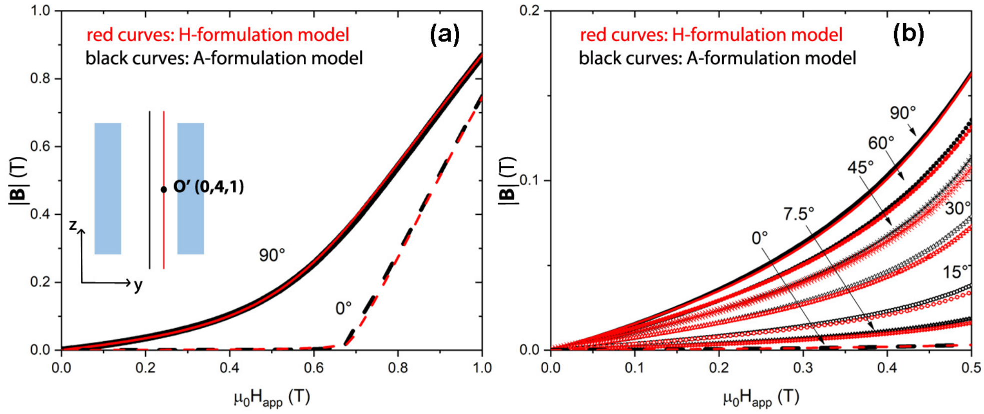

Fig. 5.6 Comparison between the magnetic flux density values calculated at point O' (whose coordinates related to point O are (0, 4, 1), i.e., 4 mm away from the tube centre along the radial direction and 1 mm away along the axial one), using the **H**-formulation (red curves) and the **A**-formulation (black curves). Calculations were carried out in the axial and transverse field orientations (a) and for different angles of the applied field (a).

Relying on this comparison, some further considerations about the **A**- and **H**-formulation based models can also been done. Despite both the numerical approaches lead to the same results, the choice of a computational approach must also take into account the computational effort required to solve the problem. Table 5.2 reports the computational time required by each formulation and the respective number of mesh elements [174]. As can be seen, for almost the same number of mesh elements, the **A**-formulation drastically reduces the computational time.

Model	number of elements	Computation Time
H-formulation	42185	≈120 h
A-formulation	42770	≈24 h

Table 5.2 Comparison of the number of mesh elements and computation time of the models based on the **H**- and **A**-formulations.

Therefore, the solution of this benchmark problem not only proves the viability of the **A**-based approach for the solution of shielding problems, confirming the positive outcome of the validation procedure in Section 5.2, but it also shows that this approach is the most performing in terms of computational time

5.4 Study of new hybrid configurations

After the twofold validation of the **A**-formulation approach in modeling the magnetic field mitigation properties of both SC and SC+FM shields, I applied this numerical procedure to predict the screening properties of new hybrid layouts. The effect of the FM layer was studied as a function of the height of the FM layer with respect to the SC shields.

First, I compared the behaviour of some configurations both in the AF and TF orientations. Next, after identifying the most efficient tube- and cup-shaped hybrid solutions, I focused on the effects of the orientations of the applied magnetic field, considering magnetic field directions between 0°and 90° with respect to the shield symmetry axis. The reasons of this study are twofold. On the one hand, the computational and experimental analysis performed on the shields – both SC and SC+FM – evidences a dependence of the shielding abilities on the orientation of the applied field. Moreover, the study carried out for the benchmark problem, highlights that the shielding ability of a short SC tube is strongly reduced already at small tilting angles of the applied field with respect to the shield axis.

In all the investigated configurations, the SC tube and cup dimensions were assumed to be the same as those of the samples characterized experimentally as well as the parameters $J_{c,0}$, B_0 and γ are the same employed in the first numerical study (see Table 5.1). Similarly, the FM shield was supposed to be made of the same material as that experimentally characterized and therefore the same B-H curve was used to model it.

5.4.1 Tube–shaped shields

The effect of the FM shell addiction: comparative analysis of different layouts in the AF and TF orientations

Two different configurations were compared, henceforth labelled hybrid tube configuration HTC2 and hybrid tube configuration HTC3, shown in Figure 5.7. The layout HTC2 is the same that was characterized experimentally (Figure 3.9). For the sake of clarity, its sketch is again reported in Figure 5.7. Moreover, it is worth mentioning that I did not consider combinations of SC and FM tubes with the same height. This is due to the fact that previous investigations [168, 169] highlighted that the occurrence of a shift in the edge of the two shields is a key factor to optimize the performances of the device.

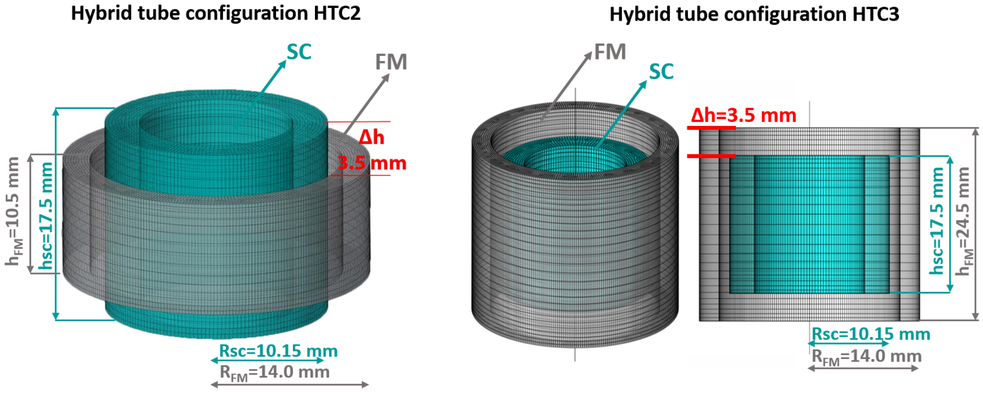
Hybrid tube configuration HTC2 **Hybrid tube configuration HTC3**

Fig. 5.7 Schematic view of the tubular hybrid layouts consisting in SC+FM superimposed tubes with the SC tube protruding above the FM one (HTC2) and in SC+FM superimposed tubes with the FM tube protruding above the SC one (HTC3). The shield sizes are reported in the picture; Δh represents the height difference between the tubes edges.

Figure 5.8 shows the shielding factors of the single SC tube and of the configurations HTC2 and HTC3 for the AF orientation. The positions match those chosen for comparison with the experimental results. Therefore, the plotted curves were calculated at the position: $hp_1 = 0$ mm (SC shields centre), $hp_2 = 4.4$ mm and $hp_3 = 8.8$ mm (SC shield edge coordinate), left unchanged both in AF and TF orientation; $hp_4 = 13.1$ mm and $hp_4 = 12$ mm in AF and TF orientation respectively.

Since the magnetic flux lines are attracted by the FM tube, the magnitude of the magnetic flux density at the shield openings is greater than in the case of the single SC tube. Consequently, in both case, the superimposition of the FM tube induces a slight SF worsening at low applied field. Instead, by raising the applied field, the flux penetration from the lateral wall becomes significant, and the screening effect by the FM tube makes the SF of the hybrid configurations overcome that of the single SC tube. Configuration HTC3 is the most efficient: using this configuration, the upper limit of the region where high-SFs can be achieved is shifted from about 0.6 T (with the SC alone) to about 0.8 T.

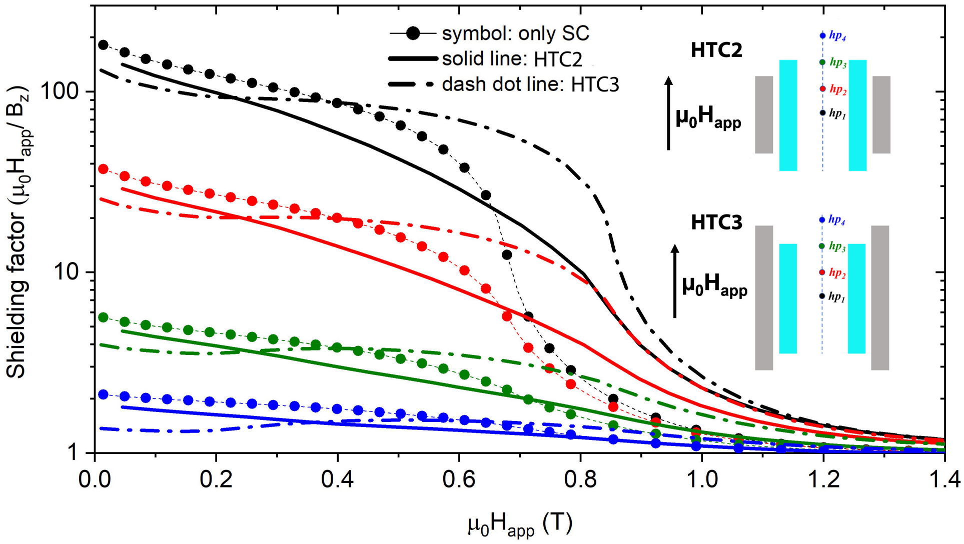

Fig. 5.8 Comparison between the SFs calculated for the single SC tube (symbols) and for the configurations HTC2 (solid lines) and HTC3 (dash dot lines) in the AF orientation.

Conversely, as shown in Figure 5.9, in TF orientation, the configuration HTC3 shows the best shielding performances in the whole investigated range of fields and not only for $\mu_0 H_{app} > 0.5$ T. Comparing the HTC3 shielding ability with that of the only SC shield at low applied field, it can be seen that hybrid configuration provides a $SF = 40$ against SF values lower than 10 obtained with the SC shield alone. This improvement is again caused by the FM material property to accumulate the magnetic flux lines inside. In this orientation, this effect provides a reduction of the magnetic flux density at the superconducting shield openings, which, due to the small aspect ratio of the tubes, affects the SF throughout the shield. Noticeably, the longer the FM tube is, the greater the improvement is, as it appears from Figure 5.10 where the SF colour maps are shown for HTC2 and HTC3.

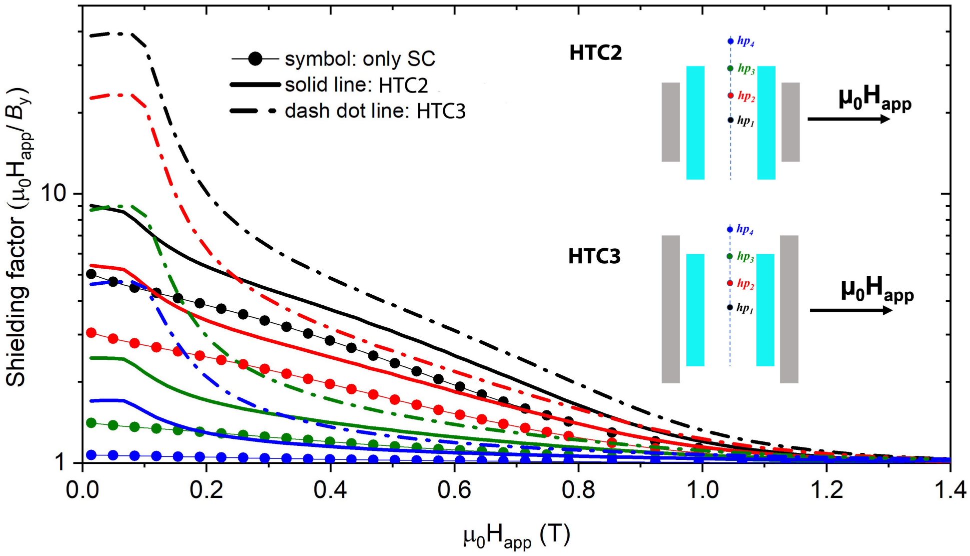

Fig. 5.9 Comparison between the SFs of the single SC tube (symbols) and for the configurations HTC2 (solid lines) and HTC3 (dash dot lines) in the TF mode.

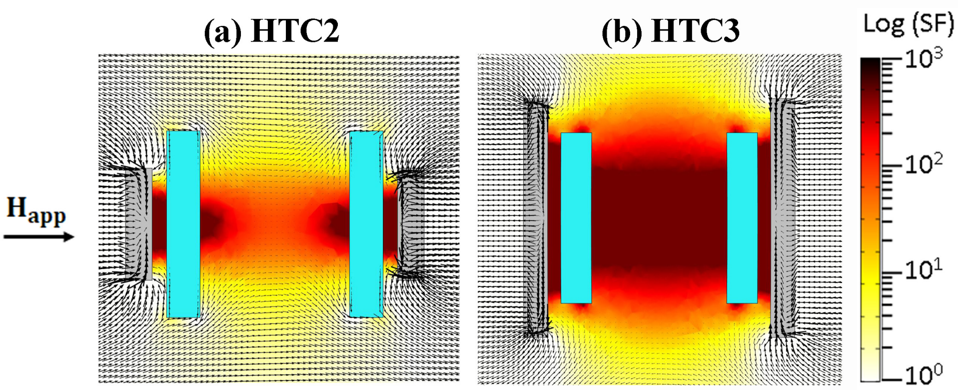

Fig. 5.10 Comparison of the SF (colour) maps and the magnetic flux line distributions computed for shields HTC2 (a) and HTC3 (b) after the external field, applied along the y-direction, was ramped up to $\mu_0 H_{appl}$ = 0.1 T. Data are related to the central cross-section parallel to the applied field characterization. To better represent the full range of the SF values, a logarithmic colour scale is used.

Usefulness of the FM shell superimposition at different tilt angle of the applied field

The former study evidenced that the effect of the FM layer addition at low fields strongly relies on the relative height of the FM and SC components and on the field orientation. For these reasons, since the hybrid configuration HTC3 turns out to be the better performing, I focused on the comparison between the HTC3 and the only SC tube shielding performances. With the aim of investigating the influence of the FM shield superimposition under realistic operating conditions, the shielding properties for applied magnetic field with intermediate inclinations with respect to the shield axis, namely 7.5°, 15°, 30°, 45°, and 60°, were investigated. Furthermore, I focused on the low applied field range ($0 \text{ T} < \mu_0 H_{app} < 0.5 \text{ T}$), where the use of the hybrid configuration could not guarantee an increase in the shielding abilities. This comparison confirms the drastic dependence of the shielding effect on the applied magnetic field orientation. Figure 5.11(a)–(g) displays the SFs of the configuration HTC3 (dash dot line), SF_{hybrid}, and that of SC tube (dot symbols), $SF_{supercond}$, at the same positions hp_1, hp_2, hp_3, and hp_4. Focusing in the range $0 \text{ T} < \mu_0 H_{app} < 0.2$ T for the position hp_1, one can see that a tilted field of 7.5° (Figure 5.11(b)) is enough to make the hybrid arrangement 4 times more efficient than the only SC tube. To better quantify this improvement, the ratio of the HTC3 SFs to the SC tube SFs ($SF_{hybrid}/SF_{supercond}$) are shown in Figure 5.12 as a function of the tilt angles of the applied magnetic field. Focusing on position hp_1, as the applied field inclination increases, the ratio rises steadily until it reaches a maximum value of 8 for a 45° tilt angle. Even though at the other positions along the shield axis the crossover between a worsening to an enhancing effect of the FM shell addition is shifted to greater tilt angles of the applied field, the trend of the SF ratios as a function of the inclination angle is confirmed.

These findings enable me to draw the conclusion that the superimposition of a ferromagnetic shield can successfully mitigate the abrupt drop of shielding factor that occurs in a superconducting short tube, even for a small inclination of the applied field.

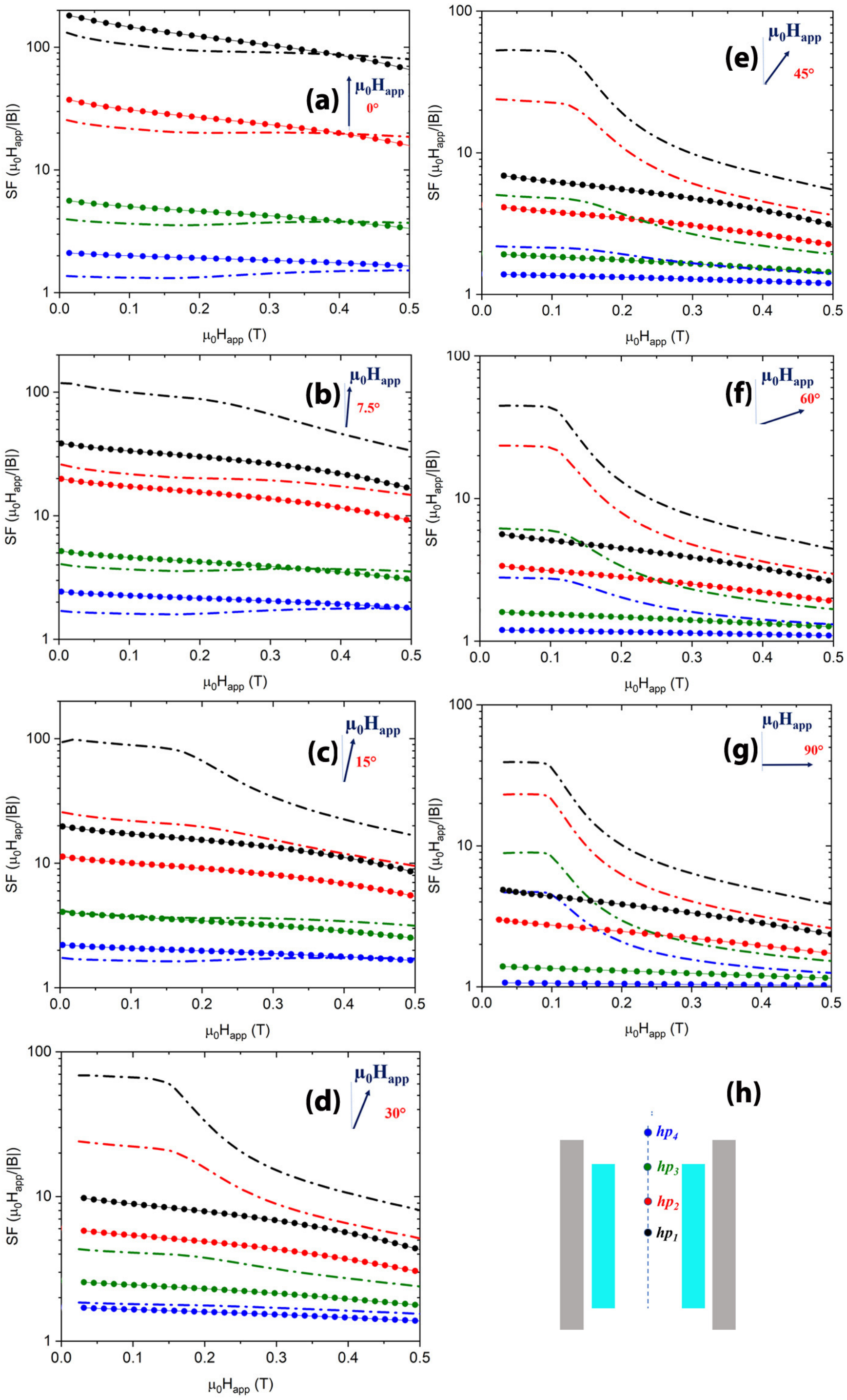

Fig. 5.11 Comparison between the SFs of the single SC tube (dot symbols) and the configuration HTC3 (dash dot lines). Each frame (a)–(g) corresponds to a different tilt angle of the applied magnetic field.

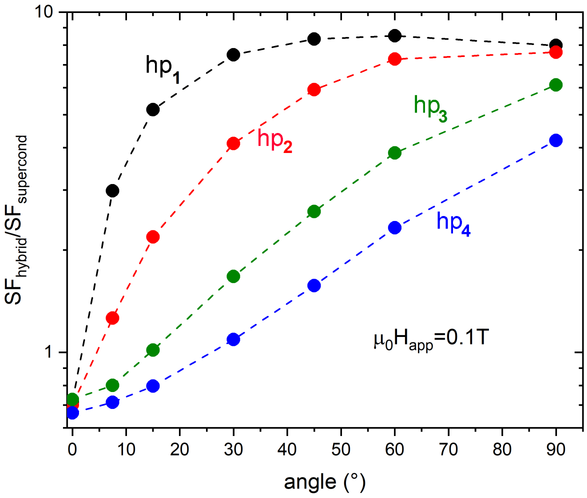

Fig. 5.12 Dependence of the ratio between the SFs of the configuration HTC3 and those of the single SC tube, $SF_{hybrid}/SF_{supercond}$, on the tilt angle of the applied magnetic field having magnitude 0.1 T. The data refer to positions hp_1 (black dots), hp_2 (red dots), hp_3 (green dots), and hp_4 (blue dots) reported in Figure 5.11(h).

5.4.2 Cup–Shaped shields

The effect of the FM shell addiction: comparative analysis of different layouts in the AF and TF orientations

Following the same procedure, I looked into how the superimposition of a coaxial FM cup can modify the SF of the SC cup. As for the tube, at first the research was conducted in relation to the FM cup height, as shown in Figure 5.13. Defining Δh as the difference between the FM internal depth d_{FM} and the SC external height h_{SC}, three different values of Δh are considered, namely Δh=0 mm for the Hybrid cup configuration 1 (HCC1), Δh=-3.5 mm for the Hybrid cup configuration 2 (HCC2) and Δh=3.5 mm for the Hybrid cup configuration 3 (HCC3). The study was carried out in both AF and TF orientations. I assumed that the size and the physical properties of the SC cup are the same as those of the cup experimentally characterized (see Figure 3.3) while the FM cup was considered to be made out of ARMCO iron with the same B–H constitutive law as the FM tube experimentally characterised. The positions at which the magnetic flux density is calculated match those chosen for comparison with the experimental results. Therefore, defining $hp = 0$ to be the coordinate of the closed extremity of the SC cup, the plotted curves were calculated at the position: hp_1 = 1.0 mm, hp_2 = 5.0 mm, hp_3 = 9.2 mm (SC shield centre), hp_4 = 13.7 mm, and hp_5 = 18.3 mm (SC shield open extremity).

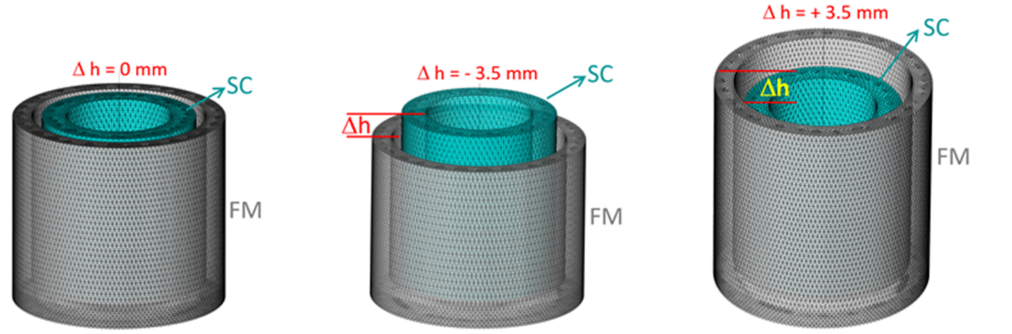

Hybrid cup configuration 1 (HCC1)

SC outer diameter, $D_{o,SC}$: 20.3 mm
SC inner diameter, $D_{i,SC}$: 14.0 mm
SC external height, h_{SC}: 22.5 mm
SC internal depth, d_{SC}: 18.3 mm

FM outer diameter, $D_{o,FM}$: 28.0 mm
FM outer diameter, $D_{i,FM}$: 23.0 mm
FM external height, h_{FM} : 25.0 mm
FM internal depth, d_{FM}: 22.5 mm

Hybrid cup configuration 2 (HCC2)

SC outer diameter, $D_{o,SC}$: 20.3 mm
SC inner diameter, $D_{i,SC}$: 14.0 mm
SC external height, h_{SC}: 22.5 mm
SC internal depth, d_{SC}: 18.3 mm

FM outer diameter, $D_{o,FM}$: 28.0 mm
FM outer diameter, $D_{i,FM}$: 23.0 mm
FM external height, h_{FM} : 21.5 mm
FM internal depth, d_{FM}: 19.0 mm

Hybrid cup configuration 3 (HCC3)

SC outer diameter, $D_{o,SC}$: 20.3 mm
SC inner diameter, $D_{i,SC}$: 14.0 mm
SC external height, h_{SC}: 22.5 mm
SC internal depth, d_{SC}: 18.3 mm

FM outer diameter, $D_{o,FM}$: 28.0 mm
FM outer diameter, $D_{i,FM}$: 23.0 mm
FM external height, h_{FM} : 28.5 mm
FM internal depth, d_{FM}: 26.0 mm

Fig. 5.13 Schematic view of the cup-shaped hybrid layouts whose shielding properties were calculated. From left to right: SC+FM superimposed cups with the open extremity at the same height (HCC1; Δh = 0 mm), SC+FM superimposed cups with the SC cup protruding above the FM one (HCC2; Δh = -3.5 mm) and SC+FM superimposed cups with the FM cup protruding above the SC one (HCC3; Δh = +3.5 mm).

As for the hybrid tube layouts, in the AF orientation the addition of the FM cup induces a worsening in the shielding ability at low applied fields, as can be seen in Figure 5.14. This can be attributed to the fact that the magnetic flux entrance from the cup opening is predominant in such short shields. Therefore, the FM component, modifying the curvature of the magnetic flux lines, induces a higher magnetic flux density at the shield opening, which has an impact on the SF all throughout the shield. However, when the FM cup edge protrudes beyond the SC edge, specifically with the HCC3 layout, this SF worsening was partly mitigated. Conversely, the addition of the FM shell reduces the magnetic flux penetration from the lateral wall of the shield, thus increasing the range of applied fields for which elevated SFs can be obtained. The most effective configuration, HCC3, ensures a SF greater than 100 in the entire inner half of the SC cup up to $\mu_0 H_{appl}$ = 1.1 T.

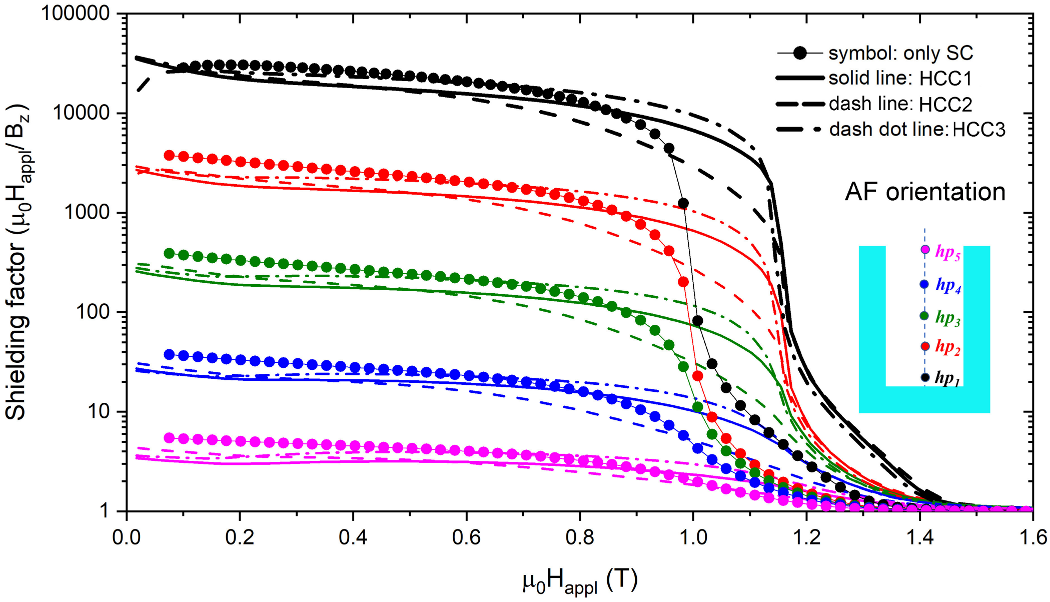

Fig. 5.14 Comparison between the SFs of the single SC cup (symbols) and of the hybrid configurations HCC1 (solid lines), HCC2 (dash lines) and HCC3 (dash dot lines) in the AF mode.

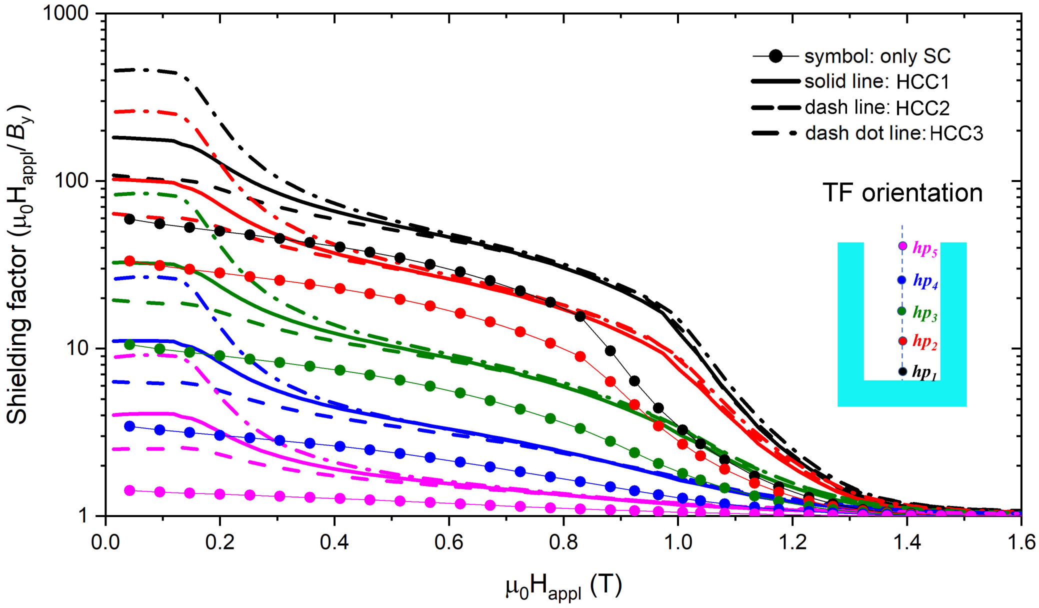

Fig. 5.15 Comparison between the SFs of the single SC cup (symbols) and of the hybrid configurations HCC1 (solid lines), HCC2 (dash lines) and HCC3 (dash dot lines) in the TF mode.

Figure 5.15 shows the SFs computed for the same shielding arrangements in the TF orientation as a function of the applied field. Contrary to what was seen in the AF orientation, the FM cup superimposition increases the SF values across the board for all the examined applied fields. The range of applied fields with the greatest SFs is that where in no zone of the FM shell the magnetic flux density exceed the saturation value. In this range, the shielding capacity of the entire structure is significantly influenced by the FM cup aspect ratio. Focusing on the most efficient configuration, namely the HCC3, the addition of the FM cup causes the SF at location $hp1$ to rise from 50 to 450 and leads to SFs greater than 100 in about half of the central volume of the shield. The other two hybrid configurations with lower aspect ratios of height to average diameter of the FM cup still yield notable improvements, even though they are not as high. Due to the different heights of the FM cups, there is a variation in the magnetic flux line organization near the open extremity of the hybrid shield (Figure 5.16). On the other hand, over $\mu_0 H_{appl}$ = 0.2 T, some FM shield zones (specifically, the outermost layer of the closing cap and the final section of the lateral wall close to the open edge) experience magnetic saturation, and the benefit of superimposing the FM shell begins to wane. However, even with partially saturated zones, the presence of the FM cup still reduces the magnetic field applied to the SC cup. Accordingly, the SFs of the hybrid shields are still greater than that of the SC cup. The SFs curves of the three hybrid configurations collapse at $\mu_0 H_{appl}$ = 0.6 T where the SFs stop being reliant on the FM cup height.

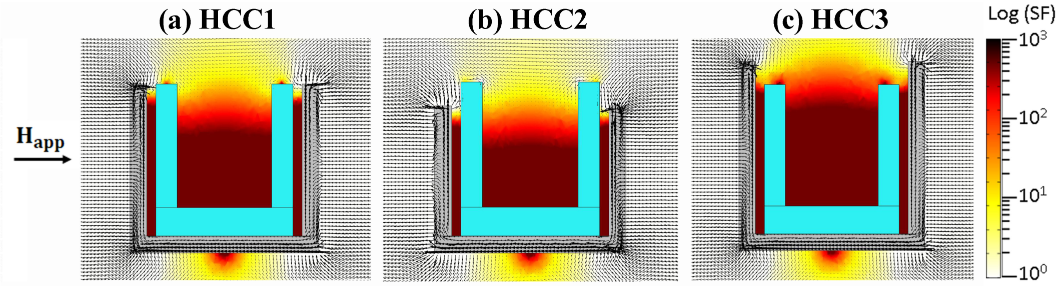

Fig. 5.16 Comparison of the SF (colour) maps and the magnetic flux line distributions computed for shields HCC1 (a), HCC2 (b) and HCC3 (c) after the external field, applied perpendicular to the shield axis, was ramped up to $\mu_0 H_{appl}$ = 0.1 T. Data are related to the central cross-sections parallel to the applied field direction. To better represent the full range of the SF values, a logarithmic colour scale is used.

Finally, still focusing on layout HCC3, I also investigate how the thickness of the FM wall can affect the SF of the hybrid configuration. The study pointed out that this parameter plays a minor role. Figure 5.17 compares the shielding factors calculated at $\mu_0 H_{appl}$ = 0.1 T along the axis of the SC cup, for the hybrid configurations HCC1, HCC2 and HCC3 and for two new configurations: HCC3_A and HCC3_B. The configurations HCC3, HCC3_A and HCC3_B differ from each other only in the lateral wall/base thickness, that is 2.5 mm for HCC3, 2.0 mm for HCC3_A and 3.0 mm for HCC3_B. Data refer to the transverse field orientation, where, at low fields, the addition of the FM shell is especially helpful. As can be seen, a 20% increase/reduction of the wall thickness of the FM cup provides an almost negligible change compared to the change induced by a 15% increase/reduction of its height. Of course, significant changes in the shielding factors values are expected for substantial reduction of both the SC and FM cup thickness, but in this case the mechanical stability of the whole structure should also be considered and this is beyond the aim of this work.

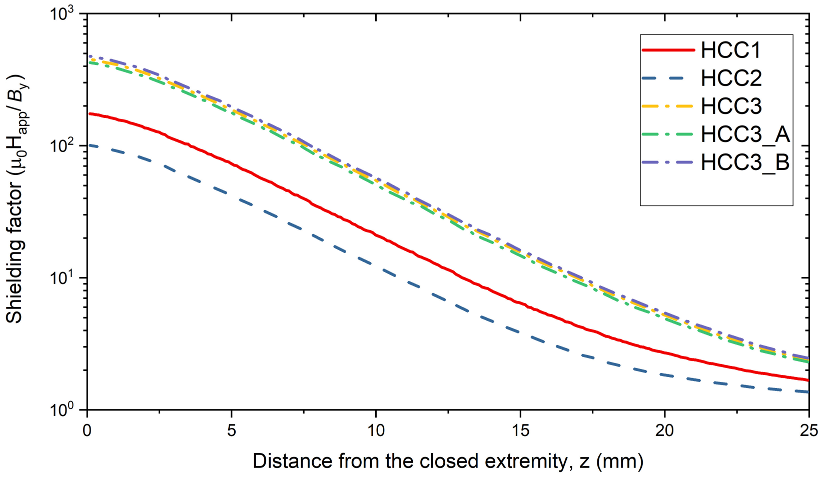

Fig. 5.17 Comparison among the shielding factors calculated for the arrangements EC3, HCC1, HCC2, HCC3, HCC3_A, HCC3_B as a function of the position along the cup axis. Calculations were carried out assuming the external field, $\mu_0 H_{appl}$ = 0.1 T, applied perpendicular to the shield axis. The zero position corresponds to the SC cup close extremity. The dimensions of the arrangements HCC1, HCC2, HCC3 are reported in Figure 5.13. The configurations HCC3, HCC3_A and HCC3_B differ from each other only in the lateral wall/base thickness that is 2.5 mm for HCC3, 2.0 mm for HCC3_A and 3.0 mm for HCC3_B (note that the lateral gap between the SC and the FM shields was always keep constant).

Usefulness of the FM shell superimposition at different tilt angle of the applied field

The previous research shows that the shielding ability of the SC cup is greatly improved by the superimposition of the FM. The hybrid cup arrangement HCC3 in particular proved to be the most effective, expanding the application field range where shielding factors of the order of 10^4 can be attained in the AF direction up to $\mu_0 H_{app} \approx 1.2$ T. Conversely, the shielding ability in the AF orientation is worsened by the FM addition at low applied fields, whereas it is improved in the TF orientation, where the SF rises from 50 to 450 at $\mu_0 H_{app} \approx 0.1$ T near the closed extremity. Thus, focusing on the HCC3 configuration, I expanded the study of the shielding properties to applied magnetic fields with inclinations of 7.5°, 15°, 30°, 45°, and 60° with respect to the shield axis, in order to better comprehend the utility of the FM shell superimposition. The shielding factor values for the hybrid configuration HCC3 and the SC cup are plotted in Figure 5.18(a)–(g) at the five distinct *hp* positions along the shield axis for the above-mentioned applied tilted fields.

The addition of the FM cup results in a notable gain even for very small tilt angles, particularly when focusing on the inner positions hp_1 and hp_2, in the range $0\ \mathrm{T} < \mu_0 H_{app} < 0.2$ T. Indeed, the hybrid arrangement is ≈8 times more efficient than the single SC cup even in a field tilted by 7.5° with respect to the shield axis, as visible in Figure 5.19, where the ratio of the SFs of the configuration HCC3 to those of the single SC cup ($SF_{hybrid}/SF_{supercond}$) are plotted at $\mu_0 H_{app} = 0.1$ T.

The SF ratio for the lowest *hp* positions remains constant also raising the tilt angle of the applied field. On the other hand, the SF ratio values for the three outermost locations, hp_3, hp_4, and hp_5, are smaller at low applied field tilt angles and exhibit a rising tendency as the field inclination increases. Except for position hp_5, the ratio is always higher than one, showing that the FM shell addition has a beneficial impact even at low applied field tilt angles.

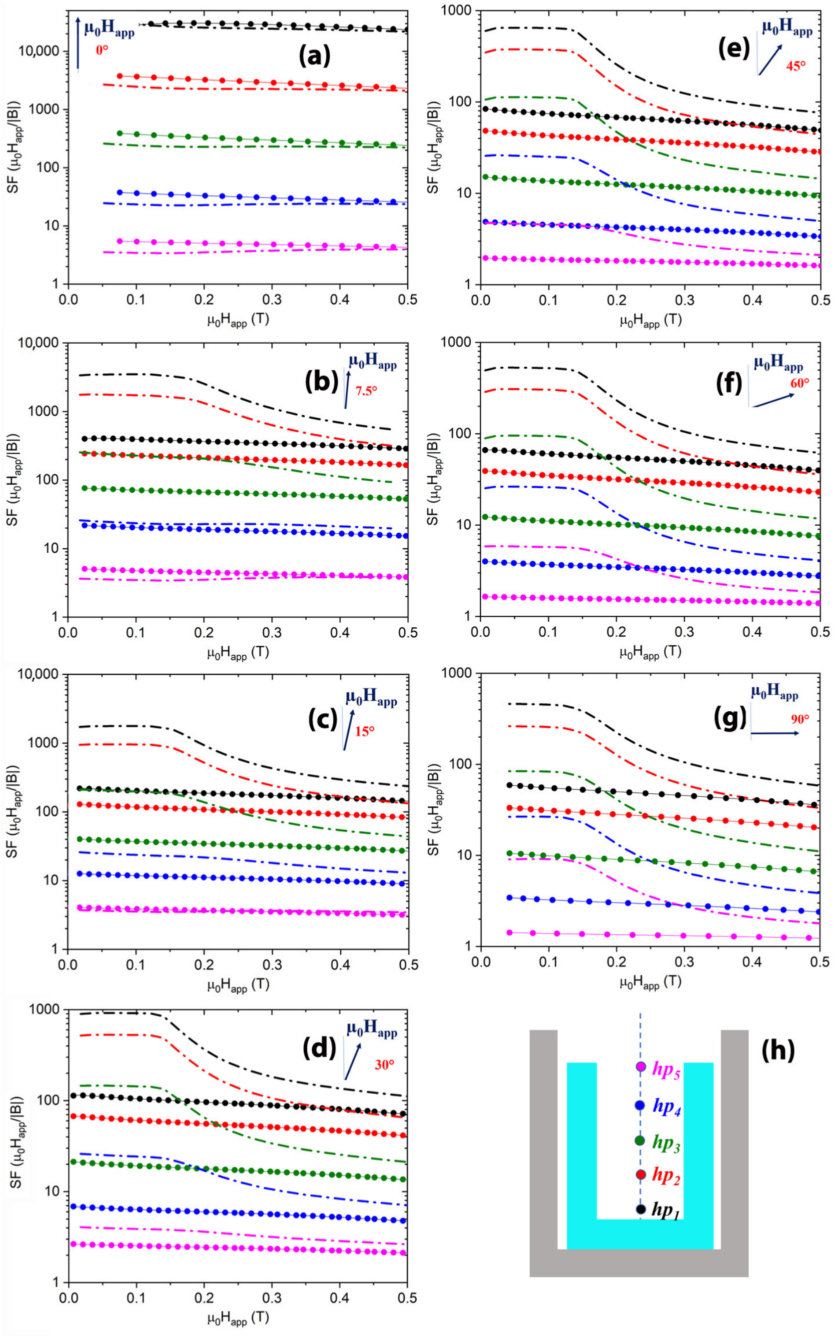

Fig. 5.18 Comparison between the SFs of the single SC cup (dot symbols) and the configuration HCC3 (dash dot lines). Each frame (a)-(g) corresponds to a different tilt angle of the applied magnetic field.

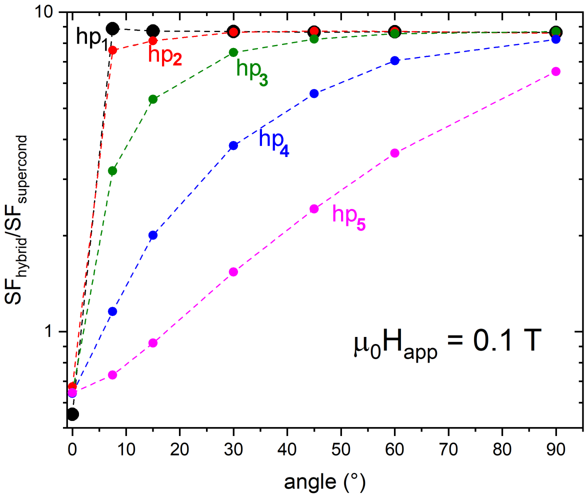

Fig. 5.19 Dependence of the ratio between the SFs of the configuration HCC3 and those of the single SC cup, $SF_{hybrid}/SF_{supercond}$, on the tilt angle of the applied magnetic field having magnitude 0.1 T. The data refer to the positions hp_1 (black dots), hp_2 (red dots), hp_3 (green dots), hp_4 (blue dots), and hp_5 (magenta dots) reported in Figure 5.18(h).

5.5 Summary

In this chapter, the effect of the addition of a FM shell on the SC shield has been addressed by a numerical approach. This numerical procedure was applied to predict the screening ability of new hybrid shield layouts consisting of superimposed coaxial SC and FM tube- and cup-shaped shields. The analysis showed that the addition of a FM shell could be a successful method to mitigate the steep reduction of the shielding capacity of short SC shields when the external field is rotated out of their symmetry axis. The positive effect of the FM shell superimposition is stronger if the open edge(s) of the FM shield protrudes (protrude) over the SC shield edge(s). By contrast, the FM shield superimposition induced a slight worsening at low applied field in the axial field orientation that, however, can be considered negligible.

Chapter 6

Electromagnetic-thermal model

The experimental characterization of the SC cup-shaped shield evidenced the occurrence of the flux jump instabilities when an AF is applied and for all the considered operational temperatures below 35 K. As shown in Chapter 5, the first version of the model based on the **A**-formulation cannot reproduce the effect of these thermomagnetic instabilities. For this reason, an upgrade of the model was needed. To this aim, the electromagnetic equations were coupled with the heat diffusion equation. This coupled model was then validated by comparing the computational outputs to the experimental results obtained at three different operational temperatures, namely 20, 25 and 30 K. The theoretical basis of the model and the boundary condition used to numerically define the experimental conditions are presented in Section 6.1, while the computational results and their comparison with the experimental data are discussed in Section 6.2. Finally, in Section 6.3 some possible improvements of the experimental setup for the mitigation of the flux jump occurrence are investigated.

6.1 Electromagnetic-thermal model

Due to high concentration of the MgB_2 in the starting powder [64], thermo-magnetic instabilities can be experimentally observed in the cup-shaped shield, where, in the AF orientation, flux jumps occur up to 32.5K introducing an abruptly worsening of the shielding performances. However, the calculation with the model described in the Sections 5.1 cannot reproduce these flux jump occurrence, since it predicts a homogeneous magnetic field penetration. For this reason, a coupled approach combining the magnetic and thermal behaviour of the superconductor is needed to accurately describe the superconducting behaviour. Since in the investigated temperature range this phenomenon appears only in the AF orientation, in order to reduce and simplify the computational effort of this coupled formulation, I chose a 2D approach in order to take advantage of the axial-symmetry of the shield.

To reproduce the effects of the thermo-magnetic instabilities on the shielding properties of the MgB_2 cup-shaped bulk, I combined the magnetic vector potential formulation discussed in Sections 5.1 with the heat balance Equation 2.40 [130, 132]. The modeling was implemented by the finite element software COMSOL 6.0 Multiphysics® [2] through the Magnetic Field (*mf*) interface coupled with the Heat Transfer (*ht*) module. To validate this numerical approach by comparing experimental and computed data, I assumed that the sample here numerically investigated has the same size and physical properties as the superconducting cup-shaped shield experimentally characterized (Figure 3.3, Section 3.2). For easy viewing, a sketch of the sample is again drawn in Figure 6.1(a). The sample was assumed subjected to the external magnetic field $\mathbf{H}_{app}(t)$ applied parallel to the cup axis after the zero-field cooling, established a cylindrical coordinate system (r, ϕ, z) with the origin placed on the base centre of the sample and assumed the external field applied parallel to the shield axis.

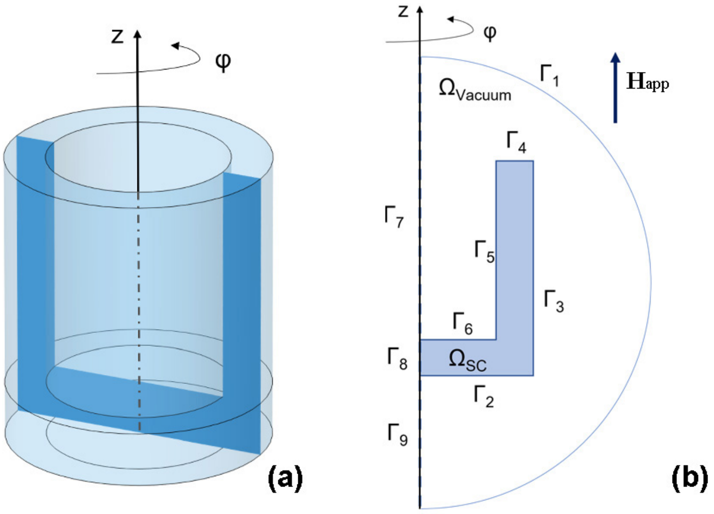

Fig. 6.1 Schematic view of the cup-shaped MgB_2 bulk. The dimensions of the cup correspond to those of the cup-shaped shield characterize experimentally (see Figure 3.3): outer diameter: 20.3 mm, inner diameter: 14.0 mm, external height: 22.5 mm, internal depth: 18.3 mm.

6.1.1 Electromagnetic equations

As said before, the electromagnetic behaviour of the superconducting and the surrounding domains is described by the Maxwell equations, which are formulated using the magnetic vector potential **A**:

$$\mathbf{E} = -\frac{\partial \mathbf{A}}{\partial t} \tag{6.1}$$

$$\mathbf{B} = \nabla \times \mathbf{A} \tag{6.2}$$

However, as a consequence of the chosen axisymmetric approach, the vector potential has only one component, A_ϕ, and equations (6.1) and (6.2) become:

$$E_\phi = -\frac{\partial A_\phi}{\partial t} \tag{6.3}$$

$$\mathbf{B} = -\frac{\partial A_\phi}{\partial z}\boldsymbol{\rho} + \frac{1}{r}\left[\frac{\partial}{\partial r}(rA_\phi)\right]\mathbf{k} \tag{6.4}$$

being $\boldsymbol{\rho}$ and **k** the unit vectors along the r- and z-directions, respectively.

The relationship between the local electric field and current density ($E - J$) in the superconducting domain was again modelled by using the hyperbolic tangent function. Accordingly, the electrical conductivity of the superconductor σ_{SC} introduced in the Ampere Law module in Comsol takes the form:

$$\sigma_{SC} = \frac{1}{|E_\phi|} J_c(B,T) \cdot tanh\left(\frac{|E_\phi|}{E_0}\right) \tag{6.5}$$

where, E_0 is the computational parameter already introduced in Section 2.5.1.

Furthermore, to ensure an appropriate value of the electrical conductivity during the transition between the superconducting- and normal-state, a term representing the normal state conductivity σ_{norm} (see Table 6.1) was added in parallel to that of the superconductor, as proposed in [130]. The electrical conductivity, σ was then modified as follows:

$$\sigma = \frac{1}{|E_\phi|} J_c(B,T) \cdot tanh\left(\frac{|E_\phi|}{E_0}\right) + \sigma_{norm} \tag{6.6}$$

In the equation above, the effect of the temperature on the superconducting behaviour was introduced by defining the critical current density, $J_c(B,T)$, as dependent on the local magnetic field and temperature through the following general form [160, 130]:

$$J_c(B,T) = J_{c0}(T) \cdot exp\left[-\left(\frac{B}{B_0(T)}\right)^{\gamma}\right] \tag{6.7}$$

where

$$J_{c0}(T) = \alpha[1-(T/T_c)^{\tilde{\alpha}}]^a \tag{6.8}$$

$$B_0(T) = \beta[1-(T/T_c)^{\tilde{\beta}}]^b \tag{6.9}$$

being α, β, $\tilde{\alpha}$, $\tilde{\beta}$, a and b fit coefficients calculated by fitting the experimental $J_{c0}(T)$ and $B_0(T)$ curves, in turn achieved by fitting the experimental $J_c - B$ curves measured at different temperatures as explained in Section 3.4 and reported in [64]. The values of these coefficients are summarized in Table 6.1.

Although γ is usually assumed to be constant, its value rises with the temperature [175, 137]. Therefore, to consider it appropriately, the following parabolic behaviour of γ as a function of T was assumed:

$$\gamma(T) = l \cdot T + g \cdot T^2 \tag{6.10}$$

where l and g are still fitting parameters, listed in Table 6.1.

6.1.2 Boundary conditions and modeling constraints

To calculate the effect of the thermo-magnetic instabilities on the local magnetic field inside the shield, the electromagnetic equations (Section 6.1.1) were solved for both the SC (Ω_{SC}) and the external domain (henceforth named vacuum domain, Ω_{vacuum}) (Figure 6.1 (b)). In contrast, the thermal equation (Equation 2.40, Section 2.8) was solved only for the Ω_{SC} domain. The value of the applied field as well as the thermal exchange between the superconductor and the cooling stage was accounted for by means of the boundary conditions: at a large distance from the MgB_2 shield, the magnetic flux density $\mathbf{B}$ was supposed to be equal to $\mu_0 \mathbf{H}_{app}$ and to increase with a ramp rate of 0.035 T/s, i.e. referring to the boundaries labelled in Figure 6.1(b):

$$B_z = \mu_0 H_{app}(t) \qquad \text{on } \Gamma_1 \tag{6.11}$$

$$B_r = 0 \qquad \text{on } \Gamma_1 \cup \Gamma_7 \cup \Gamma_8 \cup \Gamma_9 \tag{6.12}$$

with the initial condition $B_z = \mu_0 H_{app}(t = 0) = 0$. In the experiment, the shield was in vacuum and cooled through the thermal contact with the cooling stage of a cryogen-free cryocooler [137]. To improve this contact, all the external surfaces of the cup ($\Gamma_2, \Gamma_3, \Gamma_4$ boundaries in the cross-section scheme in Figure 6.1(b)) were wrapped with an indium layer. Consequently, in the calculations, I assumed heat exchange only across the surfaces covered by the indium layer whose temperature was kept constant and set to T_{OP}, i.e:

$$\mathbf{n} \cdot (-\kappa(T) \cdot \nabla T) = \Upsilon \cdot (T_{OP} - T) \qquad \text{on } \Gamma_2 \cup \Gamma_3 \cup \Gamma_4 \tag{6.13}$$

$$\mathbf{n} \cdot (-\kappa(T) \cdot \nabla T) = 0 \qquad \text{on } \Gamma_5 \cup \Gamma_6 \tag{6.14}$$

where $\mathbf{n}$ is the unit vector normal to the sample surface and Υ is a heat transfer coefficient determined through iterative adjustments starting from the value reported in [132, 176] for similar experimental conditions.

Since I could not carry out calorimetric measurements on the sample, I got the temperature-dependent behaviour of the thermal conductivity, $\kappa(T)$, and the heat capacity, $C(T)$, (Equation 2.40) from literature. However, the thermal characterizations of MgB_2 bulks are, in general, not so comprehensive, and only a few papers report complete studies of the thermal characteristics of MgB_2 samples.

It is worth noting that, to the best of my knowledge, there is just one paper reporting information on both the thermal conductivity and the specific heat of MgB_2 samples obtained by an ex-situ technique [177]. However, the thermal conductivity data reported in that paper did not allow me to reproduce the experimental data successfully. Therefore, I also consider the $\kappa(T)$ and $C(T)$ behaviours presented

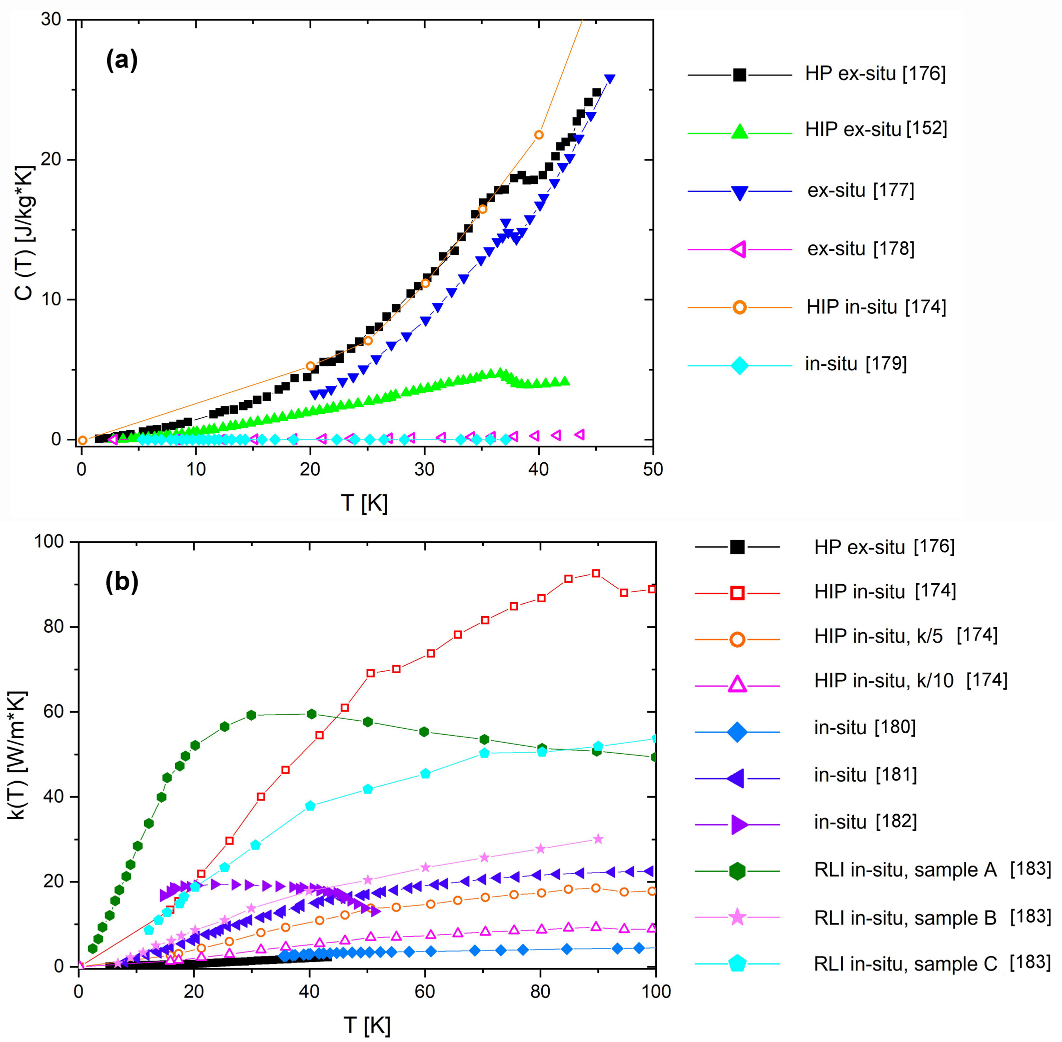

Fig. 6.2 Comparison of (a) $C(T)$ and (b) $\kappa(T)$ curves taken from literature [152, 175, 177–184].

in other papers, independently of the fabrication techniques. In Figure 6.2(a)-(b) the most relevant $C(T)$ and $\kappa(T)$ curves of MgB_2 samples obtained with different techniques, both in-situ and ex-situ [152, 175, 177–184] are collected, respectively. The value chosen for our simulations are those corresponding to the sample HIP#38 presented in reference [175]. In more detail, the criterion that guided my choice was the following. From Figure 6.2(a) one can see that the heat capacity curve of the HIP#38 sample obtained by the in-situ techniques (orange symbols) collapses to the curve reported by Anshukova et al. [177], for samples obtained by the HP ex-situ technique (black symbols) [152, 175, 177–180]. Moreover, the sample HIP#38 [175], the sample of Ref. [177] and my sample have a comparable mass density value, i.e. 2360 kg/m^3, 2560 kg/m^3 and 2500 kg/m^3, respectively. Hence, I decided to use the $C(T)$ curve reported in [175]. On the other hand, the comparison between the $\kappa(T)$ curves (Figure 6.2(b)) shows a strong dependence of the thermal conductivity on the analysed samples and precursor used [175, 177, 181–184]. Indeed, the $\kappa(T)$ behaviours are not comparable even for samples manufactured with the same techniques, as in the case of reference [184] where the samples A, B and C were obtained by Reactive Liquid Infiltration (RLI) but using different boron powders. Also, SPS samples fabricated with MgB_2 powders of different purity showed a different thermo-magnetic instability occurrence (P. Badica, from private communication), which can be the signature of a different thermal conductance. For these reasons, I chose the $\kappa(T)$ reported in [175] and divide it by a factor 5 to take into account that the addition of the BN powder degrades the thermal properties of the materials and to better reproduce the experimental data. Table 6.1 summarizes all the parameters used in this coupled electromagnetic-thermal model.

Parameters	Description	Value
E_0	Threshold electric field	10^{-5} V m^{-1}
T_c	Critical temperature (measured [64])	38.9 K
σ_{norm}	normal state conductivity (Eq.6.6)	10^{8} S m^{-1}
α	Parameter of $J_{c0}(T)$ (Eq.6.8)	4.841×10^{9} A m^{-2}
$\tilde{\alpha}$	Parameter of $J_{c0}(T)$ (Eq.6.8)	1
a	Parameter of $J_{c0}(T)$ (Eq.6.8)	1.507
β	Parameter of $B_0(T)$ (Eq.6.9)	1.658 T
$\tilde{\beta}$	Parameter of $B_0(T)$ (Eq.6.9)	5
b	Parameter of $B_0(T)$ (Eq.6.9)	1.694
l	Parameter of $\gamma(T)$ (Eq.6.10)	0.024 K^{-1}
g	Parameter of $\gamma(T)$ (Eq.6.10)	0.003 K^{-2}
ρ_m	MgB_2 mass density (measured [64])	2590 kg m^{-3}
Υ	Heat transfer coefficient (Eq.6.13)	3000 Wm^{-2}K^{-1}

Table 6.1 Parameters used for the physical modeling of the MgB_2 shield.

In the following sections, the numerical results obtained by means of the coupled model will be shown, comparing the computational outputs with the experimental data for different operational temperatures. After its validation, the model was employed to analyse and study possible solutions to mitigate the flux jump phenomenon.

6.2 Numerical simulation results and comparison with experimental data

In order to validate the reliability of the model, the comparison between the measured magnetic flux density values (symbols) and those computed both using the electromagnetic-thermal coupled approach (dashed lines) and the only electromagnetic model (solid lines) is plotted in Figure 6.3. In the latter case, where only the dependence of J_c on the local magnetic field was taken into consideration, the parameters J_{c0}, B_0, and γ were deemed constant and equal to the outputs of equations (6.8), (6.9), and (6.10) where T was set to T_{OP} = 30K. Moreover, as done in the previous studies, the magnetic flux density values were calculated in the same positions along the cup axis where the Hall probes were positioned during the experiment (see Figure 3.6(a)).

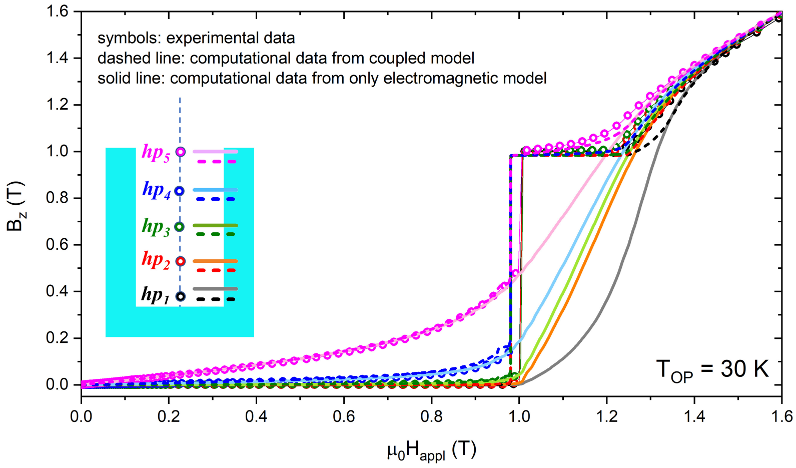

Fig. 6.3 Comparison between B_z values measured in the axial field orientation at T_{OP} = 30 K by Hall probes placed along the axis of the SC shield (open symbols) and the corresponding curves calculated by numerical simulations (dashed and solid lines, see text).

Figure 6.3 illustrates how coupling the electromagnetic and thermal equations enabled me to accurately reproduce the occurrence of the flux jump in the superconductor, which was not found when, considering a homogeneous field penetration, only the electromagnetic equations were taken. In addition, Figure 6.4 displays the corresponding SF curves determined through measurements (symbols) and numerical computations (dashed and solid lines). Once more, it is clear that the numerical analysis carried out using the electromagnetic-thermal approach (dashed lines) accurately predicts the abrupt deterioration of the shielding properties following the occurrence of the flux jump at $\mu_0 H_{app} \approx 1$ T, in remarkable agreement with the measured values. On the other hand, the results obtained with the electromagnetic-only model (solid lines), which predicts a smooth weakening of the SF, does not replicate this severe degradation of the cup shielding capacity.

As mentioned in Section 2.8, a flux jump occurs when the balance between the Lorentz and pinning forces is not fulfilled, causing a flux avalanche and the consequent Joule heating as a result. For this reason, I analysed the temperature maps of the sample in a time frame around the occurrence of the flux jump. Actually, the correlation of the evolution of the bulk temperature with the local values of

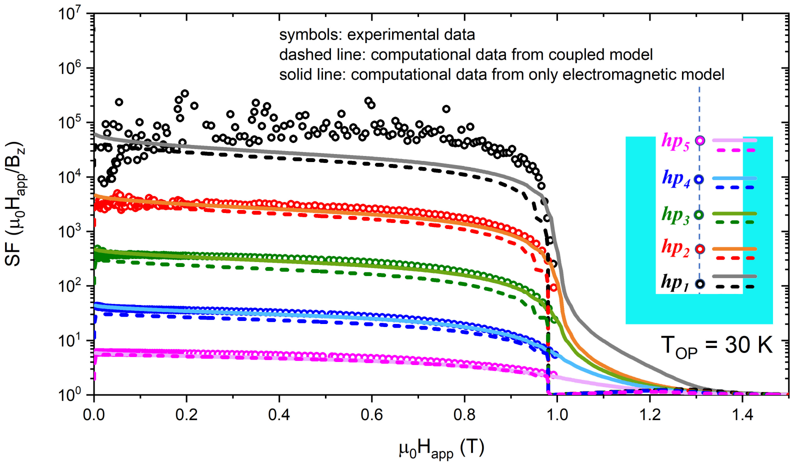

Fig. 6.4 Shielding factors measured by the Hall probes placed along the cup axis (symbols) and calculated at the same positions at T$_{OP}$=30 K. Dashed and solid lines correspond to the outputs of the coupled and electromagnetic-only models, respectively.

the field magnetic flux density can provide information on how to avoid or at least reduce this phenomenon. The magnetic flux density computed in correspondence to position hp_1 is shown in the same plot with the sample average temperature (Figure 6.5), assuming T$_{OP}$ = 30 K. Using the Comsol-implemented *Mean Probe* function defined within the superconducting region, the SC temperature is calculated as the average of the variable T. It is evident that the flux jump happens when the bulk average temperature (left red line) hits a maximum of 40.5 K. As a consequence, the magnetic flux density increases as the applied magnetic field completely penetrating the superconductor.

The detail of the evolution of the temperature peak and the magnetic flux density B as a function of the applied magnetic field is depicted in the inset of Figure 6.5. I considered five distinct time points to locally link the change in temperature, magnetic flux density, and current density during the jump, i.e. five different values of the applied magnetic field, near the peak: 0.9765 T (corresponding to t=t$_a$), 0.9800 T (t=t$_b$, when the flux jump starts), 0.9817 T (t=t$_c$, when the flux jump ends and the sample has lost its shielding ability), 0.9835 T (t=t$_d$), and 0.9870 T (t=t$_e$, when the starting temperature is nearly recovered). Figure 6.6 shows the temperature distribution in the SC domain (colour maps) and the **B**(r,z) vector plotted at the above-mentioned points in time. The corresponding current density maps are represented in Figure 6.7.

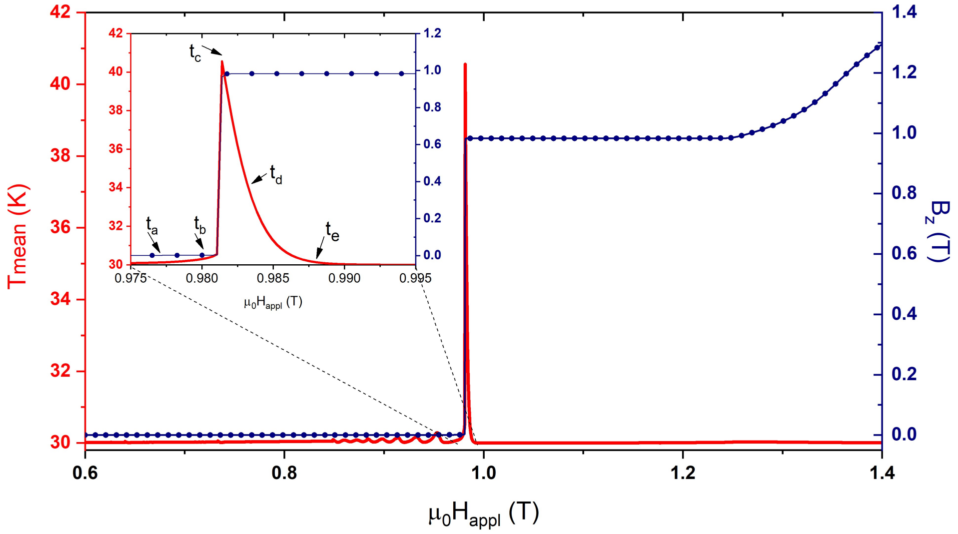

Fig. 6.5 Red curve: evolution of the mean temperature of the shield as a function of the applied magnetic field $\mu_0 H_{app}$. Blue curve: local magnetic flux density B calculated at position hp_1 along the axis of the cup-shaped shield at T$_{OP}$=30 K.
Inset: detail of the temperature peak. The moments t$_{a-e}$ refer to the moments at which the local temperature and current density distributions inside the bulk sample are mapped in figures 6.6 and 6.7.

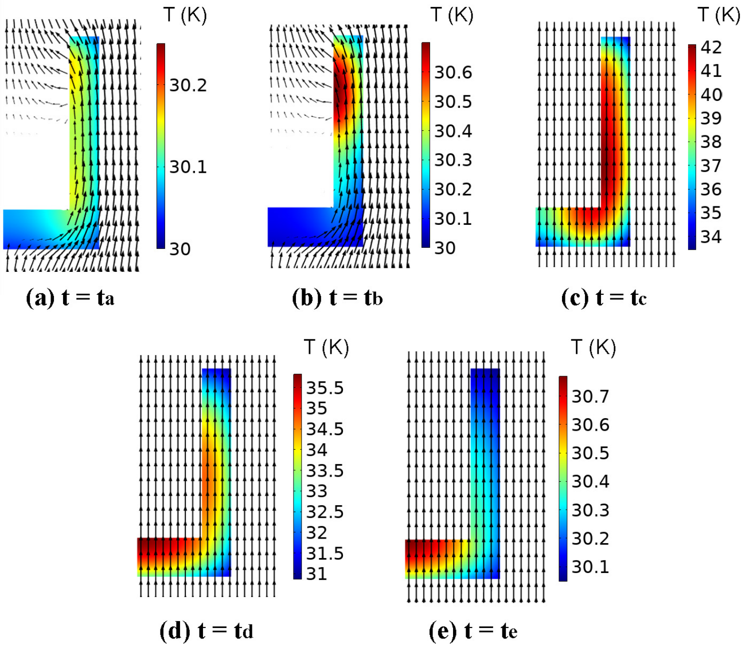

(a) t = ta **(b) t = tb** **(c) t = tc**

(d) t = td **(e) t = te**

Fig. 6.6 Magnetic flux density vector plots (cone) and temperature distributions (colour maps) for different values of applied magnetic field: 0.9765 T (t=t$_a$), 0.9800 T (t=t$_b$), 0.9817 T (t=t$_c$), 0.9835 T (t=t$_d$) and 0.9870 T (t=t$_e$).

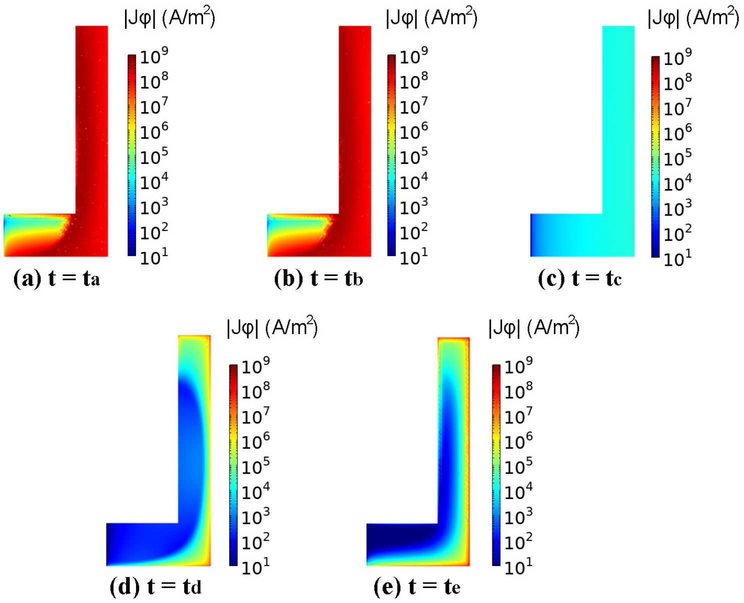

(a) t = ta **(b) t = tb** **(c) t = tc**

(d) t = td **(e) t = te**

Fig. 6.7 Current density distributions for different values of applied magnetic field: 0.9765 T (t=t$_a$), 0.9800 T (t=t$_b$), 0.9817 T (t=t$_c$), 0.9835 T (t=t$_d$) and 0.9870 T (t=t$_e$).

Figure 6.6 (a) and (b) demonstrates that the flux spike originates at a region along the inner wall of the cup, close to its open edge, where the temperature begins to rise. Indeed, as indicated by the **B** vector plot superimposed on the temperature map, there is a remarkable gradient of the magnetic flux density in this region. Accordingly, in the same region, the current density reaches its maximum value (Figure 6.7 (a) and (b)). Taking into account the shielded field, it is clear that the flux lines have just partially penetrated the superconductor before the flux-jump occurrence (Figure 6.6 (b)) and that the rapid rise in temperature (Figure 6.6 (c)) results in an instantaneous field penetration in the whole shield inner region. Once the flux jump occurred, the sample begins to cool down due to heat exchange with the cryocooler cooling stage, progressively lowering its temperature down to the operating one, T_{OP}=30 K (Figure 6.6 (d) and (e)). The shielding abilities, however, are no longer restored.

When the flux jump happens, the current density suddenly drops (t=t$_c$, Figure 6.7 (c)) according to the temperature and magnetic flux density distributions. Actually, the value of the current density decreases by more than three orders of magnitude. When the temperature returns to 30 K (t=t$_d$ and t=t$_e$, Figure 6.7 (d), (e)), it begins to rise once more in the outermost sheet of the lateral wall of the shield due to the establishment of a new magnetic flux density gradient, in turn induced by the continuous increase of the applied magnetic field.

Finally, to complete the study on the flux jump occurrence, I investigated the effect of the ramp rate of the external applied magnetic field. It is well known that this parameter affects the occurrence of the flux jump phenomenon, in particular higher ramp rates determine the increase of the flux jump occurrence at fixed temperature [130, 152]. In order to investigate this aspect, two further simulations with ramp rates equal to 0.35 T/s and 3.5 T/s at the working temperature T_{OP} = 30 K were carried out. The following plots (Figure 6.8) show the shielding curves calculated in the inner (hp_1, black lines) and outer positions (hp_5, magenta lines) along the cup axis for all the investigated ramp rates. The results are consistent with the previous study, i.e. the number of flux jumps increases as the ramp rate rises. I could not investigate slower ramp rates due to the too long calculation time.

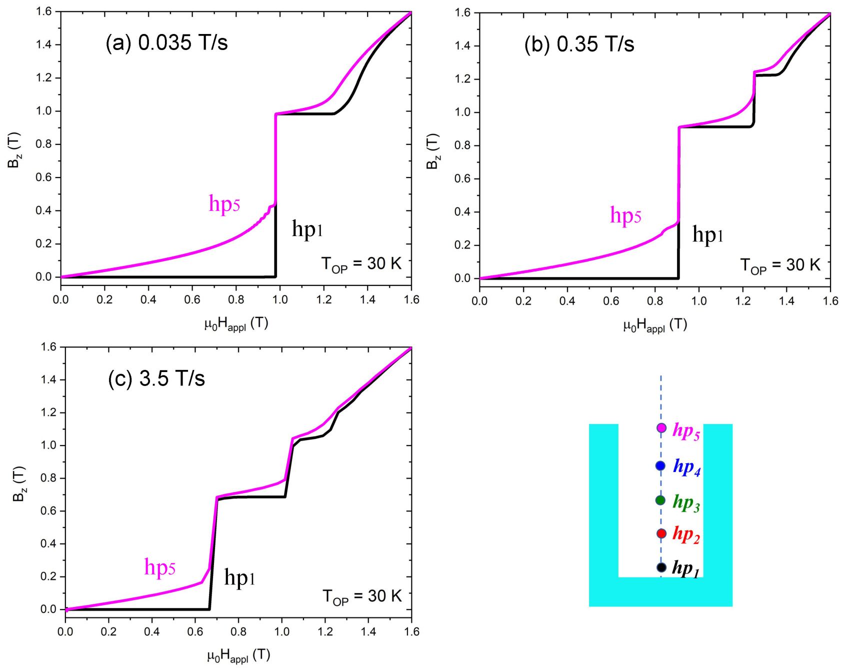

Fig. 6.8 Increasing frequency of the flux jump occurrence with increasing applied field ramp rate, i.e. 0.035 T/s (a), 0.35 T/s (b) and 3.5 T/s (c). hp_1 is located 1 mm above the closed extremity, hp_5 in correspondence to the shielding edge (i.e. 18.3 mm above the close extremity).

To achieve a further validation of this numerical procedure, the magnetic flux distribution along the shield axis at 25 K and 20 K was also calculated and compared with the corresponding experimental data. Figures 6.9 and 6.10 show how the coupling between the electromagnetic and thermal equations enables one to accurately reproduce the occurrence of the flux jumps observed in the experimental tests, including the double flux jump occurrence at 20 K for the applied field values $\mu_0 H_{app}$=1.82 T and 2.52 T. The curves obtained using the only electromagnetic model are also displayed to make a comparison.

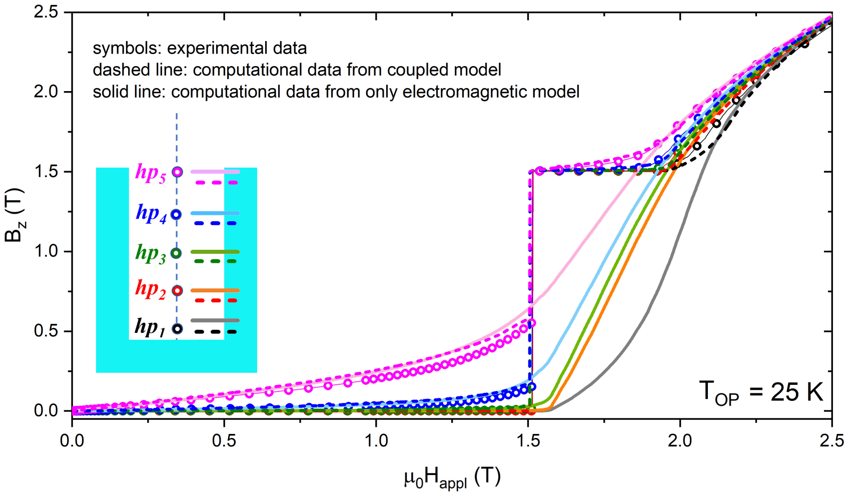

Fig. 6.9 Comparison between B_z values measured in the axial field orientation at T_{OP} = 25 K by Hall probes located along the axis of the SC shield (open symbols) and the corresponding curves calculated by numerical simulations (dashed line, coupled model; solid line, electromagnetic model only).

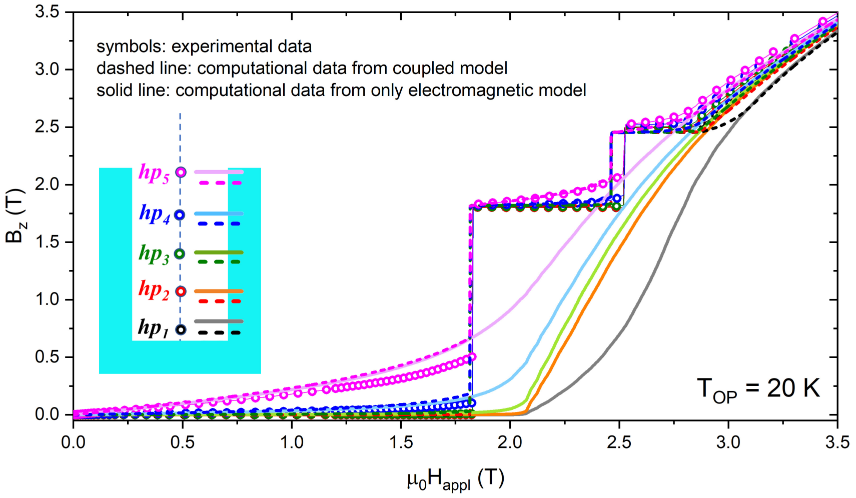

Fig. 6.10 Comparison between B_z values measured in the axial field orientation at T_{OP} = 20 K by Hall probes located along the axis of the SC shield (open symbols) and the corresponding curves calculated by numerical simulations (dashed line, coupled model; solid line, electromagnetic model only).

6.3 Influence of sample thermal conductivity and heat exchange on the flux jump occurrence

The as-validated modeling approach allows the study of potential solutions and enhancements to prevent or reduce the occurrence of thermo-magnetic instabilities or to move them to higher applied fields. An increased thermal exchange with the cooling system has been demonstrated to improve resilience against flux jumps [119]. Furthermore, using precursors ensuring that the MgB_2 bulk has better thermal properties could also avoid the incidence of thermo-magnetic instabilities [139, 115]. For this reason, I quantitatively assessed how improvements in MgB_2 thermal conductivity and/or in the heat exchange with the cooling stage can affect the flux jump occurrence and, consequently, the shielding factor of the cup, focusing on the T_{OP}=30 K. In order to handle the former issue higher $\kappa(T)$ value were assumed, while to match the latter issue, it was decided to impose the boundary condition (Equation 6.13) on the Γ_5 boundary as well, i.e. to also consider a heat exchange (cooling) across the inner lateral surface of the cup (Figure 6.1 (b)).

Figure 6.11 compares the B_z (Figure 6.11 (a)) and SF (Figure 6.11 (b)) curves calculated in Section 6.2 in correspondence to positions hp_1 and hp_3 - i.e. considering

$\kappa(T)$ values from [175] divided by 5 and the heat exchange as detailed in equation 6.13 (dot lines) – with those calculated assuming:

- $\kappa(T)$ values from [175] divided by 2 and the heat exchange as detailed in equation 6.13 (solid lines)
- $\kappa(T)$ values from [175] and the heat exchange as detailed in equation 6.13 (dashed lines)
- $\kappa(T)$ values from [175] divided by 5 and the heat exchange (see equation 6.13) on boundaries $\Gamma_2 \cup \Gamma_3 \cup \Gamma_4 \cup \Gamma_5$ (triangular symbols)
- $\kappa(T)$ values from [175] and the heat exchange (see equation 6.13) on boundaries $\Gamma_2 \cup \Gamma_3 \cup \Gamma_4 \cup \Gamma_5$ (circular symbols)

From this comparison, I can say that the flux jump occurs at slightly higher values of the applied field when a greater value of $\kappa(T)$ is assumed. Consequently, the SF deteriorates at 1.02 T under the assumption that $\kappa(T) = \kappa(T)[175]$ against 0.98 T assuming $\kappa(T) = \kappa(T)[175]/5$. On the other hand, for all the $\kappa(T)$ values considered, the assumption of a heat exchange across the shield inner wall completely eliminates the occurrence of these thermo-magnetic instabilities.

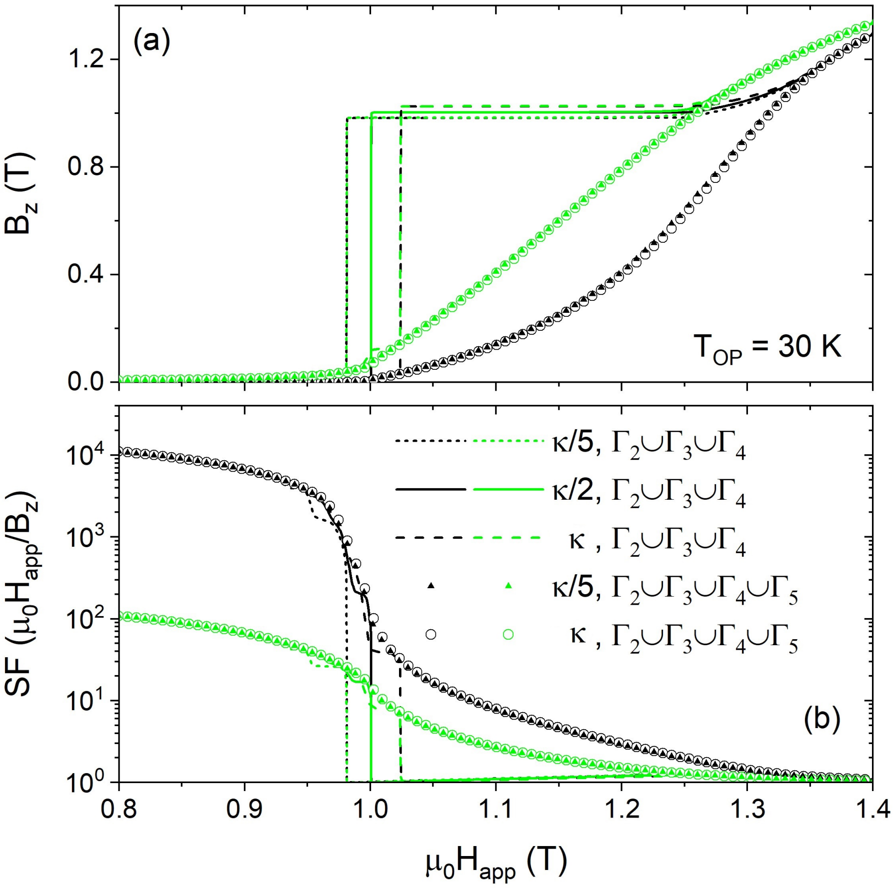

Fig. 6.11 B_z (a) and SF (b) values calculated assuming $\kappa(T)$ values from [175] divided by 5 (short dashed lines), $\kappa(T)$ values from [175] divided by 2 (solid lines), $\kappa(T)$ values from [175] (dashed lines) and heat exchange across boundaries $\Gamma_2 \cup \Gamma_3 \cup \Gamma_4$. Closed and open symbols represents the curves evaluated assuming $\kappa(T)$ values from [175] divided by 5 and pristine, respectively, and heat exchange across boundaries $\Gamma_2 \cup \Gamma_3 \cup \Gamma_4 \cup \Gamma_5$. Black and green curves refer to hp_1 and hp_3 positions, respectively.

6.4 Preliminary study of the effect of the FM shield superimposition on the flux jump occurrence

Exploiting the coupled model presented in the previous sections, the role of the ferromagnetic layer addition to prevent the flux-jump occurrence will also have to be studied numerically. The reasons of this investigation are based on experimental results obtained at 20 K for the tube-shaped shields. Although at high temperatures thermo-magnetic instabilities were not detected in the SC tube-shaped shield (Figure 4.1, Section 5.4.1), at 20 K flux-jumps also appear in it. This different behaviour can be attributed to the different MgB_2 concentration in the starting powder. Actually, less MgB_2 phase in the sample usually provides fewer flux-jumps and the MgB_2 phase concentration in the starting powder used for the fabrication of the tube is lower (87.9 wt.%) than that used for the fabrication of the cup (97 wt.%).

Figure 6.12 shows the magnetic flux density measured along the tube axis by Hall probes located at the same positions as in Figure 3.6 for the only SC shield (symbols) and for the hybrid SC+FM shields (lines) (for the layout schemes, see Figure 3.2 and 3.9, respectively).

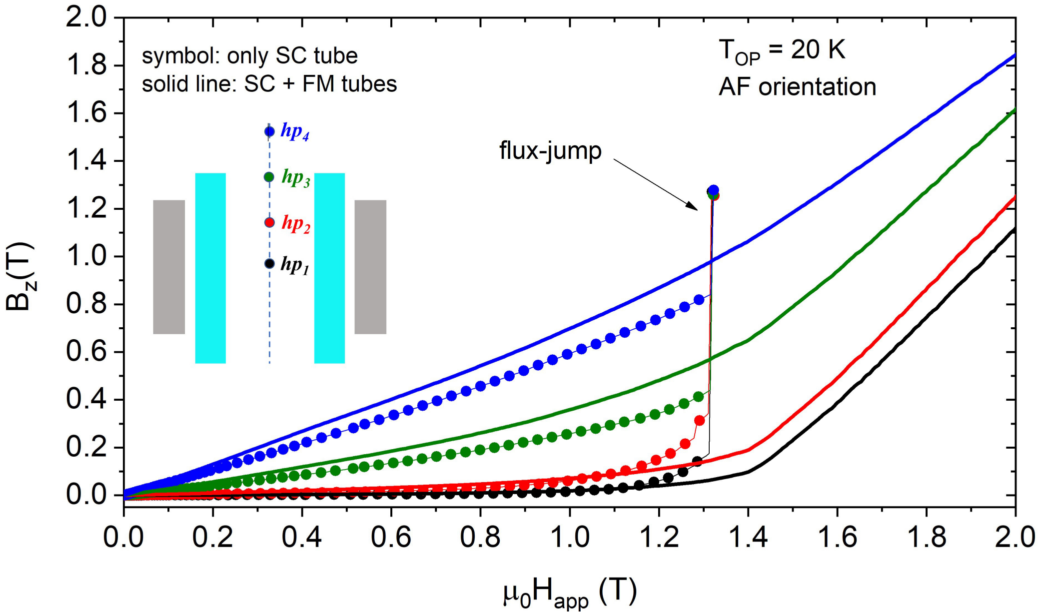

Fig. 6.12 Comparison between B_z values measured in the axial field orientation at T_{OP} = 20 K by Hall probes located along the axis of the SC (open symbols) and the SC+FM shields (solid lines). For Hall probe position, refer to Figure 3.6.

Remarkably, it can be seen that if the FM shield is added to the SC one, the flux-jump event does not happen and the shielding capability of the hybrid configuration is preserved.

This experimental evidence suggests that the FM shield could prevent the flux-jump occurrence, probably because it ensures a lower magnetic pressure at the SC shield wall. However, it is worth mentioning that the cryostat was equipped with an aluminium thermal shield whose temperature was higher than 50 K. Hence the FM shield, thermally anchored to the second cold stage of the cryocooler whose temperature was kept at T_{OP} = 20K, could also have worked as a further thermal shield against thermal radiation avoiding the flux-jump occurrence.

Thus, to deeply investigate this possible improvement, the electromagnetic-thermal model will be employed to explore the effect of the superimposition of a FM shell on the occurrence of these thermo-magnetic instabilities in the SC shield.

Chapter 7

Conclusion

In this dissertation, a combined experimental and theoretical analysis of MgB_2 and hybrid solutions for magnetic shielding applications are presented, with a particular focus on the effects of the shield geometry, the applied field orientation and the thermo-magnetic instabilities. Experimentally, the shielding properties of MgB_2 hollow cylinders without and with a closing cap and a MgB_2+FM tube-shaped shields were investigated at different operational temperatures for both axial and transverse applied magnetic fields. Numerically, a 2D axisymmetric and a 3D modeling approaches based on the **A**-formulation were employed to analyse new shielding configurations, to investigate the effect of a tilted applied magnetic field and to study the flux jump occurrence experimentally detected.

In more detail, the first part of this work deals with the experimental characterization of the shields. For this purpose, the magnetic flux density was measured by cryogenics Hall probes placed at different positions along the shield axis in both axial and transverse magnetic field orientations. The characterization was carried out in a temperature range between 20 and 35 K. However, after the analysis of the shielding properties on temperature dependence, I focused on the results obtained at 30 K, for which the practical constraints well encounter the shielding abilities. At this temperature, despite the flux jump occurrence, the cup-shaped shield turns out to be the most efficient layout, reaching, in the AF orientation, SFs value greater than 10^4 near the close extremity against the SF ≈ 150 at the centre of the SC tube. Furthermore, the study highlighted a dependence of the shielding performances on the applied field orientation: indeed, for both the geometries, worse shielding performances were obtained in the TF orientation. With the aim to improve the shielding ability in this orientation, the role of a ferromagnetic shell superimposition on the SC tube shield was experimentally investigated, as well. It turned out that the addition of the FM shell can actually improve the shielding ability, enhancing the SF of the hybrid configuration of $\approx 83\%$ with respect to that obtained with the SC-only shield.

Relying on these results and taking advantage of the computational tools, a 3D numerical model based on the **A**-formulation was implemented to deeply investigate the role of the FM addition on the SC shield properties and to extend the study also to new hybrid layouts. Therefore, the second part of this dissertation focuses on the development and validation of this numerical model. To this aim, two approaches were used, i.e. the comparison of the as-computed magnetic flux density values with the experimental data and with the numerical results achieved by solving a benchmark problem employing the well established **H**-formulation. In both the cases, a valuable agreement was found. This agreement guarantees that the model enables a trustworthy SF calculation when the field penetration into the superconductor is uniform.

Next, using this as-validated model, I calculated the screening ability of novel hybrid shield layouts made up of SC and FM coaxial tubes and cups subjected to applied fields tilted of different angles with respect to the shield axis. The effect of the FM shield was investigated as a function of its height with respect to that of the SC shield. The study revealed that the superimposition of FM shell is an effective way to reduce the sharp decline of the shielding ability of short SC screens when the external field is rotated away from their symmetry axis, even of a small angle. Notably, if the FM shield open edge(s) protrude over the SC shield edge(s), the positive influence of the FM addition is even amplified. Conversely, in the TF orientation, the superimposition of the FM shield causes a small SF decrease at low applied fields but, once again, when the FM cup protrudes above the SC one, this worsening is minimized.

Finally, the electromagnetic model based on the **A**-formulation was coupled with the heat diffusion equation to predict the effects of the flux-jump occurrence on the magnetic shielding performance of the MgB_2 cup shield. Since flux jumps were experimentally observed just in the AF orientation, taking advantage of the axial symmetry of the shield, a 2D axisymmetric coupled model was formulated and validated by comparing the computational output with the experimental results, considering as operational temperatures 20 K, 25 K and 30 K. The analysis demonstrates that this model quantitatively reproduces the experimental shielding factor curves and their sharp drop as a result of a flux jump occurrence. Moreover, focusing on 30 K, I correlated the evolution of the local magnetic field, temperature, and current density in the superconductor with the sudden worsening of the cup shielding performance. The model was then employed to look into how the material thermal conductivity and the thermal exchange with the coolant affect the shielding qualities. It turns out that increasing the thermal conductivity has a far less effect on the shielding factor than the thermal contact improvement, which can even prevent the occurrence of flux jumps.

In summary, this work shows that the combination of experimental characterization with the possibility to predict the superconducting behaviour by numerical tools can be a key point to guide and optimize the shape of superconducting shielding devices and their efficiency, identifying the most suitable solutions. The research project relied on the results presented in this thesis is still ongoing. The role of FM shield addition to prevent or mitigate the flux jump occurrence will be the next issue to be addressed by the electromagnetic-thermal model. Additionally, I am working on the implementation of a 3D fully-cryogenic scanning system to be mounted on the experimental apparatus used for the shielding measurements. It will hold a Hall probe array and allow us to map magnetic flux density distributions with micrometric resolution. Actually, all the experimental measurements presented in this work were obtained using Hall probes held in fixed positions. This new approach will result in a substantial improvement since it will enable the construction of comprehensive magnetic flux density maps, e.g. inside magnetic shields or close to permanent magnets.

Appendix A

Bi-2223 cup-shaped shield

Relying on the results obtained with the MgB_2 shields, during a two-months stay at the University of Liege (in the group of Prof. Philippe Vanderbemden), I addressed the study of the shielding ability of a Bi-2223 vessel (Figure A.1). According to the approach followed in the MgB_2 analysis, the experimental activity was coupled with a numerical modelling work.

The Bi-2223 belongs to the Bismuth Strontium Calcium Copper Oxide (BSCCO) family, having the generalized chemical formula $Bi_2Sr_2Ca_{n-1}Cu_nO_{2n+4+x}$. It was discovered in 1988 by Maeda *et al.* [185] and it was the first SC which did not contain rare-earth elements. One of the main advantages of this material is the possibility to grown and shape Bi-2223 samples as large vessels [52], making this material suitable for magnetic shielding applications. Under this perspective, several studied have been reported on its shielding capacity, investigating Bi-2223 shields of various aspect ratios and subjected to axial and transverse applied magnetic fields [51, 61, 63].

In this work, the shielding abilities of a commercial Pb-doped Bi-2223 polycrystalline vessel with a hemispherical bottom (CAN Superconductor, CSV-12), hereafter referred to as cup, was investigated in both axial (AF) and transverse (TF) applied magnetic field orientation with respect to the axis of the sample. The final target of my investigation was the analysis and the comparison of the shielding properties of the cup after zero field cooling and when crossed fields were applied (i.e. the measurement of the SF in the axial field orientation after magnetizing the sample in a transverse field and viceversa). However, due to some troubles with both the sample and the measuring system, I could not meet this target and to date I've only completed the SF evaluation after zero field cooling, whose results are here reported. However, I'm going to complete this work in a near future.

Actually, two cups with the same geometry and comparable dimension have been characterized, since the first sample got damaged. For the sake of clarity, let me define CUP-T as the cup characterized in TF orientation (the broken one) and CUP-A as the cup characterized in AF orientation. I started the characterization of CUP-T in TF orientation but, unfortunately, the cup was damaged after the first measurements in axial field orientation. For this reason, a second cup, CUP-A, was characterized in AF orientation. The main problem, as one can see in the next sections, is that all the parameters needed to numerically described the sample are extrapolated from the axial measurements, hence I did not have enough data to properly reproduce CUP-T behaviours. In Table A.1 the dimension of the cups are listed, while Figure A.1 shows a picture and a schematic view of the sample and Hall probe (*hp*) positions.

	R_e [mm]	R_i [mm]	h_e [mm]	h_i [mm]
CUP-T	15.19	12.03	44. 90	43.33
CUP-A	15.19	12.04	44. 90	43.33

Table A.1 Dimension of the cups characterized in TF (CUP-T) and AF (CUP-A), where R_e is the external radius, R_i the inner radius, h_e the external height and h_i the internal depth.

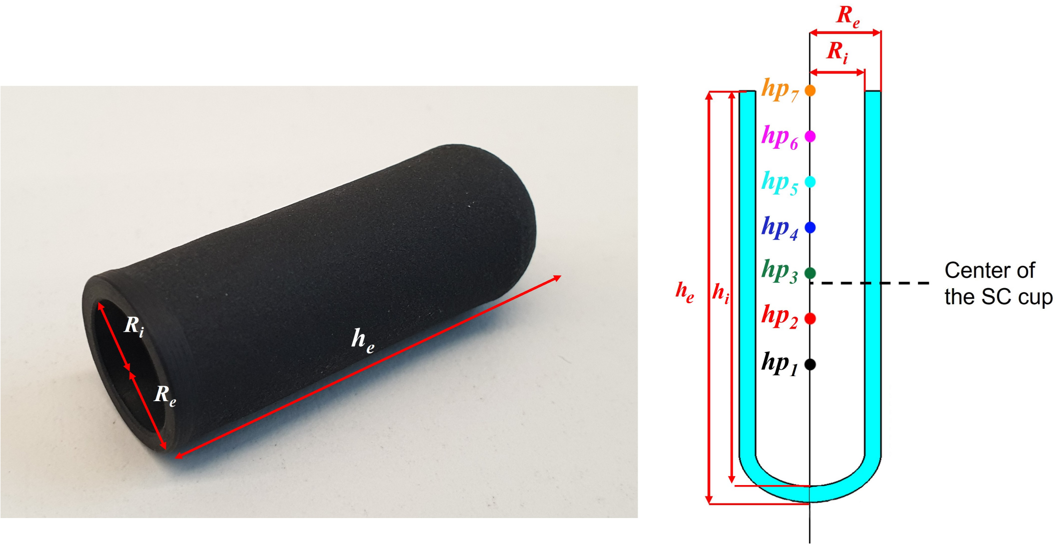

Fig. A.1 Picture of a cup-shaped Bi-2223 shield (left) and its schematic view with the positions of the Hall probes *hp* (right).

The shielding properties of the samples were investigated at 77 K, placing the cups in the nitrogen bath. For the AF characterization I used an electromagnet reaching a maximum applied field of 60 mT; while for TF characterization Helmholtz coils generating magnetic field up to 250 mT were employed. The magnetic flux density was measured by a cryogenic Arepoc® Axis-3S Hall probe at different positions along the cup axis. The right part of Figure A.1 shows the schematic view of the *hp* positions, placed at hp_1=13.3 mm, hp_2=18.3 mm, hp_3=23.3 mm, hp_4=28.3 mm, hp_5=33.3 mm, hp_6=38.3 mm and hp_7=43.3 mm from the inside bottom of the cups.

A.1 Numerical model

3D simulations were implemented in order to reproduce the experimental data in both AF and TF orientations. The numerical model is based on the **A**-formulation reported in Section 2.5 and the electromagnetic behaviour of the superconducting and the surrounding domains is described solving the Maxwell equations by means of Comsol Multyphisics®. Unlike the simulations on the MgB_2 shields, the superconducting behaviour was modelled using the power law expression (Equation 2.15) between the current density and the electric field, according to Ref. [186].

However, since the equations are formulated as function of the vector potential **A**, a not conventional form for the power law equation was used, i.e. the relation $\mathbf{J} = \sigma\mathbf{E}$, present in the Ampere Law module in Comsol, was customized introducing the *E-J* power law dependence in the electrical conductivity (defined only for the SC domain), which took the form:

$$\sigma = \frac{J_c(B)}{E_0} \cdot \left|\frac{|\mathbf{E}|}{E_0}\right|^{\frac{1-n}{n}} \tag{A.1}$$

Taking advantage of the tubular geometry of the samples, the value of J_c, needed to determine the $J_c(B)$ dependence, was again calculated from the magnetic induction cycles relying on the approach proposed by Bartolomé *et al.* for finite superconducting rings [167]. This procedure was applied to the magnetic flux density cycles obtained in the AF orientation (i.e. on sample CUP-A) and I used the value measured by the Hall probe, B_{meas}, located at the open edge of the cup (hp_7), since in that position the effects of the cup closure can be disregarded. In agreement with Ref. [187], the experimental $J_c(B)$ curve was then fitted by Kim equation:

$$J_c(B) = \frac{J_{c0}}{\left(1 + \frac{B}{B_1}\right)} \tag{A.2}$$

obtaining the fit parameter values J_{c0} = 1.3 $\cdot 10^7$ A/m^2 and B_1= 0.00615 T.
Regarding the *n* parameter, I calculated it following two different procedures. The first *n* estimation was achieved performing a *relaxation creep experiment* [61], from which the normalized flux creep rate *S*, related to *n* by the equation:

$$S = \frac{1}{1-n} \tag{A.3}$$

was calculated, obtaining *S*= -0.01318, hence *n* = 76.

The second evaluation procedure is based on the method proposed in Ref. [188]. According to this procedure, the magnetic flux density at position hp_1 was measured using different ramp rate of the applied field in AF orientation. Firstly, fitting the measured data, an *apparent* exponent *n'*=55 was found. However, this value of *n'* is overestimated, being defined as:

$$n' = n(1+\gamma) \tag{A.4}$$

Taking the value of γ equal to 0.65, in agreement with Ref. [188], I obtain n = 33. Calculations were carried out employing both the n-value. However, it is worth underlying that the use of one value of n rather than the other one does not significantly affect the result, as shown in Figure A.2 where the magnetic flux density curves, B_{calc}, calculated at position hp_1, hp_5 and hp_7 for n=76, 55 and 33 are plotted.

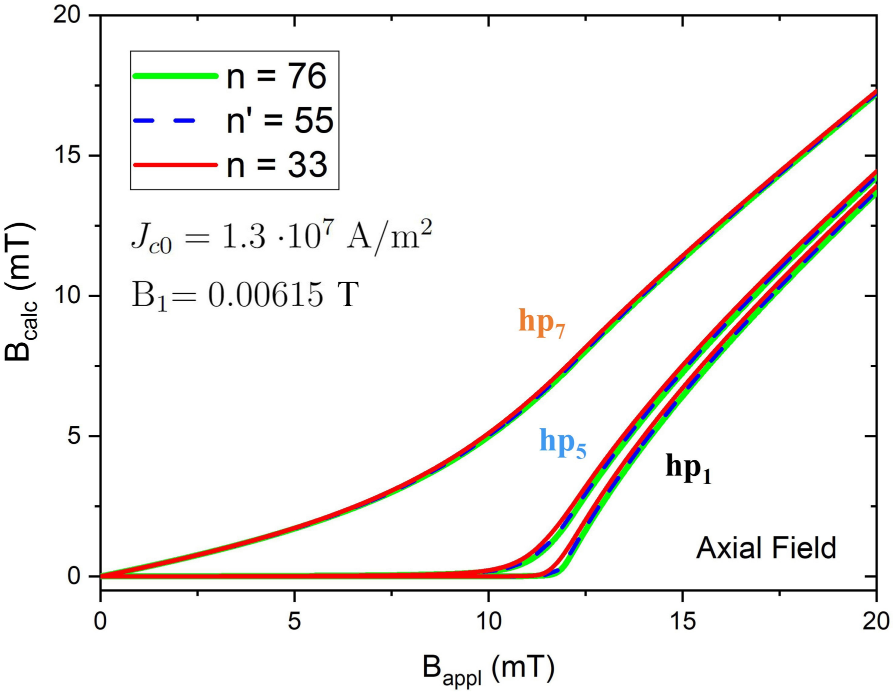

Fig. A.2 Comparison among the magnetic flux density curves calculated at position hp_1, hp_5 and hp_7 (Figure A.1) in the AF orientation. The SC domain was described by Equation 2.36 with J_{c0} = 1.3 $\cdot 10^7$ A/m^2, B$_1$= 0.00615 T, n=76 (green solid line), n'=55 (blue dashed line) and n=33 (red solid line).

A.2 Results

Figure A.3 shows the comparison between the experimental data (open symbols) and the computational output (lines) at the positions hp_1, hp_5 and hp_7 along the cup axis when an axial field is applied. Actually, the magnetic flux density was measured for all the seven positions along the axis, but here only three of them are shown for clarity. The comparison reveals a good agreement between the two sets of data, although some differences can be observed in the range 10-15 mT for position hp_1.

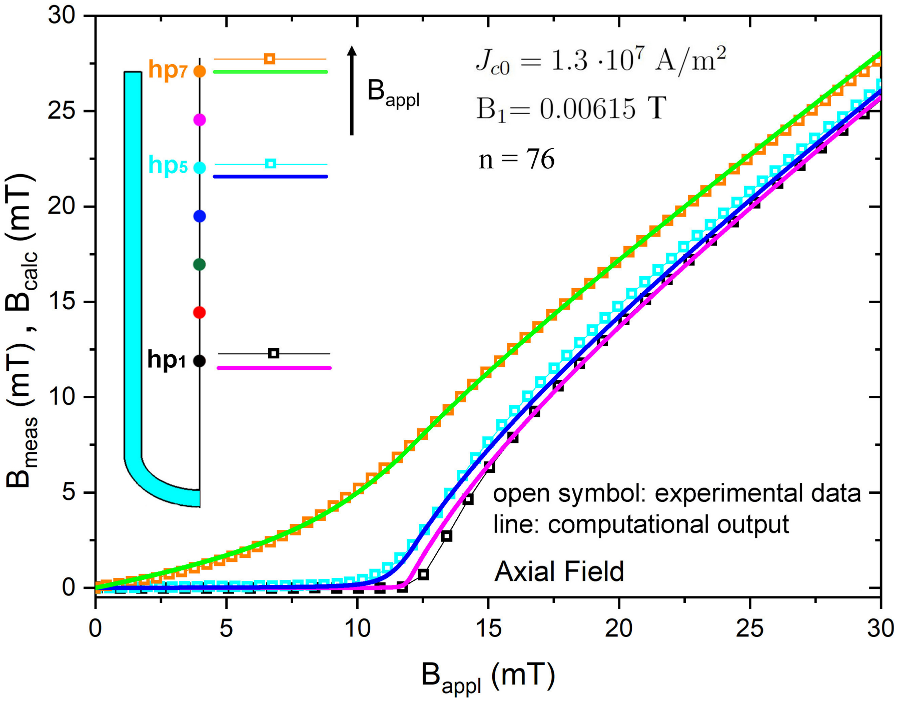

Fig. A.3 Comparison between the magnetic flux density measured along the cup axis by Hall probes hp_1, hp_5 and hp_7 (symbols) and the corresponding values computed by numerical simulations (lines) in the AF orientation.

The parameters J_{c0} and B_1 extrapolated from the magnetization cycle in the AF orientation should properly describe the superconducting behaviour of the sample in the transverse field orientation as well. However, even though from a first analysis the cups seemed to have the same characteristics, the simulated output obtained with the parameter values calculated with the magnetic flux density of CUP-A (J_{c0} = 1.3 $\cdot 10^7$ A/m^2, B_1= 0.00615 T and n=76) could not reproduce the experimental data in the TF orientation, as shown in Figure A.4.

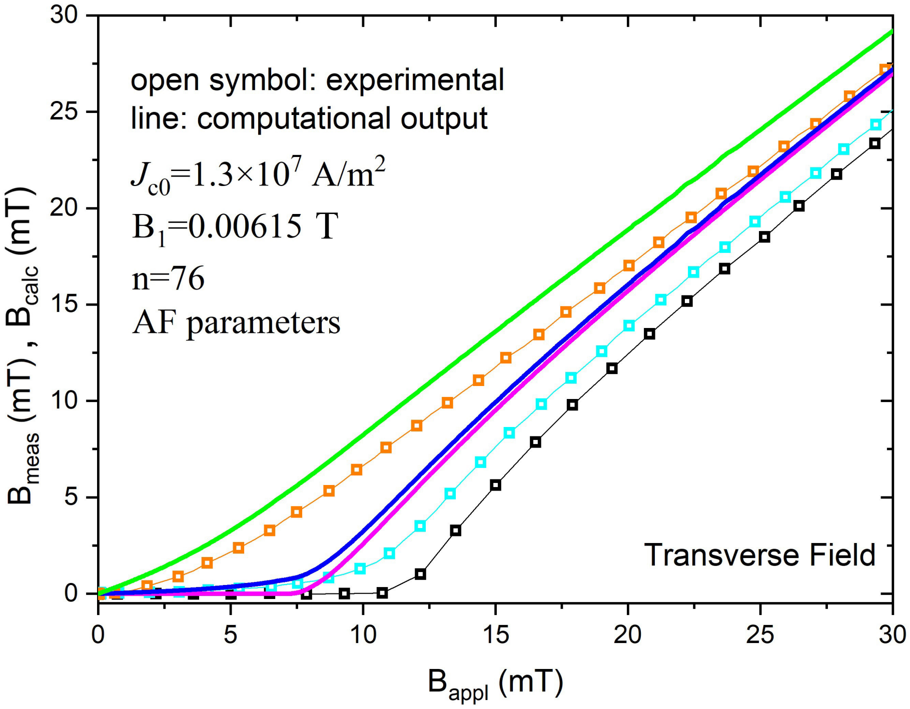

Fig. A.4 Comparison between the magnetic flux density measured along the cup axis by Hall probes hp_1, hp_5 and hp_7 (symbols) (Figure A.1) and the corresponding values computed by numerical simulations (lines) in the TF orientation, where the numerical parameters extracted by the analysis in the AF orientation were employed.

This is probably due to the fact that samples CUP-A and CUP-T are not fully comparable from a superconducting point of view. This could also be noted in Figure A.5, where the shielding curves measured at hp_1 position in both the AF (open symbols) and TF (close symbols) orientations are shown. It can be seen that the two curves intersect each other at ≈14 mT, while they should collapse when the applied magnetic field exceed the full penetration value. This could be evidence that the samples can not be described by the same parameters.

In order to try and define new parameters suitable also for the TF simulation, I considered the AF data obtained from CUP-A but shifted of 1.4 mT (both along the B_{appl} and B_{meas} axis) to make the AF and TF curves overlap at high applied fields. Indeed, the idea is to suitably shift the entire magnetic flux density cycle of CUP-A so as to make it overlap with the CUP-T cycle at high fields and then employ the shifted cycle to extract the proper $J_c(B)$ parameters. The result is shown in Figure A.5, where the shifted data are represented by the red solid line for the innermost hall probe hp_1. It is worth pointing out that the same shift provides the collapse of the AF and TF curves for all the Hall probe positions, including the data referred to the hp_7 position used to calculate the $J_c(B)$ parameters following the procedure proposed by Bartolomé *et al.* [167].

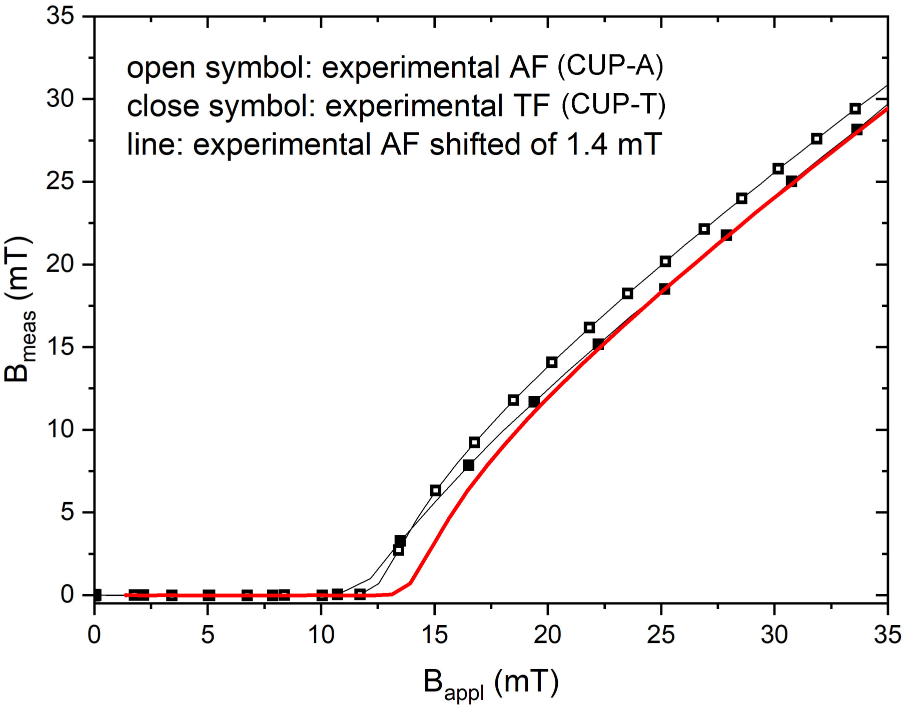

Fig. A.5 Comparison of the experimental data of CUP-A in the AF orientation (open symbol), of CUP-T in the TF orientation (closed symbol) and shifted data of CUP-A in the AF orientation (red solid line) measured in hp_1 position (Figure A.1).

Using this new set of data, the new value of J_{c0} and B_1 for CUP-T are J_{c0} = 1.3 $\cdot 10^7$ A/m^2 and B_1= 0.02035 T. Before the CUP-T got damaged, I was able to measure the magnetic flux density in the AF orientation just at position hp_1 with different ramp rate of the applied field. Therefore, I could determine the n parameter following the already described procedure. The *apparent* exponent n'=46 was found applying Equation A.4 and, with $\gamma = 0.65$, I obtained n=28. However, also in this case, the value of n does not significantly affect the computational output as one can see in Figure A.6

Table 6.1 summarizes the values of the parameters found for the two cups.

	J_{c0} [A/m^2]	B_1 [T]	n
CUP-A	1.30 $\cdot 10^7$	0.00615	76, 33 (n'=55)
CUP-T	1.30 $\cdot 10^7$	0.02035	28 (n'=46)

Table A.2 $J_c(B)$ parameters found for CUP-A and CUP-T.

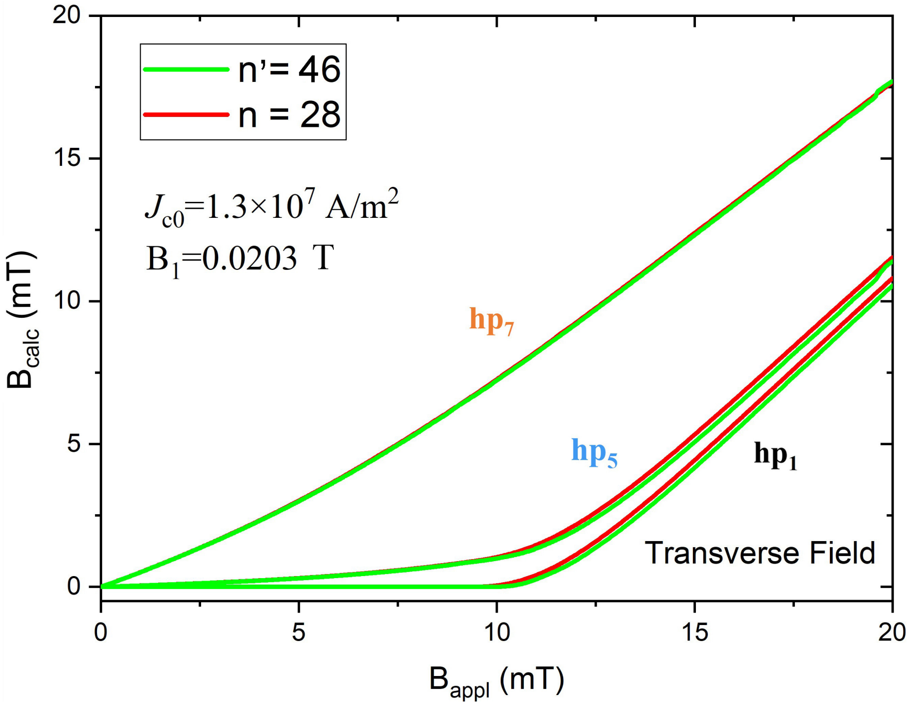

Fig. A.6 Comparison among the magnetic flux density curves calculated at position hp_1, hp_5 and hp_7 (Figure A.1) in the TF orientation. The SC domain was described by Equation 2.36 with J_{c0} = 1.3 ·10^7 A/m^2, B$_1$= 0.0203 T, n'=46 (green solid line) and n=28 (red solid line).

Figure A.7 shows the comparison between the experimental data (open symbols) and computational output (solid lines) calculated with the new parameters in the TF orientation. Considering position hp_1, the experimental and calculated curves are in excellent agreement up to ≈12 mT, i.e. when the external field starts to penetrate the shield. Over ≈12 mT the curves no longer overlap. In the same way, for position hp_5 the curves collapse on each other below ≈10 mT.

Despite the numerical results obtained in TF orientation are not in perfect agreement with the experimental ones, this analysis lays the foundation for a more comprehensive analysis of the shielding capabilities of these Bi-2223 shields. Taking advantage of the numerical tools, the further steps could be to investigate the effect of the superimposition of a ferromagnetic shell on the superconducting one and at the same time to explore the magnetic shielding properties of the "cross field" configuration, i.e. the shielding properties of the hybrid and superconducting shields, previously magnetized with an applied field perpendicular to the one used for the study of magnetic mitigation properties. The numerical analysis results will also guide the future shielding experiments in "crossed field".

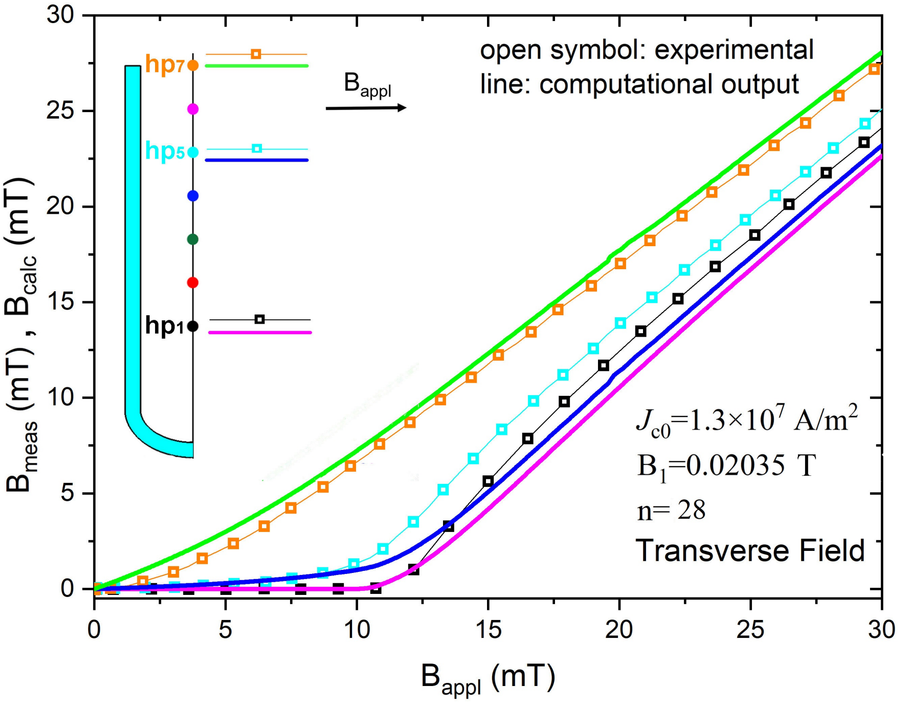

Fig. A.7 Comparison between the magnetic flux density measured along the cup axis by Hall probes hp_1, hp_5 and hp_7 (symbols) and the corresponding values computed by numerical simulations (lines) in the TF orientation.

References

[1] P Badica, G Aldica, M Burdusel, S Popa, R F Negrea, M Enculescu, I Pasuk, and L Miu. Significant enhancement of the critical current density for cubic bn addition into ex situ spark plasma sintered MgB_2. *Superconductor Science and Technology*, 27(9):095013, aug 2014.

[2] COMSOL Multiphysics®. (https://www.comsol.com/).

[3] Mykola Solovyov and Fedor Gömöry. A–v formulation for numerical modelling of superconductor magnetization in true 3d geometry. *Superconductor Science and Technology*, 32(11):115001, sep 2019.

[4] Gregory P. Lousberg, Jean-Francois Fagnard, Marcel Ausloos, Philippe Vanderbemden, and BenoÎt Vanderheyden. Numerical study of the shielding properties of macroscopic hybrid ferromagnetic/superconductor hollow cylinders. *IEEE Transactions on Applied Superconductivity*, 20(1):33–41, 2010.

[5] Jean-François Fagnard, Benoît Vanderheyden, Enric Pardo, and Philippe Vanderbemden. Magnetic shielding of various geometries of bulk semi-closed superconducting cylinders subjected to axial and transverse fields. *Superconductor Science and Technology*, 32(7):074007, 2019.

[6] H. Kamerlingh Onnes. Isotherms of monatomic gases and their binary mixtures. i. isotherms of helium between +100°c and -217°c. *KNAW, Proceedings*, 10 II:445–450, 1908.

[7] J. Bardeen, L. N. Cooper, and J. R. Schrieffer. Theory of superconductivity. *Phys. Rev.*, 108:1175–1204, Dec 1957.

[8] Müller K. A. Bednorz, J. G. Possible hightc superconductivity in the balacuo system. *Zeitschrift für Physik B Condensed Matter*, 64:189–193, Jun 1986.

[9] Jun Nagamatsu, Norimasa Nakagawa, Takahiro Muranaka, Yuji Zenitani, and Jun Akimitsu. Superconductivity at 39 k in magnesium diboride. *nature*, 410(6824):63–64, 2001.

[10] Watanabe Takumi Hirano Masahiro Hosono Hideo Kamihara, Yoichi. Iron-based layered superconductor la[o1-xfx]feas (x = 0.050.12) with tc = 26 k. *Journal of the American Chemical Society*, 130:3296–3297, Mar 2008.

[11] C.P. Poole, H.A. Farach, R.J. Creswick, and R. Prozorov. *Superconductivity*. Elsevier insights. Elsevier Science, 2014.

[12] D Uglietti. A review of commercial high temperature superconducting materials for large magnets: from wires and tapes to cables and conductors. *Superconductor Science and Technology*, 32(5):053001, apr 2019.

[13] Chao Yao and Yanwei Ma. Superconducting materials: Challenges and opportunities for large-scale applications. *iScience*, 24(6):102541, 2021.

[14] Paul Seidel. *Applied superconductivity: handbook on devices and applications*. John Wiley & Sons, 2015.

[15] Weijun Yao, Juan Bascunan, Woo-Seok Kim, Seungyong Hahn, Haigun Lee, and Yukikazu Iwasa. A solid nitrogen cooled mgb_2 "demonstration" coil for mri applications. *IEEE Transactions on Applied Superconductivity*, 18(2):912–915, 2008.

[16] Yasuaki Terao, Osamu Ozaki, Chikara Ichihara, Shinya Kawashima, Takashi Hase, Hitoshi Kitaguchi, Shin-ichi Kobayashi, Ken-ichi Sato, Iwao Nakajima, Naoki Oonishi, Michael Poole, Kazuyuki Takeda, Shin-ichi Urayama, and Hidenao Fukuyama. Newly designed 3 t mri magnet wound with bi-2223 tape conductors. *IEEE Transactions on Applied Superconductivity*, 23(3):4400904–4400904, 2013.

[17] J. Good and R. Mitchell. A desktop cryogen free magnet for nmr and esr. *IEEE Transactions on Applied Superconductivity*, 16(2):1328–1329, 2006.

[18] A. Ulbricht, J. L. Duchateau, W. H. Fietz, D. Ciazynski, H. Fillunger, S. Fink, R. Heller, R. Maix, S. Nicollet, S. Raff, M. Ricci, E. Salpietro, G. Zahn, R. Zanino, M. Bagnasco, D. Besette, E. Bobrov, T. Bonicelli, P. Bruzzone, M. S. Darweschsad, P. Decool, N. Dolgetta, A. della Corte, A. Formisano, A. Grunhagen, P. Hertout, W. Herz, M. Huguet, F. Hurd, Y. Ilyin, P. Komarek, P. Libeyre, V. Marchese, C. Marinucci, A. Martinez, R. Martone, N. Martovetsky, P. Michael, N. Mitchell, A. Nijhuis, G. Nother, Y. Nunoya, M. Polak, A. Portone, L. S. Richard, M. Spadoni, M. Susser, S. Turtu, A. Vostner, Y. Takahashi, F. Wuchner, and L. Zani. The iter toroidal field model coil project. *Fusion Engineering and Design*, 73(2-4):189–327, 2005.

[19] J. L. Duchateau. New considerations about stability margins of nbti cable in conduit conductors. *IEEE Transactions on Applied Superconductivity*, 19(2):55–62, 2009.

[20] Shigehiro Nishijima, Steven Eckroad, Adela Marian, Kyeongdal Choi, Woo Seok Kim, Motoaki Terai, Zigang Deng, Jun Zheng, Jiasu Wang, Katsuya Umemoto, Jia Du, Pascal Febvre, Shane Keenan, Oleg Mukhanov, Lance D Cooley, Cathy P Foley, William V Hassenzahl, and Mitsuru Izumi. Superconductivity and the environment: a roadmap. *Superconductor Science and Technology*, 26(11):113001, sep 2013.

[21] Herman H. J. ten Kate. Superconducting magnet system for the atlas detector at cern. *IEEE TRANSACTIONS ON APPLIED SUPERCONDUCTIVITY*, 9:841–846, Jun 1999.

[22] D.E. Baynham. Evolution of detector magnets from cello to atlas and cms and toward future developments. *IEEE Transactions on Applied Superconductivity*, 16(2):493–498, 2006.

[23] D. Swoboda, D. Cacaut, and S. Evrard. Toward starting up of the alice dipole magnet. *IEEE Transactions on Applied Superconductivity*, 14(2):560–563, 2004.

[24] R Kleiner and P Müller. Intrinsic josephson effects in high-t c superconductors. *Physical Review B*, 49(2):1327, 1994.

[25] Andrea Napolitano, Samuele Ferracin, Michela Fracasso, Roberto Gerbaldo, Gianluca Ghigo, Laura Gozzelino, Daniele Torsello, and Francesco Laviano. Study of the thermal distribution for ybco based transition edge bolometers working above 77 k. In *2021 IEEE 14th Workshop on Low Temperature Electronics (WOLTE)*, pages 1–4, 2021.

[26] Nathan Newman and W Gregory Lyons. High-temperature superconducting microwave devices: fundamental issues in materials, physics, and engineering. *Journal of Superconductivity*, 6(3):119–160, 1993.

[27] John H Durrell, Mark D Ainslie, Difan Zhou, Philippe Vanderbemden, Tom Bradshaw, Susannah Speller, Mykhaylo Filipenko, and David A Cardwell. Bulk superconductors: a roadmap to applications. *Superconductor Science and Technology*, 31(10):103501, sep 2018.

[28] T Oka. Processing and applications of bulk htsc. *Physica C: Superconductivity and its applications*, 463:7–13, 2007.

[29] T Oka, S Hasebe, J Ogawa, S Fukui, T Nakano, N Sakai, M Miryala, M Murakami, and K Yokoyama. Novel magnetizing technique using high temperature superconducting bulk magnets for permanent magnets in interior permanent magnet rotors. *Superconductor Science and Technology*, 33(8):084003, 2020.

[30] H Seino, K Nagashima, and Y Arai. Development of superconducting magnetic bearing using superconducting coil and bulk superconductor. In *Journal of Physics: Conference Series*, volume 97, page 012101. IOP Publishing, 2008.

[31] Difan Zhou, Mitsuru Izumi, Motohiro Miki, Brice Felder, Tetsuya Ida, and Masahiro Kitano. An overview of rotating machine systems with high-temperature bulk superconductors. *Superconductor Science and Technology*, 25(10):103001, 2012.

[32] Bruno Douine, Kevin Berger, and Nickolay Ivanov. Characterization of high-temperature superconductor bulks for electrical machine application. *Materials*, 14(7):1636, 2021.

[33] S Denis, L Dusoulier, M Dirickx, Ph Vanderbemden, R Cloots, M Ausloos, and B Vanderheyden. Magnetic shielding properties of high-temperature superconducting tubes subjected to axial fields. *Superconductor Science and Technology*, 20(3):192–201, jan 2007.

[34] L. Schultz, O. de Haas, P. Verges, C. Beyer, S. Rohlig, H. Olsen, L. Kuhn, D. Berger, U. Noteboom, and U. Funk. Superconductively levitated transport system - the supratrans project. *IEEE Transactions on Applied Superconductivity*, 15(2):2301–2305, 2005.

[35] G G Sotelo, D H N Dias, O J Machado, E D David, R de Andrade Jr, R M Stephan, and G C Costa. Experiments in a real scale maglev vehicle prototype. *Journal of Physics: Conference Series*, 234(3):032054, jun 2010.

[36] Jiasu Wang, Suyu Wang, Jun Zheng, Fei Yen, Guangtong Ma, Lu Liu, Jing Li, and Wei Liu. Recent developments of the high temperature superconducting maglev at asclab. *IEEE Transactions on Applied Superconductivity*, 21(3):1551–1555, 2011.

[37] John R Hull. Superconducting bearings. *Superconductor Science and Technology*, 13(2):R1, feb 2000.

[38] F N Werfel, U Floegel-Delor, R Rothfeld, T Riedel, B Goebel, D Wippich, and P Schirrmeister. Superconductor bearings, flywheels and transportation. *Superconductor Science and Technology*, 25(1):014007, dec 2011.

[39] T Oka, H Kanayama, K Tanaka, S Fukui, J Ogawa, T Sato, M Yamaguchi, M Ooizumi, K Yokoyama, and K Noto. Study on magnetic separation system using high tc superconducting bulk magnets for water purification technique. *Journal of Physics: Conference Series*, 156(1):012031, mar 2009.

[40] T. Hiyama, H. Fujishiro, T. Tateiwa, T. Naito, H. Hayashi, and K. Tone. Trapped field enhancement of five-aligned superconducting bulk magnetized by pulse field for magnetic separation. *Physica C: Superconductivity*, 468(15):1469–1472, 2008. Proceedings of the 20th International Symposium on Superconductivity (ISS 2007).

[41] Yufeng Zhang, Difan Zhou, Tetsuya Ida, Motohiro Miki, and Mitsuru Izumi. Melt-growth bulk superconductors and application to an axial-gap-type rotating machine. *Superconductor Science and Technology*, 29(4):044005, mar 2016.

[42] A Nijhuis, Y Ilyin, and W Abbas. Axial and transverse stress–strain characterization of the eu dipole high current density nb3sn strand. *Superconductor Science and Technology*, 21(6):065001, mar 2008.

[43] Takashi Nakamura, Yoshitaka Itoh, Masaaki Yoshikawa, Tetsuo Oka, and Jun Uzawa. Development of a superconducting magnet for nuclear magnetic resonance using bulk high-temperature superconducting materials. *Concepts in Magnetic Resonance Part B: Magnetic Resonance Engineering*, 31B(2):65–70, 2007.

[44] Kyohei Ogawa, Takashi Nakamura, Yasuhiko Terada, Katsumi Kose, and Tomoyuki Haishi. Development of a magnetic resonance microscope using a high tc bulk superconducting magnet. *Applied Physics Letters*, 98(23):234101, 2011.

[45] R. Araneo and S. Celozzi. Analysis of the shielding performance of ferromagnetic screens. *IEEE Transactions on Magnetics*, 39(2):1046–1052, 2003.

[46] R. R. Ferber and F. J. Young. Enhancement of emp shielding by ferromagnetic saturation. *IEEE Transactions on Nuclear Science*, 17(6):354–359, 1970.

[47] V. Kelha, J. Pukki, R. Peltonen, A. Penttinen, R. Ilmoniemi, and J. Heino. Design, construction, and performance of a large-volume magnetic shield. *IEEE Transactions on Magnetics*, 18(1):260–270, 1982.

[48] James R Claycomb. Magnetic shields. *digital Encyclopedia of Applied Physics*, pages 1–32, 2003.

[49] Magnetic Shield Corporation. https://www.magnetic-shield.com/.

[50] Magnetic Shield Corporation. https://hollandshielding.com/mu-metal-magnetic-shielding-materials.

[51] Ł Tomków, Marian Ciszek, and Maciej Chorowski. Combined magnetic screen made of bi-2223 bulk cylinder and ybco tape rings—modeling and experiments. *Journal of Applied Physics*, 117(4):043901, 2015.

[52] James R. Claycomb. Magnetic shields. In *Applied superconductivity: handbook on devices and applications*, pages 780–806. John Wiley & Sons, 2015.

[53] P Arpaia, A Ballarino, G Giunchi, and G Montenero. MgB_2 cylindrical superconducting shielding for cryogenic measurement applications: a case study on dc current transformers. *Journal of Instrumentation*, 9(04):P04020, 2014.

[54] A. Bergen, H. J. van Weers, C. Bruineman, M. M. J. Dhallé, H. J. G. Krooshoop, H. J. M. ter Brake, K. Ravensberg, B. D. Jackson, and C. K. Wafelbakker. Design and validation of a large-format transition edge sensor array magnetic shielding system for space application. *Review of Scientific Instruments*, 87(10):105109, 2016.

[55] Yutaka Terao, Masaki Sekino, Hiroyuki Ohsaki, Hidekazu Teshima, and Mitsuru Morita. Magnetic shielding characteristics of multiple bulk superconductors for higher field applications. *IEEE transactions on applied superconductivity*, 21(3):1584–1587, 2010.

[56] L Wéra, J-F Fagnard, G A Levin, B Vanderheyden, and P Vanderbemden. A comparative study of triaxial and uniaxial magnetic shields made out of YBCO coated conductors. 28(7):074001, 2015.

[57] Y Nagasaki, M Solovyov, and F Gömöry. Experimental and numerical investigation of shielding performance of superconducting magnetic shields using coated conductor tapes. *IEEE Transactions on Applied Superconductivity*, 28(4):1–5, 2018.

[58] Pengtao Yang, Jean-Francois Fagnard, Philippe Vanderbemden, and Wanmin Yang. Magnetic shielding of a short thick gdbco tube fabricated by the buffer aided top-seeded infiltration and growth method. *Superconductor Science and Technology*, 32(11):115015, oct 2019.

[59] Laurent Wera, Jean-Francois Fagnard, Devendra K Namburi, Yunhua Shi, Benoit Vanderheyden, and Philippe Vanderbemden. Magnetic shielding above 1 t at 20 k with bulk, large grain ybco tubes made by buffer-aided top seeded melt growth. *IEEE Transactions on Applied Superconductivity*, 27(4):6800305, 2017.

[60] Daniel Barna, Giovanni Giunchi, Martin Novák, Kristof Brunner, Aniko Német, Carlo Petrone, Miroslav Atanasov, Hugues Bajas, and Jerome Feuvrier. An MgB_2 Superconducting Shield Prototype for the Future Circular Collider Septum Magnet. *IEEE Trans. Appl. Supercond.*, 29(8):4101310, 2019.

[61] Jean-François Fagnard, Steffen Elschner, Joachim Bock, Michel Dirickx, Benoît Vanderheyden, and Philippe Vanderbemden. Shielding efficiency and e (j) characteristics measured on large melt cast bi-2212 hollow cylinders in axial magnetic fields. *Superconductor Science and Technology*, 23(9):095012, 2010.

[62] JJ Rabbers, MP Oomen, E Bassani, G Ripamonti, and G Giunchi. Magnetic shielding capability of MgB_2 cylinders. *Superconductor Science and Technology*, 23(12):125003, 2010.

[63] Laurent Wera, Jean-Francois Fagnard, Devendra K Namburi, Yunhua Shi, Benoit Vanderheyden, and Philippe Vanderbemden. Magnetic shielding above 1 t at 20 k with bulk, large grain ybco tubes made by buffer-aided top seeded melt growth. *IEEE Transactions on Applied Superconductivity*, 27(4):1–5, 2016.

[64] Laura Gozzelino, Roberto Gerbaldo, Gianluca Ghigo, Daniele Torsello, Valentina Bonino, Marco Truccato, Mihai A Grigoroscuta, Mihail Burdusel, Gheorghe V Aldica, Viorel Sandu, Iuliana Pasuk, and Petre Badica. High

magnetic shielding properties of an MgB_2 cup obtained by machining a spark-plasma-sintered bulk cylinder. *Superconductor Science and Technology*, 33(4):044018, mar 2020.

[65] Frederic Sirois, Francesco Grilli, and Antonio Morandi. Comparison of constitutive laws for modeling high-temperature superconductors. *IEEE Transactions on Applied Superconductivity*, 29(1):8000110, 2019.

[66] Grigorii P Mikitik, Yasunori Mawatari, Andy TS Wan, and Frederic Sirois. Analytical methods and formulas for modeling high temperature superconductors. *IEEE Transactions on Applied Superconductivity*, 23(2):8001920–8001920, 2013.

[67] AM Campbell. An introduction to numerical methods in superconductors. *Journal of superconductivity and novel magnetism*, 24(1-2):27–33, 2011.

[68] D Ruiz-Alonso, T Coombs, and AM Campbell. Computer modelling of high-temperature superconductors using an a–v formulation. *Superconductor Science and Technology*, 17(5):S305, 2004.

[69] Naoyuki Amemiya, Shun-ichi Murasawa, Nobuya Banno, and Kengo Miyamoto. Numerical modelings of superconducting wires for ac loss calculations. *Physica C: Superconductivity*, 310(1-4):16–29, 1998.

[70] Z Hong, AM Campbell, and TA Coombs. Numerical solution of critical state in superconductivity by finite element software. *Superconductor Science and Technology*, 19(12):1246, 2006.

[71] Gregory P Lousberg, Marcel Ausloos, Christophe Geuzaine, Patrick Dular, Philippe Vanderbemden, and Benoit Vanderheyden. Numerical simulation of the magnetization of high-temperature superconductors: a 3d finite element method using a single time-step iteration. *Superconductor Science and Technology*, 22(5):055005, mar 2009.

[72] Alexandre Arsenault, Frédéric Sirois, and Francesco Grilli. Implementation of the h-ϕ formulation in comsol multiphysics for simulating the magnetization of bulk superconductors and comparison with the h-formulation. 31(2):6800111, 06 2021.

[73] Lorenzo Bortot, Bernhard Auchmann, Idoia Cortes Garcia, Herbert De Gersem, Michal Maciejewski, Matthias Mentink, Sebastian Schöps, Jeroen Van Nugteren, and Arjan P Verweij. A coupled a–h formulation for magneto-thermal transients in high-temperature superconducting magnets. *IEEE Transactions on Applied Superconductivity*, 30(5):4900911, 2020.

[74] Edgar Berrospe-Juarez, Víctor MR Zermeño, Frederic Trillaud, and Francesco Grilli. Real-time simulation of large-scale hts systems: Multi-scale and homogeneous models using the t–a formulation. *Superconductor Science and Technology*, 32(6):065003, 2019.

[75] A Stenvall and T Tarhasaari. Programming finite element method based hysteresis loss computation software using non-linear superconductor resistivity and T- formulation. *Superconductor Science and Technology*, 23(7):075010, jun 2010.

[76] Siddharth Pratap and Clay S Hearn. 3-d transient modeling of bulk high-temperature superconducting material in passive magnetic bearing applications. *IEEE Transactions on Applied Superconductivity*, 25(5):5203910, 2015.

[77] 73 - on the theory of superconductivity. In D. TER HAAR, editor, *Collected Papers of L.D. Landau*, pages 546–568. Pergamon, 1965.

[78] D. Dew-Hughes. Flux pinning mechanisms in type ii superconductors. *Philosophical Magazine*, 30(2):293–305, 1974.

[79] Willa Roland Miura Masashi Sato Michio Leroux Maxime Henry Michael David Civale Leonardo Eley, Serena. Accelerated vortex dynamics across the magnetic 3d-to-2d crossover in disordered superconductors. *npj Quantum Materials*, 3(1):37, 2018.

[80] Y Bugoslavsky, LF Cohen, GK Perkins, M Polichetti, TJ Tate, R Gwilliam, and AD Caplin. Enhancement of the high-magnetic-field critical current density of superconducting MgB_2 by proton irradiation. *Nature*, 411(6837):561–563, 2001.

[81] Jijie Huang and Haiyan Wang. Effective magnetic pinning schemes for enhanced superconducting property in high temperature superconductor yba2cu3o7- x: a review. *Superconductor Science and Technology*, 30(11):114004, 2017.

[82] Roland Willa, Alexei E Koshelev, Ivan A Sadovskyy, and Andreas Glatz. Strong-pinning regimes by spherical inclusions in anisotropic type-ii superconductors. *Superconductor Science and Technology*, 31(1):014001, 2017.

[83] T Izumi and K Nakaoka. Control of artificial pinning centers in rebco coated conductors derived from the trifluoroacetate metal-organic deposition process. *Superconductor Science and Technology*, 31(3):034008, 2018.

[84] Jian Zhang, Haiyan Wu, Guangzhen Zhao, Lu Han, and Jun Zhang. Progress in the study of vortex pinning centers in high-temperature superconducting films. *Nanomaterials*, 12(22), 2022.

[85] Y. B. Kim, C. F. Hempstead, and A. R. Strnad. Critical persistent currents in hard superconductors. *Phys. Rev. Lett.*, 9:306–309, Oct 1962.

[86] CHARLES P. BEAN. Magnetization of high-field superconductors. *Rev. Mod. Phys.*, 36:31–39, Jan 1964.

[87] Yosef Yeshurun, Alexis P. Malozemoff, and Avner a. Shaulov. Magnetic relaxation in high-temperature superconductors. *Reviews of Modern Physics*, 68:911–949, 1996.

[88] E H Brandt. The flux-line lattice in superconductors. *Reports on Progress in Physics*, 58(11):1465, nov 1995.

[89] Y.S. Cha. An empirical correlation for e(j,t) of a melt-cast-processed bscco-2212 superconductor under self field. *IEEE Transactions on Applied Superconductivity*, 13(2):2028–2031, 2003.

[90] A Nader. Magnetic relaxation of a superconducting slab: a description of the temporal evolution. *Superconductor Science and Technology*, 15(6):894, apr 2002.

[91] P. W. Anderson. Theory of flux creep in hard superconductors. *Phys. Rev. Lett.*, 9:309–311, Oct 1962.

[92] E. Zeldov, N. M. Amer, G. Koren, A. Gupta, R. J. Gambino, and M. W. McElfresh. Optical and electrical enhancement of flux creep in $yba_2cu_3o_{7-\delta}$ epitaxial films. *Phys. Rev. Lett.*, 62:3093–3096, Jun 1989.

[93] Francesco Grilli. Numerical modeling of hts applications. *IEEE Transactions on Applied Superconductivity*, 26(3):1–8, 2016.

[94] A M Campbell. A new method of determining the critical state in superconductors. *Superconductor Science and Technology*, 20(3):292–295, feb 2007.

[95] A M Campbell. The interaction distance between flux lines and pinning centres. *Journal of Physics C: Solid State Physics*, 4(18):3186, dec 1971.

[96] W.S. Seow, R.A. Doyle, J.D. Johnson, D. Kumar, R. Somekh, D.J.C. Walker, and A.M. Campbell. The elastic regime of vortices in superconducting ybco and multilayer ybco/prbco films. *Physica C: Superconductivity*, 241(1):71–82, 1995.

[97] F Gömöry, M Vojenčiak, E Pardo, and J Šouc. Magnetic flux penetration and ac loss in a composite superconducting wire with ferromagnetic parts. *Superconductor Science and Technology*, 22(3):034017, 2009.

[98] F Gömöry and J Sheng. Two methods of ac loss calculation in numerical modelling of superconducting coils. *Superconductor Science and Technology*, 30(6):064005, may 2017.

[99] F Gömöry, M Vojenčiak, E Pardo, M Solovyov, and J Šouc. Ac losses in coated conductors. *Superconductor Science and Technology*, 23(3):034012, 2010.

[100] Roberto Brambilla, Francesco Grilli, and Luciano Martini. Development of an edge-element model for AC loss computation of high-temperature superconductors. *Superconductor Science and Technology*, 20(1):16–24, nov 2006.

[101] Valtteri Lahtinen, Antti Stenvall, Frédéric Sirois, and Matti Pellikka. A finite element simulation tool for predicting hysteresis losses in superconductors using an h-oriented formulation with cohomology basis functions. *Journal of Superconductivity and Novel Magnetism*, 28:2345–2354, 08 2015.

[102] Frédéric Sirois and Francesco Grilli. Potential and limits of numerical modelling for supporting the development of HTS devices. *Superconductor Science and Technology*, 28(4):043002, mar 2015.

[103] WJ Carr Jr. *AC loss and macroscopic theory of superconductors*. CRC press, 2001.

[104] Ernst Helmut Brandt and Mikhail Indenbom. Type-ii-superconductor strip with current in a perpendicular magnetic field. *Physical review B*, 48(17):12893, 1993.

[105] K Yamafuji and Takanobu Kiss. Current-voltage characteristics near the glass-liquid transition in high-tc superconductors. *Physica C: Superconductivity*, 290(1-2):9–22, 1997.

[106] Nicolò Riva, Frederic Sirois, Christian Lacroix, Felix Pellerin, Jael Giguere, Francesco Grilli, and B. Dutoit. The eta-beta model model: an alternative to the power-law model for numerical simulations of rebco tapes, 2021.

[107] M. J. Qin, X. L. Wang, H. K. Liu, and S. X. Dou. Evidence for vortex pinning induced by fluctuations in the transition temperature of mgb_2 superconductors. *Phys. Rev. B*, 65:132508, Mar 2002.

[108] G. Blatter, M. V. Feigel'man, V. B. Geshkenbein, A. I. Larkin, and V. M. Vinokur. Vortices in high-temperature superconductors. *Rev. Mod. Phys.*, 66:1125–1388, Oct 1994.

[109] Roger Wördenweber. Mechanism of vortex motion in high-temperature superconductors. *Reports on Progress in Physics*, 62(2):187, feb 1999.

[110] F. X. Xiang, X. L. Wang, X. Xun, K. S. B. De Silva, Y. X. Wang, and S. X. Dou. Evidence for transformation from tc to l pinning in MgB_2 by graphene oxide doping with improved low and high field jc and pinning potential. *Applied Physics Letters*, 102(15):152601, 2013.

[111] C. P. Bean. Magnetization of hard superconductors. *Phys. Rev. Lett.*, 8:250–253, Mar 1962.

[112] D. LeBlanc and M. A. R. LeBlanc. ac-loss valley in type-ii superconductors. *Phys. Rev. B*, 45:5443–5449, Mar 1992.

[113] W. A. Fietz, M. R. Beasley, J. Silcox, and W. W. Webb. Magnetization of superconducting nb-25*Phys. Rev.*, 136:A335–A345, Oct 1964.

[114] JHP Watson. Magnetization of synthetic filamentary superconductors. b. the dependence of the critical current density on temperature and magnetic field. *Journal of Applied Physics*, 39(7):3406–3413, 1968.

[115] S. L. Wipf. Magnetic instabilities in type-ii superconductors. *Phys. Rev.*, 161:404–416, Sep 1967.

[116] P. S. Swartz and C. P. Bean. A model for magnetic instabilities in hard superconductors: The adiabatic critical state. *Journal of Applied Physics*, 39(11):4991–4998, 1968.

[117] D A Moseley, D P Wilkinson, T Mousavi, A R Dennis, S Speller, and J H Durrell. A new MgBsub2/sub bulk ring fabrication technique for use in magnetic shielding or bench-top NMR systems. *Superconductor Science and Technology*, 35(8):085003, jun 2022.

[118] Kunitoshi Murai, Jun'ya Hori, Yoshiko Fujii, Jonah Shaver, and Gregory Kozlowski. Magnetic flux pinning and flux jumps in polycrystalline MgB_2. *Cryogenics*, 45(6):415–420, 2005.

[119] D A Moseley, G A B Matthews, D Zhou, V Cientanni, Y Tsui, M D Ainslie, S Speller, and J H Durrell. Improved pulsed field magnetisation in MgBsub2/sub trapped-field magnets. *Superconductor Science and Technology*, 34(8):085018, jul 2021.

[120] RG Mints. Flux creep and flux jumping. *Physical Review B*, 53(18):12311, 1996.

[121] K.-H. Müller and C. Andrikidis. Flux jumps in melt-textured y-ba-cu-o. *Phys. Rev. B*, 49:1294–1307, Jan 1994.

[122] R. G. Mints and A. L. Rakhmanov. Critical state stability in type-ii superconductors and superconducting-normal-metal composites. *Rev. Mod. Phys.*, 53:551–592, Jul 1981.

[123] M Polichetti, D Zola, I Husek, P Kovác, and S Pace. Effects of impurities addition in MgB_2/nb tapes on flux jumps instability and critical current density. In *Journal of Physics: Conference Series*, volume 150, page 052212. IOP Publishing, 2009.

[124] Maxim Marchevsky. Quench detection and protection for high-temperature superconductor accelerator magnets. *Instruments*, 5(3), 2021.

[125] Muralidhar Miryala, Sai Srikanth Arvapalli, Naomichi Sakai, Masato Murakami, Hidehiko Mochizuki, Tomoyuki Naito, Hiroyuki Fujshiro, Milos Jirsa, Akira Murakami, and Jacques Noudem. Complex pulse magnetization process and mechanical properties of spark plasma sintered bulk MgB_2. *Materials Science and Engineering: B*, 273:115390, 2021.

[126] Sai Srikanth Arvapalli, Muralidhar Miryala, Naomichi Sakai, Masato Murakami, and Milos Jirsa. Novel ultra-sonic boron refinement in distilled water for cost-efficient fabrication of MgB_2 bulk ceramic superconductors. *Ceramics International*, 48(19, Part A):28102–28111, 2022.

[127] Michela Fracasso, Fedor Gömöry, Mykola Solovyov, Roberto Gerbaldo, Gianluca Ghigo, Francesco Laviano, Andrea Napolitano, Daniele Torsello, and Laura Gozzelino. Modelling and performance analysis of MgB_2 and hybrid magnetic shields. *Materials*, 15(2), 2022.

[128] H Fujishiro, H Mochizuki, T Naito, M D Ainslie, and G Giunchi. Flux jumps in high-j_c MgB_2 bulks during pulsed field magnetization. *Superconductor Science and Technology*, 29(3):034006, feb 2016.

[129] You-He Zhou and Xiaobin Yang. Numerical simulations of thermomagnetic instability in high-T_c superconductors: Dependence on sweep rate and ambient temperature. *Phys. Rev. B*, 74:054507, Aug 2006.

[130] Jing Xia, Maosheng Li, and Youhe Zhou. Numerical investigations on the characteristics of thermomagnetic instability in MgB_2 bulks. *Superconductor Science and Technology*, 30(7):075004, jun 2017.

[131] Weiwei Zhang, Jing Xia, Huadong Yong, and Youhe Zhou. Mechanical response induced by flux jump in a cylindrical superconductor. *AIP Advances*, 10(2):025021, 2020.

[132] Ze Jing. Coupled multiphysics modeling of the thermal-magnetic-mechanical instability behavior in bulk superconductors during pulsed field magnetization. *Superconductor Science and Technology*, 35(5):054006, apr 2022.

[133] NorimasA; Muranaka Takahiro; Zenitani Yuji; Akimitsu Jun Nagamatsu, Jun; Nakagawa. Superconductivity at 39 k in magnesium diboride. *Nature*, 410(6824):63–64, 2001.

[134] Kévin Berger, Michael Rudolf Koblischka, Bruno Douine, Jacques Noudem, Pierre Bernstein, Thomas Hauet, and Jean Lévêque. High magnetic field generated by bulk MgB_2 prepared by spark plasma sintering. *IEEE Transactions on Applied Superconductivity*, 26(3):6801005, 2016.

[135] Jacques G. Noudem, Yiteng Xing, Pierre Bernstein, Richard Retoux, Masaki Higuchi, Srikanth S. Arvapalli, Miryala Muralidhar, and Masato Murakami. Improvement of critical current density of MgB_2 bulk superconductor processed by spark plasma sintering. *Journal of the American Ceramic Society*, 103(11):6169–6175, 2020.

[136] Matt Rindfleisch and Michael Tomsic. Superconducting MgB_2 tubes for passive magnetic field shielding for the electron ion collider. *Technical report:*, 11 2019.

[137] Laura Gozzelino, Roberto Gerbaldo, Gianluca Ghigo, Francesco Laviano, Daniele Torsello, Valentina Bonino, Marco Truccato, Dan Batalu, Mihai A Grigoroscuta, Mihail Burdusel, Gheorghe V Aldica, and Petre Badica. Passive magnetic shielding by machinable MgB_2 bulks: measurements and numerical simulations. *Superconductor Science and Technology*, 32(3):034004, 2019.

[138] Giovanni Giunchi, Giovanni Ripamonti, Tommaso Cavallin, and Enrico Bassani. The reactive liquid mg infiltration process to produce large superconducting bulk MgB_2 manufacts. *Cryogenics*, 46(2):237–242, 2006.

[139] AG Bhagurkar, A Yamamoto, L Anguilano, AR Dennis, JH Durrell, N Hari Babu, and DA Cardwell. A trapped magnetic field of 3 t in homogeneous, bulk MgB_2 superconductors fabricated by a modified precursor infiltration and growth process. *Superconductor Science and Technology*, 29(3):035008, 2016.

[140] Marina Putti, R Vaglio, and JM Rowell. Radiation effects on MgB_2: a review and a comparison with a15 superconductors. *Superconductor Science and Technology*, 21(4):043001, 2008.

[141] S Okayasu, M Sasase, K Hojou, Y Chimi, A Iwase, H Ikeda, R Yoshizaki, T Kambara, H Sato, Y Hamatani, et al. Irradiation effects on MgB_2 bulk samples and formation of columnar defects in high-tc superconductor. *Physica C: Superconductivity*, 382(1):104–107, 2002.

[142] M Angst, R Puzniak, A Wisniewski, J Jun, SM Kazakov, J Karpinski, J Roos, and H Keller. Temperature and field dependence of the anisotropy of mgb 2. *Physical review letters*, 88(16):167004, 2002.

[143] VG Kogan and SL Bud'ko. Anisotropy parameters of superconducting MgB_2. *Physica C: Superconductivity*, 385(1-2):131–142, 2003.

[144] J-H Ahn and S Oh. Pore structures and grain connectivity of bulk MgB_2. *Physica C: Superconductivity*, 469(15-20):1235–1238, 2009.

[145] Qingshuang Ma, Junming Peng, Zongqing Ma, Fang Cheng, Feng Lan, Chong Li, Zhenwen Yang, Chenxi Liu, and Yongchang Liu. Improved grain connectivity and critical current density in ex-situ MgB_2 superconductors prepared by two-step sintering. *Materials Chemistry and Physics*, 204:62–66, 2018.

[146] TA Prikhna, Michael Eisterer, Harald W Weber, W Gawalek, VV Kovylaev, MV Karpets, TV Basyuk, and VE Moshchil. Nanostructural inhomogeneities acting as pinning centers in bulk MgB_2 with low and enhanced grain connectivity. *Superconductor Science and Technology*, 27(4):044013, 2014.

[147] G. Aldica, M. Burdusel, S. Popa, I. Pasuk, A.M. Ionescu, A. Kuncser, and P. Badica. Ex situ spark plasma sintering of short powder-in-tube MgB_2 tapes with open and closed ends. *Journal of Superconductivity and Novel Magnetism*, 31(11):3423–3432, 2018.

[148] Randall M. German. Chapter ten - sintering with external pressure. pages 305 – 354, 2014.

[149] Z. A. Munir, U. Anselmi-Tamburini, and M. Ohyanagi. The effect of electric field and pressure on the synthesis and consolidation of materials: A review of the spark plasma sintering method. *Journal of Materials Science*, 41(3):763–777, Feb 2006.

[150] W. Häßler, J. Scheiter, P. Hädrich, S. Kauffmann-Weiß, B. Holzapfel, M. Oomen, and K. Nielsch. Properties of ex-situ MgB_2 bulk samples prepared by uniaxial hot pressing and spark plasma sintering. *Physica C: Superconductivity and its Applications*, 551:48 – 54, 2018.

[151] T C Shields, K Kawano, D Holdom, and J S Abell. Microstructure and superconducting properties of hot isostatically pressed MgBsub2/sub. *Superconductor Science and Technology*, 15(2):202–205, jan 2002.

[152] C. Romero-Salazar, F. Morales, R. Escudero, A. Durán, and O. A. Hernández-Flores. Flux jumps in hot-isostatic-pressed bulk Mgb_2 superconductors: Experiment and theory. *Phys. Rev. B*, 76:104521, Sep 2007.

[153] C E J Dancer, D Prabhakaran, M Başoğlu, E Yanmaz, H Yan, M Reece, R I Todd, and C R M Grovenor. Fabrication and properties of denseiex situ/imagnesium diboride bulk material synthesized using spark plasma sintering. *Superconductor Science and Technology*, 22(9):095003, aug 2009.

[154] Giovanni Giunchi, Daniele Turrioni, Vladimir Kashikhin, Hogan Nguyen, and Emanuela Barzi. Feasibility study of a MgB_2 superconducting magnetic cloak. *IEEE Transactions on Applied Superconductivity*, 26(3):1–5, 2016.

[155] Victor Chabanenko, Roman Puźniak, Adam Nabiałek, Sergei Vasiliev, Vladimir Rusakov, Loh Huanqian, Ritta Szymczak, Henryk Szymczak, Jan Jun, Janusz Karpiński, et al. Flux jumps and ht diagram of instability for MgB_2. *Journal of low temperature physics*, 130(3):175–191, 2003.

[156] AV Bobyl, DV Shantsev, TH Johansen, WN Kang, HJ Kim, EM Choi, and SI Lee. Current-induced dendritic magnetic instability in superconducting mgb 2 films. *Applied physics letters*, 80(24):4588–4590, 2002.

[157] G. Ghigo, F. Laviano, L. Gozzelino, R. Gerbaldo, E. Mezzetti, E. Monticone, and C. Portesi. Evidence of rf-driven dendritic vortex avalanches in MgB_2 microwave resonators. *Journal of Applied Physics*, 102(11):113901, 2007.

[158] D Zola, M Polichetti, MG Adesso, P Kovác, L Martini, and S Pace. Thermomagnetic instability and critical current density in MgB_2 monofilamentary tapes. *Physica C: Superconductivity and its applications*, 468(7-10):761–764, 2008.

[159] L Miu, G Aldica, P Badica, I Ivan, D Miu, and G Jakob. Improvement of the critical current density of spark plasma sintered MgB_2 by c60 addition. *Superconductor Science and Technology*, 23(9):095002, 2010.

[160] Hiroyuki Fujishiro, Tomoyuki Naito, and Takafumi Yoshida. Numerical simulation of the trapped field in MgB_2 bulk disks magnetized by field cooling. *Superconductor Science and Technology*, 27(6):065019, 2014.

[161] Francesco Laviano. *Vortex Avalanches in Superconductors Visualized by Magneto-Optical Imaging*, pages 133–157. Springer International Publishing, Cham, 2017.

[162] Thomas Qureishy, Carlos Laliena, Elena Martínez, Atle Jorstad Qviller, Jørn Inge Vestgården, Tom Henning Johansen, Rafael Navarro, and Pavlo Mikheenko. Dendritic flux avalanches in a superconducting MgB_2 tape. *Superconductor Science and Technology*, 30(12):125005, 2017.

[163] G. Aldica, M. Burdusel, S. Popa, M. Enculescu, I. Pasuk, and P. Badica. The influence of heating rate on superconducting characteristics of MgB_2 obtained by spark plasma sintering technique. *Physica C: Superconductivity and its Applications*, 519:184–189, 2015.

[164] G. Aldica, D. Batalu, S. Popa, I. Ivan, P. Nita, Y. Sakka, O. Vasylkiv, L. Miu, I. Pasuk, and P. Badica. Spark plasma sintering of MgB_2 in the two-temperature route. *Physica C: Superconductivity*, 477:43–50, 2012.

[165] G.V. Aldica, M. Burdusel, E.M. Cioca, and P. Badica. Machinable superconducting material and magnetic field concentrator/storer made of a superconducting material based on MgB_2, machinable by chip remova. *Patent No. RO130252-B1*, 28 February 2020,.

[166] K Yokoyama, T Oka, K Berger, R Dorget, M Koblischka, M Grigoroscuta, M Burdusel, D Batalu, G Aldica, P Badica, N Sakai, M Muralidhar, and M Murakami. Investigation of flux jumps during pulsed field magnetization in graphene-added MgB_2 bulks. *Journal of Physics: Conference Series*, 1559(1):012080, jun 2020.

[167] E. Bartolomé, X. Granados, A. Palau, T. Puig, X. Obradors, C. Navau, E. Pardo, A. Sánchez, and H. Claus. Magnetization and critical current of finite superconducting $\mathrm{Yba_2cu_3o_7}$ rings. *Phys. Rev. B*, 72:024523, Jul 2005.

[168] L Gozzelino, R Gerbaldo, G Ghigo, F Laviano, M Truccato, and A Agostino. Superconducting and hybrid systems for magnetic field shielding. *Superconductor Science and Technology*, 29(3):034004, jan 2016.

[169] L Gozzelino, R Gerbaldo, G Ghigo, F Laviano, and M Truccato. Comparison of the shielding properties of superconducting and superconducting/ferromagnetic bi- and multi-layer systems. *Journal of Superconductivity and Novel Magnetism*, 30:749–756, mar 2017.

[170] L Gozzelino, A Agostino, R Gerbaldo, G Ghigo, and F Laviano. Magnetic shielding efficiency of superconducting/ferromagnetic systems. *Superconductor Science and Technology*, 25(11):115013, sep 2012.

[171] Laura Gozzelino, Roberto Gerbaldo, Gianluca Ghigo, Francesco Laviano, Angelo Agostino, Elisabetta Bonometti, Mario Chiampi, Alessandra Manzin, and Luca Zilberti. Dc shielding properties of coaxial MgB_2/fe cups. *IEEE transactions on applied superconductivity*, 23(3):8201305, 2013.

[172] M Filtz and H Büssing. Screening attenuation of conducting and ferromagnetic hollow cylinders of finite length. *Electrical Engineering*, 90:469–478, 2008.

[173] Laura Gozzelino, Michela Fracasso, Mykola Solovyov, Fedor Gömöry, Andrea Napolitano, Roberto Gerbaldo, Gianluca Ghigo, Francesco Laviano, Daniele Torsello, Mihai A Grigoroscuta, Gheorghe Aldica, Mihail Burdusel, and Petre Badica. Screening of magnetic fields by superconducting and hybrid shields with a circular cross-section. *Superconductor Science and Technology*, 35(4):044002, feb 2022.

[174] Comsol. How to estimate the number of degrees of freedom in a model.

[175] J Zou, M D Ainslie, H Fujishiro, A G Bhagurkar, T Naito, N Hari Babu, J-F Fagnard, P Vanderbemden, and A Yamamoto. Numerical modelling and comparison of MgBsub2/subbulks fabricated by HIP and infiltration growth. *Superconductor Science and Technology*, 28(7):075009, may 2015.

[176] V Cientanni, M D Ainslie, H Fujishiro, and K Takahashi. Modelling higher trapped fields by pulsed field magnetisation of composite bulk MgBsub2/sub superconducting rings. *Superconductor Science and Technology*, 34(11):114003, oct 2021.

[177] NV Anshukova, BM Bulychev, AI Golovashkin, LI Ivanova, AA Minakov, and AP Rusakov. Low-temperature anomalies in the specific heat and thermal conductivity of MgB_2. *Physics of the Solid State*, 45(7):1207–1212, 2003.

[178] Ch Wälti, E Felder, C Degen, G Wigger, R Monnier, B Delley, and HR Ott. Strong electron-phonon coupling in superconducting mgb 2: A specific heat study. *Physical Review B*, 64(17):172515, 2001.

[179] Yuxing Wang, Tomasz Plackowski, and Alain Junod. Specific heat in the superconducting and normal state (2–300 k, 0–16 t), and magnetic susceptibility of the 38 k superconductor MgB_2: evidence for a multicomponent gap. *Physica C: Superconductivity*, 355(3-4):179–193, 2001.

[180] Carmine Senatore, Paola Lezza, Rolf Lortz, O Shcherbakova, Wai Kong Yeoh, SX Dou, and R Flukiger. Specific heat and magnetic relaxation analysis of MgB_2 bulk samples with and without additives. *IEEE transactions on applied superconductivity*, 17(2):2941–2944, 2007.

[181] VPS Awana, Arpita Vajpayee, Monika Mudgel, V Ganesan, AM Awasthi, GL Bhalla, and H Kishan. Physical property characterization of bulk MgB_2 superconductor. *The European Physical Journal B*, 62(3):281–294, 2008.

[182] E Bauer, Ch Paul, St Berger, S Majumdar, H Michor, M Giovannini, A Saccone, and A Bianconi. Thermal conductivity of superconducting MgB_2. *Journal of Physics: Condensed Matter*, 13(22):L487, 2001.

[183] Jan Mucha, Marek Pękała, Jadwiga Szydłowska, Wojciech Gadomski, Jun Akimitsu, Jean-François Fagnard, Philippe Vanderbemden, Rudi Cloots, and Marcel Ausloos. Magnetotransport study of MgB_2 superconductor. *Superconductor Science and Technology*, 16(10):1167, 2003.

[184] T Cavallin, EA Young, C Beduz, Y Yang, and G Giunchi. Thermal conductivity of bulk MgB_2 produced by infiltration of different boron powders. *IEEE transactions on applied superconductivity*, 17(2):2770–2773, 2007.

[185] Hiroshi Maeda, Yoshiaki Tanaka, Masao Fukutomi, and Toshihisa Asano. A new high-tc oxide superconductor without a rare earth element. *Japanese Journal of Applied Physics*, 27(2A):L209, feb 1988.

[186] Jean-François Fagnard, S Elschner, A Hobl, J Bock, Benoît Vanderheyden, and Philippe Vanderbemden. Magnetic shielding properties of a superconducting hollow cylinder containing slits: modelling and experiment. *Superconductor Science and Technology*, 25(10):104006, 2012.

[187] Jean-François Fagnard, Michel Dirickx, Marcel Ausloos, Grégory Lousberg, Benoît Vanderheyden, and Ph Vanderbemden. Magnetic shielding properties of high-tc superconducting hollow cylinders: model combining experimental data for axial and transverse magnetic field configurations. *Superconductor science and technology*, 22(10):105002, 2009.

[188] Jean-Francois Fagnard, Samuel Denis, Gregory Lousberg, Michel Dirickx, Marcel Ausloos, Benoit Vanderheyden, and Philippe Vanderbemden. Dc and ac shielding properties of bulk high-tc superconducting tubes. *IEEE Transactions on Applied Superconductivity*, 19(3):2905–2908, 2009.